University of Leoben
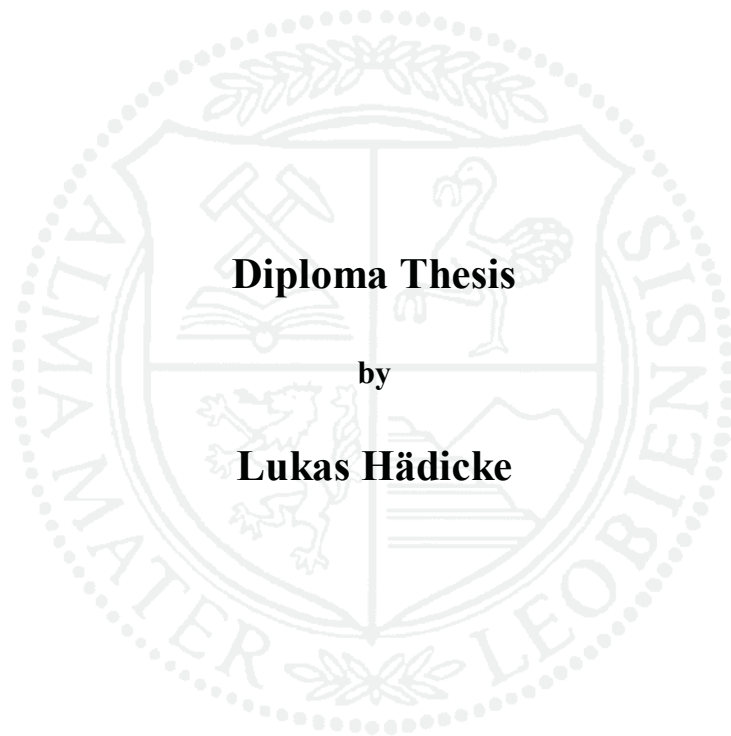
Structural development and thermal stability of Zr-Al-Y-N and Zr-Al-Y-O-N thin films

Diploma Thesis

by

Lukas Hädicke

Leoben, 2.März.2009

Affidavit

I declare in lieu of oath, that I wrote this thesis and performed the associated research by myself, using only literature cited in this volume.

Leoben, 2.März.2009

Acknowledgements

In the first place I want to thank **Paul Mayrhofer** for making this thesis possible. The organising of a scientific stay at the Thin Films Physics Division at the University of Linköping wouldn't have been possible without him.

I also want to express my gratitude to my supervisor **Martin Moser** who was very supportive and most motivating. Thanks for his guidance and his point of view.

Thanks to the head of Thin Films Physics Division **Lars Hultman**. He and his group provided an unmatched scientific hospitality and support.

Without **Martina Lattemann**, the master of electron transmission, a lot of atoms wouldn't have been become visible. So I thank her for her patience in teaching me.

Manfred Beckers was always the person who was there when I needed help or a clever advice when I didn't know that I needed one.

The man who shared the adventures in examining this thesis is **Richard Rachbauer**. I want to thank him, who-always-gave-a-clear-party-plan, in wishing him good luck for his PhD.

Thanks to my **brothers** and my **parents** for the generous support in every phase of my life.

My special gratitude goes to all my **friends** for playing their special roles in my life and made it like this.

L. Hädicke

Table of contents

L. Hädicke

1   Introduction

Thin-film technology is simultaneously one of the oldest arts and one of the newest sciences. The first film considered as a thin-film is the 0.3 μm thick gold film found in Luxor dating to the Eighteen Dynasty (1567 – 1320 B.C). In comparison, today gold leaf can be machine-beaten to 0.1 μm and to 0.05 μm when beaten by skilled craftsman [1].

Nowadays, thin-films are key-players in modern development of materials and engineering. Thin-microelectronics and optoelectronic industries strong technology drivers of our economy, a fact manifested by the explosive growth in communications, and information processing, storage and display applications. Developments in these technologies have expanding thin film uses towards different areas, e.g. coatings of all kinds (optical, decorative, environmental, and wear resistant), biotechnology, and energy and aerospace applications [83].

An application example of coatings is, the so called Thermal Barrier Coatings (TBC) which are used in aircraft turbo engine components. There, the blade made of Ni based super alloy which has been optimized for high temperature is protected with TBC's because of high temperature and high temperature corrosion The coating system consists of a Bond Coating (BC) which is directly deposited on the blade, a Thermal Grown Oxide layer (TGO) which is used as barrier for oxygen and the intrinsic TBC. The role of the bond coat, 100±50 μm thick, is to provide additional corrosion and oxidation protection to the bulk component. The bond coat alloy is designed similar to that of the super alloy but has usually a higher content of Al. The bond coat is essentially a reservoir of Al to support the formation of TGO at the TBC/BC interface. Because the top coat can not inhibit the oxygen transport through the layer, the TGO, primarily α-Al_2O_3 acts as a diffusion barrier for oxygen. The primary function of the ceramic TBC top coat is to act as a thermal insulator and to reduce the heat transfer to the metallic substrate (e.g. the blade material). These requirements are found in ZrO_2 partly or completely stabilized with additions of Y_2O_3. Yttria Stabilized Zirconia (YSZ) has been found empirically the most spallation resistant composition in thermal cycling conditions and therefore is commonly used as the thermal ceramic insulation layer in present TBC systems[46,51,85,86].

Generally, light weight alloys such as γ-TiAl play an increasingly important role in mdern development of materials for automotive, energy and aerospace applications. Their specific stiffness, strength and creep resistance (compared to the low mass) potentially leads to lower weight savings (up to 50%) and therefore lower mechanical loads on components like

L. Hädicke

turbines. However, for a wider use their resistance against oxidation, erosion and hot corrosion needs to be improved. These, basically surface – related material attacks require the development of adequate protective coatings, especially excellent transitions between the metallic –like substrate material and the ceramic TBC. Consequently, Zr-Al-Y-N and Zr-Al-Y-O-N coatings are developed and investigated with respect to their structure, morphology, mechanical properties and thermal stability as a function of their Y-content.

L. Hädicke

Physical vapour deposition techniques

1.1 General

Up to now, numerous specialized process variations and modifications of Physical Vapour Deposition (PVD) have been developed and are in industrial use. Their main advantages can be found in the variety of deposition materials. The deposited coatings, however, are usually far from their state of thermo dynamical equilibrium. [3,5,13,11,82,83]

The main principle of the PVD process is the transition of a liquid or solid phase to the vapour phase, transport of the vapour from the source to the substrate, and finally its condensation, followed by film nucleation and growth.

There are different possibilities to obtain the vapour phase of the material source: thermal evaporation by induction, resistance, electron beam, arc or laser heating; thermal sublimation (continuous or pulsed arc discharge) and sputtering (conventional or magnetron). Thus, a possible way to classify the different PVD processes, among others, is by its means of obtaining the vapour phase of the source (target) [4,5,6,14,15]. Another possibility is to subdivide PVD processes into plasma assisted and non-plasma assisted processes.

As mentioned above, in the vapour deposition processes, the coating material is heated in vacuum until it evaporates. Under the condition that the vacuum is high enough (10^{-3} to 10^{-6} Pa), there is a long free mean path for the particles, assuming that there is no particle interaction during the transport to the substrate and therefore, the particles are not deflected before they are deposited. The evaporation rate can reach high values and the coatings have an evenly distributed coating thickness with sufficient adhesion. Avoiding reactions between source material and evaporant caused by high reactivity at high temperatures, different variations of the evaporation deposition processes have been developed, e.g. arc vapour [4,15].

Sputtering is the process of obtaining a vapour by transferring the kinetic energy from an incident particle onto a material, which is therefore named the target. This results in the direct ejection of surface atoms from the solid to the vapour phase without entering the liquid state. [6,7]. To induce the ion bombardment, an inert working gas like argon and a high voltage source are necessary. By applying a voltage, a glow-discharge plasma is ignited between the cathodic target and the anodic substrate. The deposition rate is relatively low and

L. Hädicke

the coating thickness is not evenly distributed [15,16]. For this work a sputtering deposition facility was used so, this technique will be discussed in more detail in chapter 3.1.1.

The ion plating process is a hybrid process, i.e. either vaporization of the coating material takes place by thermal energy or momentum transfer in an anodic source or the coating material is directly supplied as vapour. Some of the vaporized atoms are ionized by a glow discharge produced by biasing the substrate to a high negative potential and employing a working gas. Therefore, the substrate and the coating underlie a constant bombardment of high-energy ions leading to better coating adhesion and modified microstructure within the coating. Deposition rates are high, but the coatings have an unevenly distributed coating thickness. The substrate temperature is below 300°C and, therefore, relatively low [16,83].

1.2   Plasma

A plasma consists of ions, free electrons and neutral atoms. The amount of positive and negative charge carriers is equal, thus, it can be defined as a quasi-neutral gas of charged and neutral particles which show collective behaviour, triggered by Coulomb interactions. The electric fields are generated by the movement of charged particles in the plasma, which induce local concentrations of positive and negative charge. The movement of charged particles also induces a current and therefore, magnetic fields. For this reason, the movement of charged particles, which are far away, is also influenced [15,17].

In opposite to the plasma formation of pure substances in thermal equilibrium, the low-pressure processing discharges, as used in PVD processes, are never in thermal equilibrium. The plasma density is reduced due to several loss mechanisms such as recombination, radiation and diffusion from the discharge zone with subsequent wall reaction. Therefore, external source of energy is required to provide a stable discharge process. The latter can be of thermal, electric or of natural origin [82].

1.2.1   Gas discharge/plasma

L. Hädicke

The process, where electrical charges are transported in a gas or vapour by mobile charge carriers (ions and electrons), is called gas discharge. This process consists of charge carrier generation, particle movement in electrical fields, and recombination reactions. The most important way to generate free charge carriers is the ionization of neutral particles by kinetic energy transfer through inelastic impact of electrons [9].

The general technical arrangement is a direct current (DC) applied between two electrodes, usually the target (cathode) and substrate (anode), within a low-pressure gas atmosphere. The gas ionizes and a glow discharge can be initiated. This only occurs, if the applied voltage exceeds the ionization potential of the gas concerned. The voltage is in the order of some hundreds of volts, and the current of typically several hundred milliamps [8,9,11].
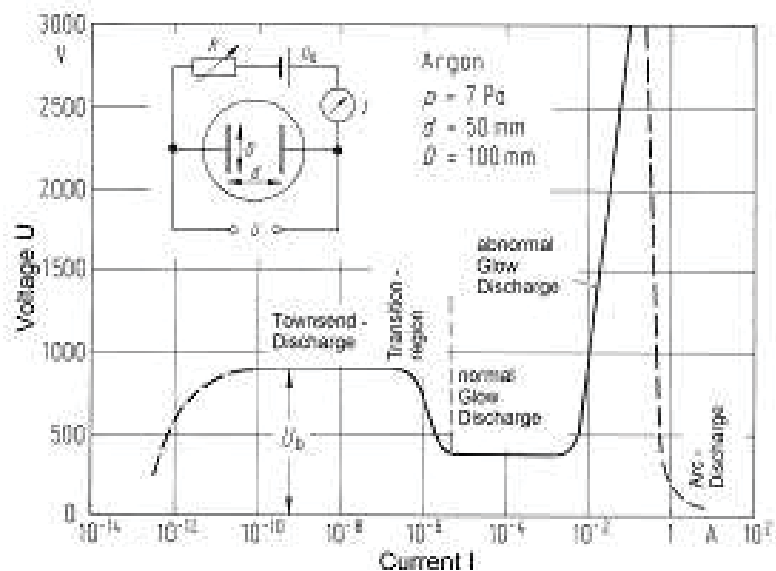

Figure2.1 Voltage-Current characteristics of a glow discharge process [3].

Increasing the voltage and so the electric field, the energy of the electrons increases too. If they gain enough energy, charged particles are formed by inelastic collisions between neutral atoms and these accelerated electrons. In opposite to elastic collisions, these inelastic collisions lead to ionisation of atoms. New generated ions are accelerated through the electric field force. So they gain energy and collide with neutral atoms and ionise them. This sum of ions is accelerated along the electric field towards the cathode. With a certain probability they produce secondary electrons after impact. This leads to a multiplication of charge carriers which means an increase in current while the voltage remains constant. During the charge carrier generation annihilation of positive and negative carriers takes place. The gas discharge process is self sustaining, if more charge carriers are generated then the probability of annihilation is higher. Figure 2.1 shows a typical I-V curve of a glow discharge with its

L. Hädicke

fields of Townsend-, normal-, abnormal- and arc discharge. If the number of generated charge carriers is equal to the number of the removed ones, a steady state situation is reached, which is called Townsend-Discharge. At higher currents, the normal glow discharge region follow the gas starts to glow, the voltage decreases and the current rises immediately. The current is proportional to the electrode area and is covered by the glow discharge. If the total electrode area is covered with the glow discharge, the abnormal glow discharge region is reached. This is utilized for a lot of sputter deposition processes. Behind this area, the voltage decreases and the glow discharge changes into an arc discharge [9,17,83].

In front of the cathode a significant descend of the potential occurs, see Figure 2.2. This is named cathode fall and is of the utmost importance for a glow discharge, as herein sufficient electrons have to be emitted and accelerated. In the same way, the arriving ions obtain a velocity high enough in order to eject secondary electrons from the cathode. Consequently, the cathode fall is decisive for a continuous discharge. Normally, the cathode fall has a greater magnitude than its anodic counterpart and is restricted to the close surrounding of the electrode. In case of glow discharges, the cathode mechanism almost entirely depends on the emission of secondary electrons by fast ions, whereas primary processes are negligible [10]
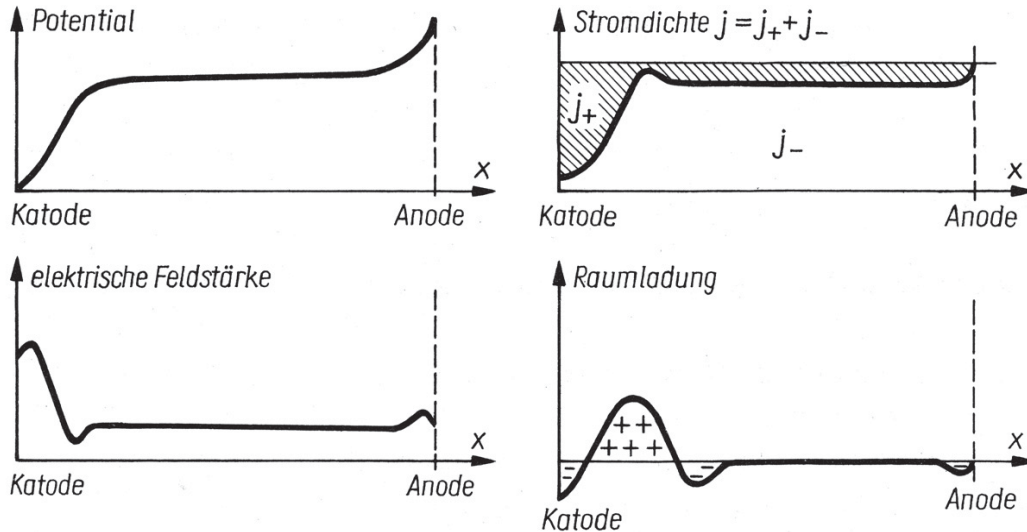

Figure 2.2: a) Distribution of potential and electrical field strength, b) current density, and space charge of discharges [10]

L. Hädicke

1.3   Sputtering

As it is described above, the ions of the working gas are generated by collision of accelerated free electrons with neutral particles. The ejected and decelerated electrons may be accelerated again by the electric field, and may collide again. Subsequently, the amount of charge carriers multiplies. The Ar+ ions accelerate towards the negative cathode, whereas the electrons are move towards the substrate. The Ar+ ions are the charged particles which are responsible for sputtering of the target surface atoms. The ejected atoms distribute randomly in the deposition chamber and condense onto cold surfaces like the substrate. Figure 2.3 shows the basic processes that usually occur while sputtering [9,10,83].
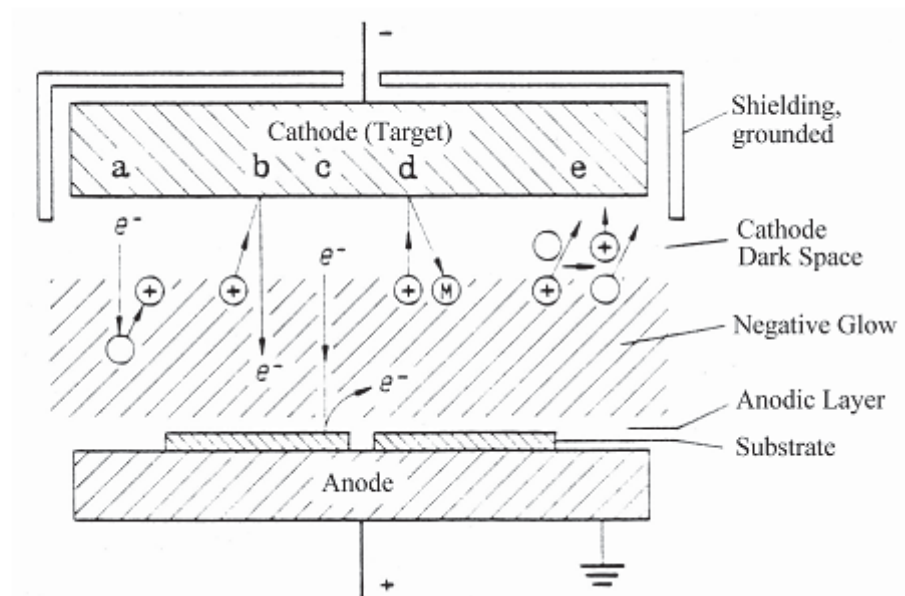

Figure 2.3 Particle interactions which can occur during sputtering [83].

An important factor which characterizes the processes performance is the sputtering yield - the number of atoms ejected per incident ion. This value is depending on the angle of incidence, mass ratio, surface energy, the condition of the target (roughness, crystalline structure, temperature) and the target material's sublimation heat [19]. This effect can be utilized by changing the polarisation, for surface cleaning (substrate works as cathode); here, the mechanism is named ion etching and is widespread in industry as sample cleaning step [10].

L. Hädicke

1.3.1   Magnetron sputtering

In the magnetron sputtering process, a magnet is placed behind the target. Magnetrons are classified into circular, cylindrical or planar magnetrons [18]. This permanent magnetic field is confining and concentrating the plasma and leads to "racetrack" area close to the target due to trapping of the electrons by the induced magnetic field. Figure 2.4 shows schematically a planar magnetron. The movement of the charged particles is influenced by the interaction of the electrical and the magnetic field by the Lorentz-force. The electric field acts perpendicular, the magnetic field above the racetrack parallel to the target. The electrons move on a cycloidal path with a higher concentration of charged particles than at other areas. This leads to higher ionisation efficiency at the racetrack. Hence, the positive ion formation rate is enhanced and the probability of electron loss by wall reactions is decreased. As a result, the deposition rate at lower working gas pressures increases and for this reason the deposition time decreases.[6,11]
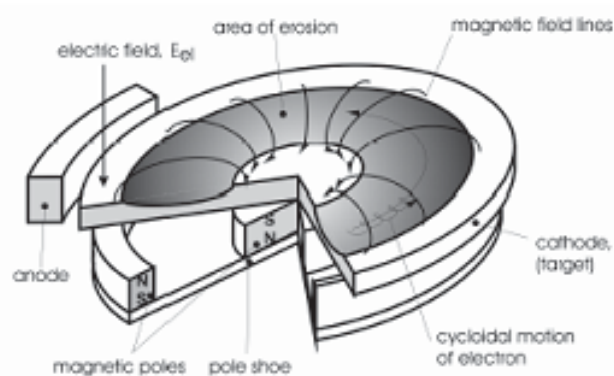

Figure 2.4: Schematic of a planar magnetron [75].

If all the magnetic field lines are confined between the concentrically arranged magnets of the planar magnetron configuration, they are balanced against each other, therefore, named conventional balanced magnetrons (CBM). On unbalanced magnetrons, the magnetic field lines are not self confined. Consequently they are partially open towards the substrate [12,13]. As a result, fast secondary electrons accelerating away from the cathode follow the magnetic field lines, move away from the target and collide with gas, as displayed in Figure 2.5
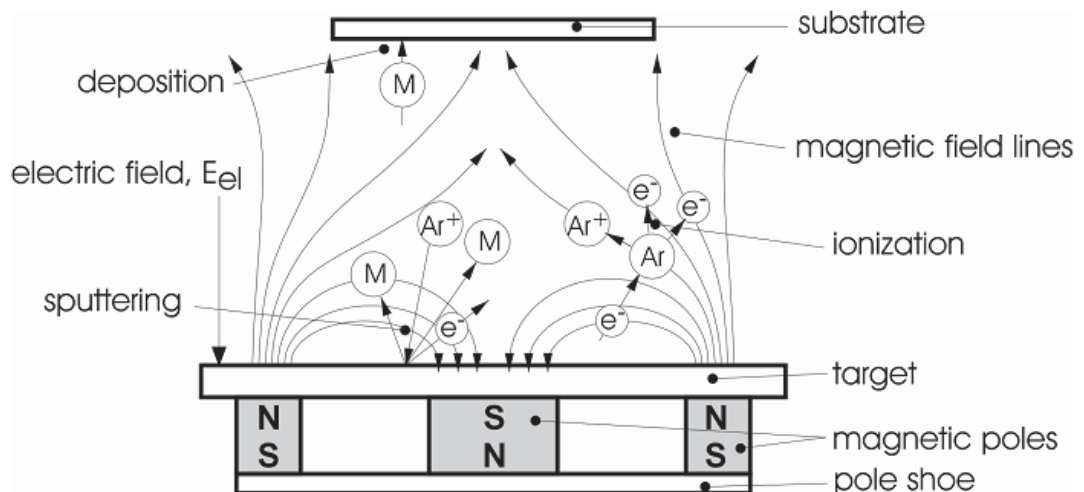
L. Hädicke

Figure 2.5: Schematic of the unbalanced magnetron configuration [21].

1.3.2 Reactive magnetron sputtering

Reactive coating facilities take advantage of the high chemical reactivity of particles that participate in the discharge. A reactive gaseous component or mixture of N_2, CH_4, or O_2 is added to the working gas (usually argon), becomes part of the plasma, and contributes actively to the process of film formation [11]. In general, the deposition rate decreases if the partial pressure of the reactive gas, is increased. In contrast to nonreactive deposition, the interactions at the target are different, as a reaction of the additional gaseous phase results in compound formation. These compounds can, depending on the flow rate, completely cover the sputtering area, and consequently lead to a degradation of the deposition rate. This effect is termed target 'poisoning', and strongly depends on the specific target material -reactive gas combination and their compound properties. [8,11].

The main reasons for this behaviour are the different sputtering and secondary electron emission yields of such compounds, whether oxide or nitride, compared to their pure targets. Moreover, the formed compounds may not have well electrical conductivity leading to uncontrolled arcing. This arc discharge results in evaporation of the compound and parts of the target material. Similar processes may happen at the substrate. The most preferable requirement for a reactive process is that the compound phase forms only at the substrate and not at the target surface. Introducing the inert atmosphere close to the target circumvents that if the s the reactive gas inlet is placed near the substrate. Intensifying the plasma close to the substrate additionally increases the probability of reactions of the substrate area. The use of

L. Hädicke

unbalanced magnetrons that expand the plasma area close to the substrates may accomplish that [11,13].

In our case artificial air with an N_2 to O_2 ratio of 4/1 was used as working gas.

1.4 Nucleation and growth

Properties of thin films are highly determined by their microstructure. In particular, in the case of coatings produced by condensation from the vapour phase, the properties are normally different to their bulk counterparts. The nucleation and growth processes, which occur during the deposition process, determine these properties and the final structure of the coating. Generally, the substrate and the deposited coating have different chemical compositions. Therefore, there is no instant condensation possible, if atoms from the vapour phase impinge on the substrate surface. In the following, two different interactions are possible: either the atom is reflected from the surface or adsorption on the surface occurs. Condensation takes place, if several adsorbed atoms combine and form small clusters, also called nuclei. The cluster formation itself is called nucleation. Growth is the following extension of the nuclei to form a coherent film. Nucleation and growth often occur at the same time during coating deposition. The sequence of the nucleation and growth process can be divided into the following steps [22,23,24]:

Nucleation:
- Formation of adsorbed monomers
- Formation of subcritical embryos of various sizes
- Formation of critically sized nuclei (nucleation step)
- Growth of these nuclei to supercritical dimensions with the resulting depletion of monomers in the capture zone around them
- Concurrent with the previous steps there will be nucleation of critical clusters in areas not depleted of monomers
- Clusters touch and coalesce to form a new island occupying an area smaller than the sum of the original two, thus exposing fresh substrate surface
- Monomers adsorb on the freshly exposed areas and 'secondary' nucleation occurs
- Large islands grow together, leaving channels or holes of exposed substrate
- The channels or holes fill via 'secondary' nucleation to give a continuous film

L. Hädicke

Crystal growth:

- Coalescence of individual crystals on the substrate and grain boundary migration in the polycrystalline structure

As shown in Figure 2.6, the impinging atoms arrive on the substrate surface with material and deposition system depending arrival rate. As mentioned above, either the atoms are now reflected from the surface or become loosely bonded 'adatoms'. The adatoms, which transfer their kinetic energy to the lattice, may diffuse on the substrate surface for a while, before they either get desorbed again or become trapped at low-energy lattice sites. The adatom mobility is controlled by the kinetic energy of the adatom, the temperature of the substrate and the bonding strength between substrate and adatom. At very small arrival rates, the coverage is small which inhibits nucleation or film formation. Therefore, an equilibrium between adsorption and desorption is reached. High arrival rates lead to the formation of metastable and sTable clusters. The clusters grow by addition of other arriving atoms from the substrate surface or directly from the vapour phase. Bulk diffusion of incorporated atoms to readjust their position is possible as well. Meeting clusters combine by growth or motion. This coalescence results in the formation of a more or less dense coating [3,20,25].
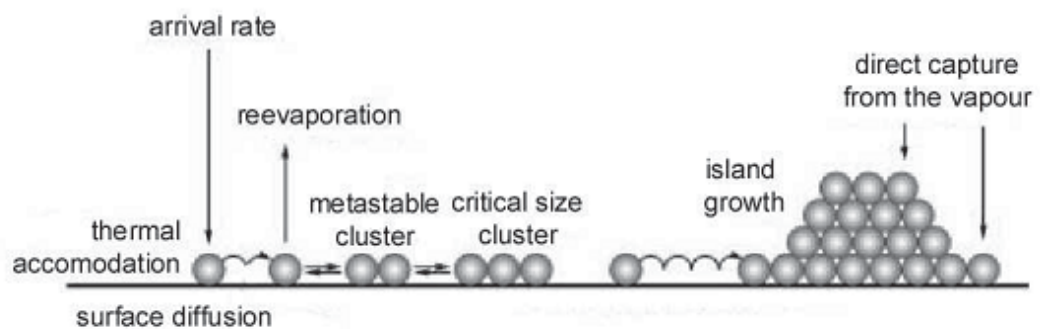

Figure 2.6 Schematic overview of the principles of nucleation and growth processes [26].

Many observations of subsequent film formation have pointed to three basic growth modes (1) island (or Volmer-Weber), (2) layer (or Frank–Van der Merwe), and (3) Stranski-Krastanov. Island growth occurs when the smallest sTable clusters nucleate on the substrate and grow in three dimensions to form islands. This happens when atoms or molecules in the deposit are more strongly bound to each other than to the substrate. The opposite characteristics are displayed during layer growth. Here the extension of the smallest sTable

L. Hädicke

nucleus occurs in two dimensions, resulting in the formation of planar sheets. In this growth mode the atoms are more strongly bound to the substrate than to each other. The first complete monolayer is then covered with a somewhat less tightly bound second layer. Providing the decrease in bonding energy is continuous toward the bulk crystal value, the layer growth mode is sustained. The layer plus island or Stranski-Krastanov (S-K) growth mechanism is an intermediate combination of the preceding two modes. In this case after forming one or more monolayer, subsequent layer growth becomes unfavourable and islands form [25,20].

These growth modes can be explained from an energetic point of view, when the surface tension is plotted against the lattice mismatch, Fig 2.7.
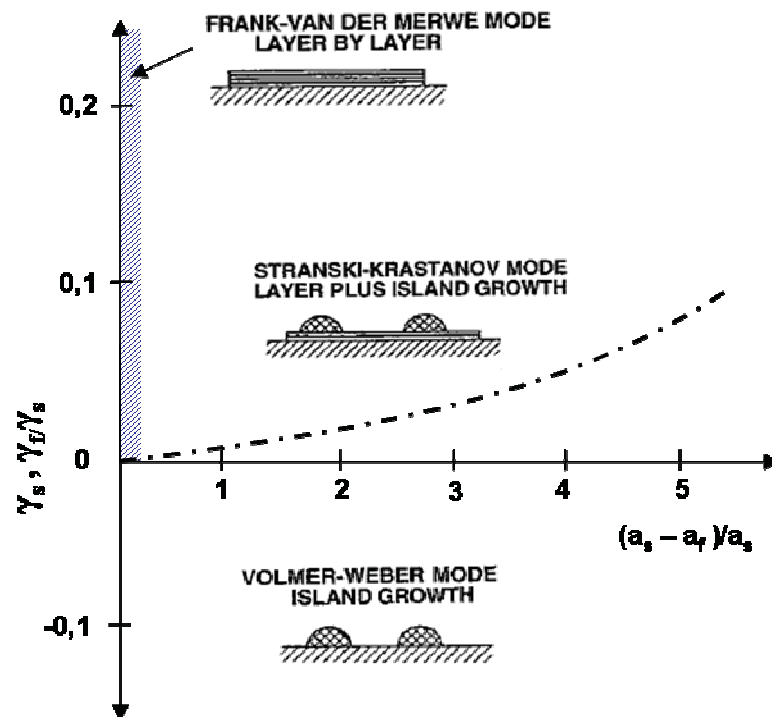

Figure 2.7 Stability regions of the three thin film growth modes in coordinates of surface energy difference between substrate and film (vertical) and lattice misfit (horizontal) [76].

L. Hädicke

1.4.1   Structure zone models

In the late 70's investigations on thick coatings were made. The correlation between coating structure and deposition parameters are defined in Structure Zone Models (SZM). In this way, morphology and microstructure of a film can be predicted as a function of adatom mobility independent on the material. Shadowing, desorption, surface and bulk diffusion as well as recrystallization are the basic processes of nucleation and growth of films. Shadowing is caused by the interaction of surface roughness and the angle of incidence of the arriving atoms. It prevents a constant coating for all areas of the surface [2]. A quantification of these basic processes is possible by the characteristic surface roughness, the activation energy of surface and bulk diffusion, and the sublimation energy. There is a correlation between these energies and the melting point T_m for many pure metals. The basis of structure zone models is that several of these basic processes can be expected to dominate a certain field of homologous temperature (T/T_m) ranges, with T being the substrate temperature, T_m the melting temperature [2, 3]. The first structure zone model was defined by Mochvan and Demchishin (1969). They defined three different structural zones with distinct properties and structures, and investigated the influence of substrate temperature on condensation, structure and properties [27]. Thornton (1977) took the effect of the sputtering gas pressure (argon) into account. As shown in Figure 2.7 (a), he also introduced a transition zone T between zone I and zone II. Due to the increasing number of collisions between particles with increasing gas pressure, the kinetic energy of the impinging adatoms decreases. Messier et al. modified the Thornton model (see Figure 2.7 (b)) by taking the influence of the energy of the impinging ions into account. The ion bombardment induces mobility of the surface atoms, which leads to a broadening of zone T in the lower temperature range [28,29].
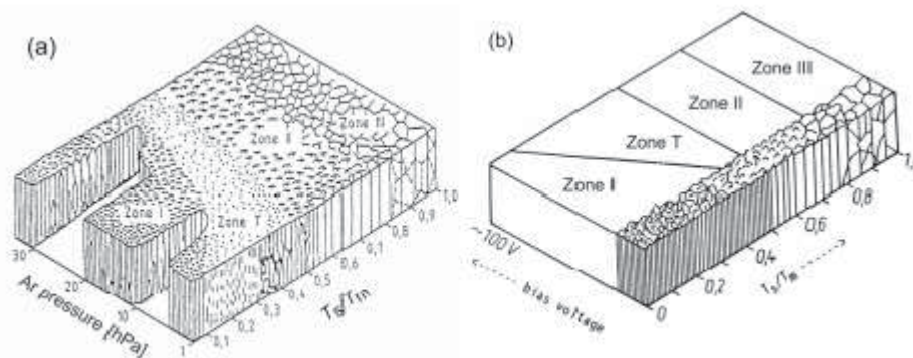

Figure 2.7 (a) Structure zone model after Thornton [29] and (b) after Messier et al. [28].

L. Hädicke

1.4.2   Nanocrystallinity

Nanocrystalline materials are polycrystalline with an average grain size below 100 nm. So the main structural feature is described in a nanometer scale [30]. This leads to a high volume fraction of grain boundary phase. The properties of such a structure differ widely from the same material with larger grains. This structure is achieved by setting the appropriate depositing parameters. One way to produce this structure is displayed in Figure 2.8 where influence of the ion bombardment during the growth process is shown.
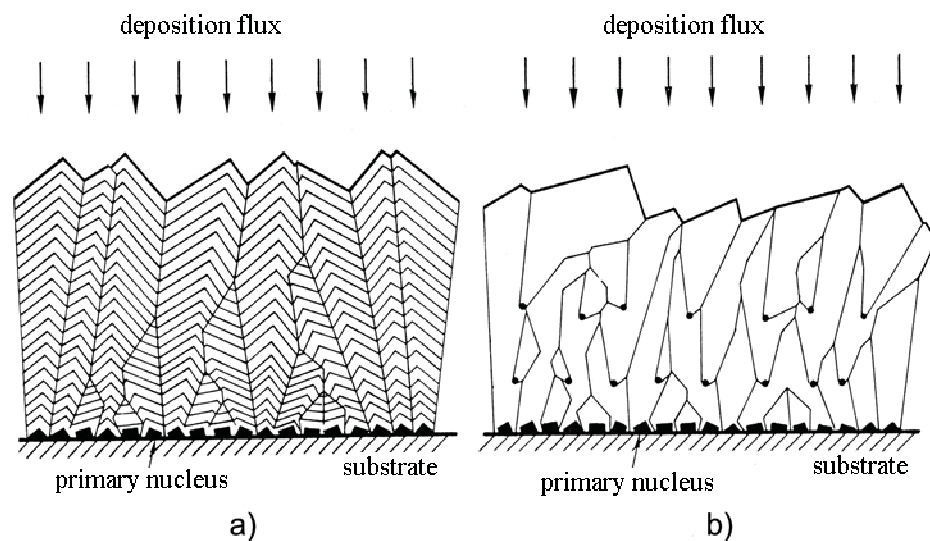

Figure 2.8 Film structure growth at elevated surface diffusion in dependence of a repeated nucleation [31].

At a high surface diffusion, caused by elevated temperatures or energy transfer through ion bombardment, a dense columnar structure evolves as visible in Figure 2.8 (a). With an increase of the number of the impinging ions or their energy the defect density would increase. This higher defect density promotes in turn the nucleation. In succession, nuclei which are not located in the film-substrate interface are formed. This leads to a dense nanocrystalline film, Figure 2.8(b).

Another approach producing nanocrystalline films is to select an appropriate chemical composition which is forming more than one phase which constrain each other in their growth. By continuous nucleation, growth and opposite disablement during growth a multiphase nanocrystalline structure is produced (nanocomposite). Barna et al. [31] investigated this influence and displayed it in a SZM (Figure 1.9) where the dependence of impurities is shown.
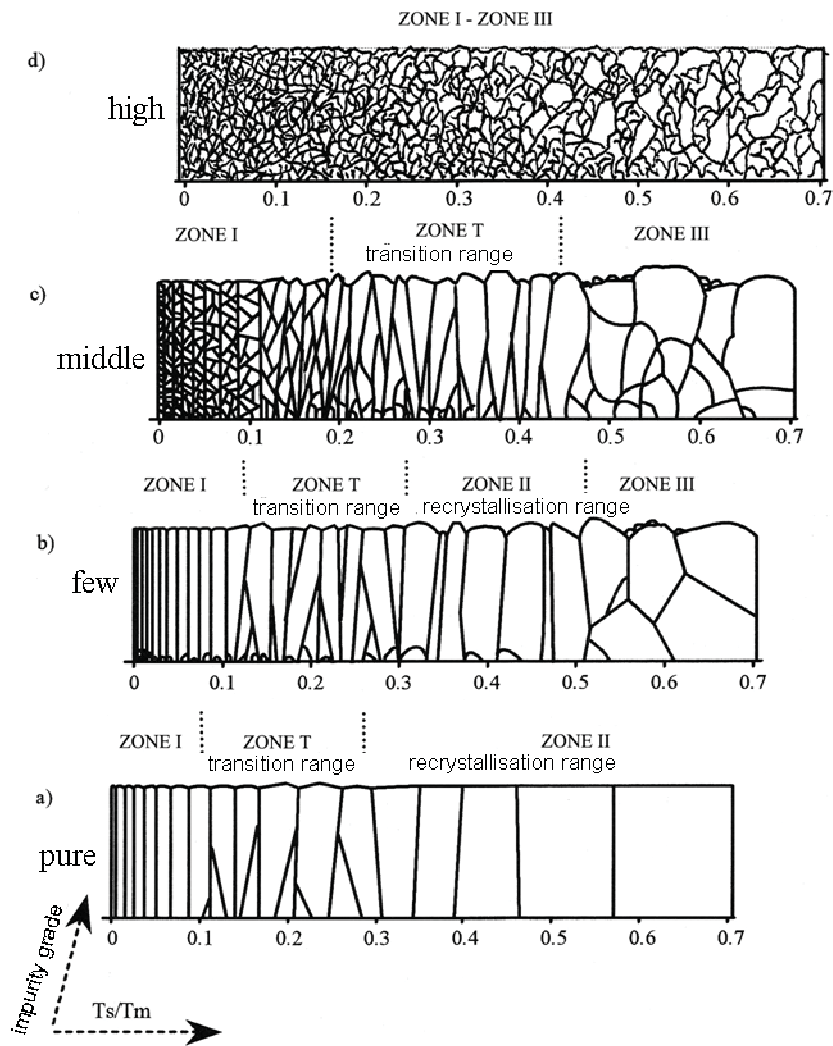
L. Hädicke

ZONE I - ZONE III

d)

high

| 0 | 0.1 | 0.2 | 0.3 | 0.4 | 0.5 | 0.6 | 0.7 |

ZONE I   ZONE T   ZONE III
transition range

c)

middle

| 0 | 0.1 | 0.2 | 0.3 | 0.4 | 0.5 | 0.6 | 0.7 |

ZONE I   ZONE T   ZONE II   ZONE III
transition range   recrystallisation range

b)

few

| 0 | 0.1 | 0.2 | 0.3 | 0.4 | 0.5 | 0.6 | 0.7 |

ZONE I   ZONE T   ZONE II
transition range   recrystallisation range

a)

pure

| 0 | 0.1 | 0.2 | 0.3 | 0.4 | 0.5 | 0.6 | 0.7 |

impurity grade

Ts/Tm

Figure 2.8 SZM after Barna, et al.[31], Dependence of the evolving structure from the concentration of foreign atoms rather impurities.

The term impurities include species which are deposited or incorporated in the film, which are over their solubility or stoichiometry. If a crystal is covered with such impurities further growth is blocked and this leads to formation of another new crystal. When a frequent re-nucleation occurs small grains are the result. The impurity grade increases this effect and finally increases the volume fraction of the grain boundary phase.

2 Thermally activated processes

Every process which needs thermal energy is thermally activated. In condensed matter in particular there are processes where atoms change their lattice sites. For a change in the site these atoms need a place to change to. This can be interstitial vacancies, vacancies or other void imperfections [32].

Thermally activated processes are diffusion, recovery, nucleation, spinodal decomposition, recrystallisation and grain growth.

2.1 Diffusion

A mixture of several different atoms is reaching its thermodynamically equilibrium by reaching the equilibrium concentration. This is described by Fick's first law that notes that the flux is direct proportional to the concentration gradient [33].

Diffusion is the thermally activated lattice site change of single atoms. This transposition commonly happens with vacancies. Diffusion of interstitial atoms is only for interstitial solid solutions important. The different mechanisms of diffusion are displayed in Figure 3.1. The interstitial mechanism occurs with small alloy elements, like, H, C and N which find enough space in interstitial lattice vacancies. Without the influence of a concentration gradient the self diffusion in a substitutional solid solution has the highest significance. Hence, dependency from the vacancy concentration is very high [33]. This strong dependency is recognizable in thermally activated processes of PVD sputtered thin films which have a high concentration of vacancies and imperfections and are therefore far from their thermodynamic equilibrium [34].
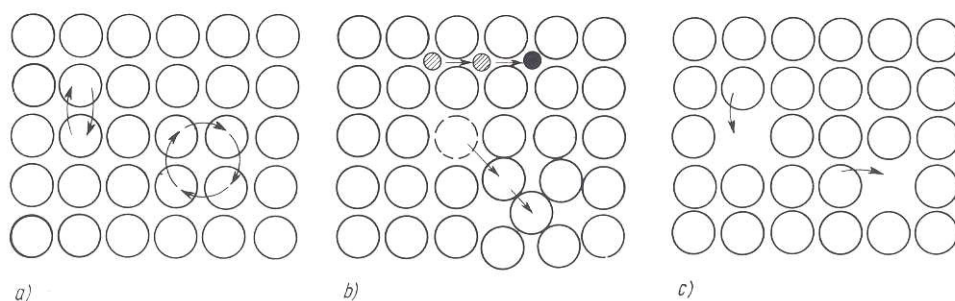

Figure 3.1: Diffusion mechanism: (a) transposition; (b) interstitial transposition; (c) vacancy mechanism [35]

L. Hädicke

2.2 Recovery

All crystallographic imperfections which are not in thermodynamic equilibrium have the tendency to heal through energy input. These effects have a great technical relevance because of their influence on the properties of the material through annealing. The possible recovery processes are displayed in Figure 3.2 [36,37].

Recovery is basically the different types of interaction of dislocations due to their long range stressfield. If two dislocations have an opposite pressure and tension field they will attract each other. If the fields are located on the same slideplain they will annihilate. Through this mechanism the dislocation density decreases. If they are not located on the same slideplain they can climb or cross slip when they are thermally activated and will annihilate then. On the other hand when they have the same sign they can minimize their energy by arranging over each other. This arrangement is named low angle grain boundary [36].
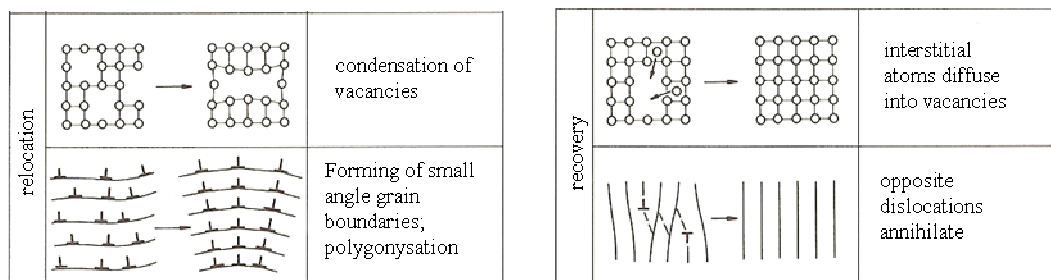

Figure 3.2: Possible mechanism of recovery [36].

Subgrains are formed which show growth at elevated temperatures. This process is called polygonisation. At higher temperature or more thermal energy input these low angle grain boundaries can aggregate to high angle grain boundaries.

Recovery is conducted through dislocation climbing and cross sliding. These processes are highly dependent on the stacking fault energy [33].

L. Hädicke

2.3 Recrystallisation

Opposite to recovery, recrystallisation triggers grain and structure regeneration. The kinetic of the recrystallisation is determined by the thermal activation energies of nucleation and growth. Primary recrystallisation is performed by the recrystallisation nuclei and their growth. The formation of the recrystallisation nuclei needs three criteria to be fulfilled. These are called the laws of recrystallization.

Thermodynamic instability: The nucleus must have critical size so that its enlargement must lead to a decrease of its energy. This is possible because the surface energy increases with power of two but the volume energy decreases with power of three. This makes a larger nucleus thermodynamically more Table.

Mechanical instability: There must be a local unbalance in the driving force to give the grain boundary a selected direction of motion.

Kinetic instability: The boundary surface must be free to move. This is only possible with high angle grain boundary. The formation of this boundary is the most complex step of the recrystallization nucleation.

These three criteria are easy to fulfill if there are already deformation inhomogeneties and high angle grain boundaries. All processes, which are needed to fulfill these criteria, are supposed to have local rearrangement of dislocations. This is aligned with recovery which happens always before nucleation. The incubation time is the time where recovery takes place. When a nucleus is formed it will grow into the deformed structure by assimilating atoms from the dislocation dense area and incorporate them in the recrystallized structure. If the growing grains hinder each other the primary recrystallisation is completed. This results into a polycrystalline dislocation depleted structure [33].

L. Hädicke

2.4   Nucleation and spinodal decomposition

The process of decomposition can either be performed by nucleation and growth processes, by forming a nucleus with the equilibrium composition, or by spontaneous decomposition where the equilibrium composition is reached after some time. If a phase has a composition near a minimum of the free enthalpy graph G(c) like c_1 in Figure 3.3 so decomposition would lead to an enhancement of the enthalpy G_1 to G_{1E}. Hence, such decomposition would be in Table and the system changes its composition back to the homogeneous state.

At a composition close to the maxima of the free enthalpy graph G(c) every decomposition is leading to an energy reduction. From G_3 to G_{3E} the energy reduction continues till no more energy reduction is possible.

This shows that a fluctuation of concentration is potentiated what leads in a spontaneous decomposition. This is called spinodal decomposition where the diffusion flux flows against the concentration gradient [32,33,36].
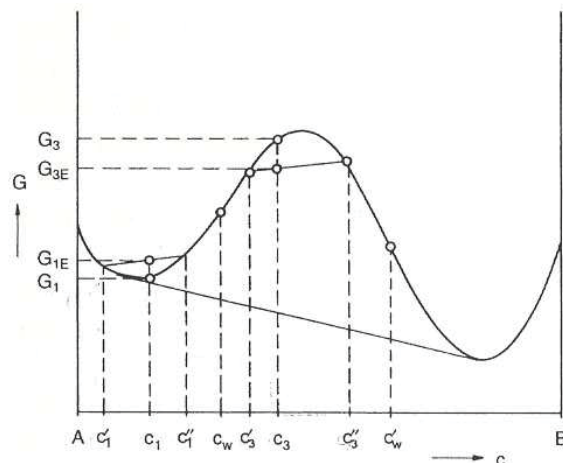

Figure 3.3: Change of the free enthalpy through decomposition [33].

The difference between spinodal decomposition and nucleation is clarified in Figure 3.4. At the nucleation the critical nucleus size with equilibrium concentration has to be reached for growth. Hence, the reason for the incubation time on the other hand the spinodal decomposition is reacting spontaneously (without incubation time) whereas the equilibrium composition is reached later [32,33,36].
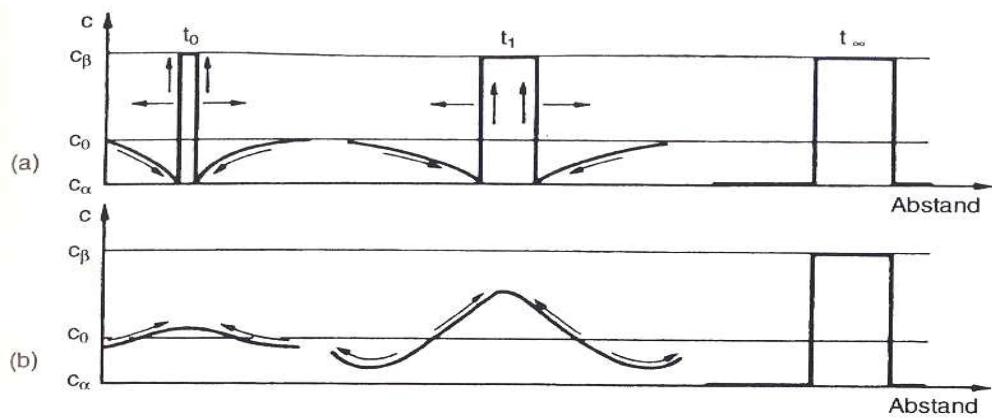
L. Hädicke

Figure 3.4: Schematic characteristics of the concentration variation and the dimension of the decomposition when (a) nucleation and (b) spinodal decomposition occurs [33].

The spinodal decomposition is only possible when the free enthalpy graph is curved concave between cw und c´w. In the range between the turning points and the solubility limit the decomposition occurs through nucleation and growth, so the nucleation energy has to be dedicated.

L. Hädicke

3 Thin film materials

3.1 Zr-Al-Y-N

Transition metal nitride coatings have been commercially available for many decades, and offer a combination of high hardness, high thermal stability, reasonably good high temperature strength and oxidation resistance [38,39,40]. Among well investigated ternary Me-Al-N (Me, transition metal) systems the Zr-Al-N system shows only few studies. It is known that ZrN has a lower friction coefficient than TiN and other transition metal nitrides, and is relatively hard [41,42]. The, compared to other coatings, poor oxidation resistance hindered a broader use. This was tried to circumvent by alloying ZrN with Al to improve the oxidation resistance and the mechanical properties [43]. The $Zr_{1-x}Al_xN$ (fcc, NaCl-type) solid solution has an existence range from x=0 to 0.43 and shows an increase of hardness trough solid solution hardening from 21 to 28 GPa [44]. With higher Al contents the hexagonal close packed AlN appears (hcp, ZnS-type) and the hardness decreases. S. Veprek et al. [45] calculated the binodal and spinodal decomposition curve of metasTable fcc $Zr_{1-x}Al_xN$ and came to a decomposition into fcc ZrN and fcc AlN. But due to interfacial strain the fully coherent spinodal decomposition may be hindered and decomposition into fcc ZrN and hcp AlN is more preferable.

3.2 Zr-Al-Y-O-N

The need of sTable coatings during a temperature cycling at around 1500°C leads to Y stabilized ZrO_2 (YSZ) which shows low thermal conductivity and a high thermal expansion coefficient. This insulating ability and low-level mismatch during service temperature gave YSZ a broad use as thermal barrier coating (TBC). These TBCs are utilized on turbine engine components to increase the operation temperature. The operation temperature can be enhanced over 100° what is equal to about 3-4 times of service life [46,47,48]. The phase transition temperatures of pure ZrO_2 are shown in Figure 4.1.
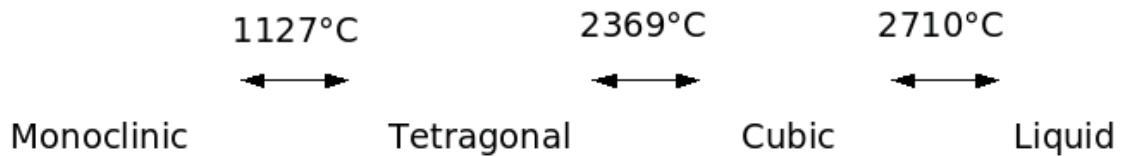
L. Hädicke

Figure 4.1: Phase transformations of ZrO_2 at elevated temperatures [49, 50, 51].

The high temperature cubic and tetragonal phase can both be stabilized to room temperature by doping it with oxides like CaO, MgO or Y_2O_3. These dopants decide over the existing phases and the microstructure which are very important for many features like thermal conductivity, fracture toughness and strengths.
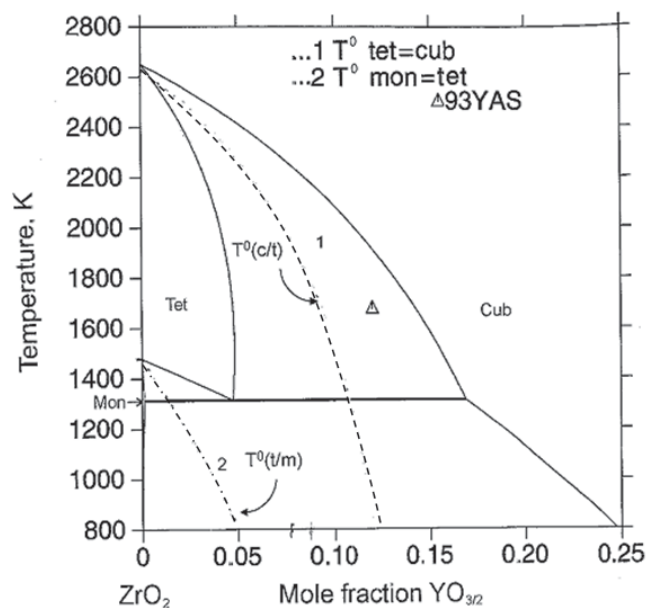

Figure 4.2, Phase diagram of ZrO_2 and $YO_{3/2}$ and the indicated existence area of YSZ between T°(t/m) and T°(c/t) from [52].

The existence of the tetragonal phase of ZrO_2 is deciding about the thermal stability during the cycling. The tetragonal – monoclinic transformation which shows a volume expansion of 4 % has a destructive influence on the material. So the alloying with $YO_{3/2}$ (i.e., Y_2O_3) gives a possibility to stabilize the tetragonal phase of ZrO_2 [52]

L. Hädicke

4 Experimental

4.1 Film deposition

4.1.1 Magnetron sputter device

All films investigated in this work were produced by DC-reactive magnetron sputtering, using a modified Leybold-Heraeus A-400 magnetron sputtering unit. Explanations to the operation mode are listed in [52-56]. The facility is displayed in Figure 5.1.
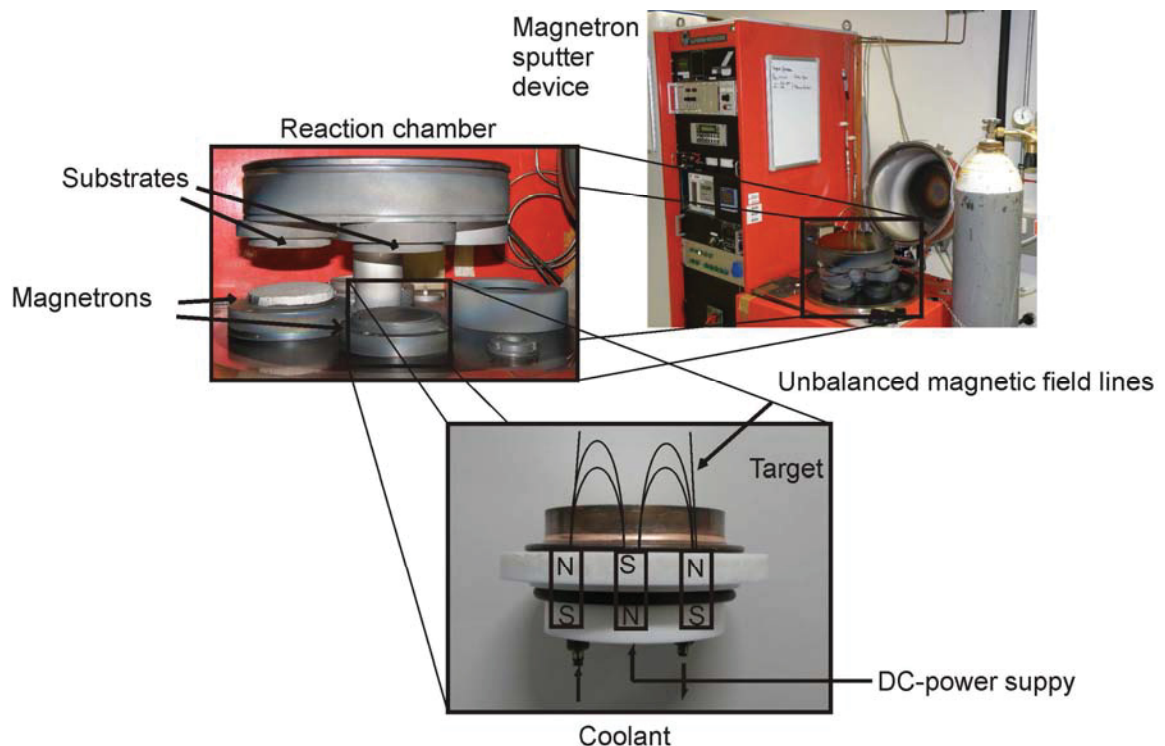

Figure 5.1: Leybold-Heraeus A-400 magnetron sputtering unit.

4.1.2 Reaction Chamber and cathodes

The chamber (420x200 mm) consists of two parts and a cover. The rotaTable upper-part contains the substrate holder, which can be heated up to 550°C and charged with a bias voltage. RF–etching power is applied on the substrate holder through a switching-system. The lower part at the reaction chamber holds the magnetrons (Figure 3.1), contains the pump

L. Hädicke

flange, the pressure measure tubes and the gas inlet. All three cathodes are located at the bottom of the chamber. They are isolated and sealed against the chamber with a Teflon base plate. Furthermore, they have a circular permanent magnet system (Gencoa PK 75) and water cooling system. The cathode power supply is a Leybold-Heraeus DC-generator. For a good thermal and electrical conductivity the targets are bonded with Indium to the cathodes.

4.1.3   Vacuum system

The reaction chamber is evacuated by a pre-vacuum pumping system (rotary vane vacuum pump Pfeiffer DUO 20) and a turbomolecular pump (Leybold Turbovac 361), which is controlled and supplied by a (Leybold Turbotronic NT 20) frequency changer.

4.1.4   Atmosphere control system and pressure measurement

The chamber pressure was measured by a Leybold Combivac CM 31. Two gas flow control units (Tylan RO-7031, controller Tylan RO-7030) were used to adjust the working gas flow between 0 and 200 sccm (standard cubic centimetres) and the N_2 and reactive gas flow between 0 and 50 sccm.

4.1.5   Power supplies

A Leybold-Heraeus DC-sputter generator is integrated in the basic system and enables a continuous DC-power regulation of the plasma. For RF-sputter cleaning prior to deposition, an RF-generator (ENI ACG-6B) was used. The bias voltage during deposition was applied by a DC-bias generator (Sorensen DCR 300-1.5).

L. Hädicke

4.1.6   Substrates and targets

The utilized substrates are listed in Table 5.1.

Table 5.1: The utilized targets, their composition, dimension and their purpose of investigation.

Substrates	Composition	Dimension [mm]	Purpose of investigation
Sapphire	Al2O3 (1$\bar{1}$20)	10*10*0.5mm	High temperature phase evolution, structure
Low-alloyed steel	DIN 1.0330	Ø 75*0.05mm	Phase stability , thermal activated processes
Silicon	Si (100)	5*17*1mm	Thickness evaluation, structure, hardness evaluation

The targets used for deposition are listed in Table 5.2 containing the composition and the purity.

Table 5.2: The utilized targets, their dimension and their composition

Target composition	Dimension [mm]	Purity [%]	Manufacturer
$Zr_{0.67}Al_{0.33}$	Ø 75 mm	99.9%	Plansee S.E,
$Zr_{0.66}Al_{0.32}Y_{0.02}$	Ø 75 mm	99.9%	Plansee S.E,
$Zr_{0.64}Al_{0.31}Y_{0.05}$	Ø 75 mm	99.9%	Plansee S.E,
$Zr_{0.60}Al_{0.30}Y_{0.10}$	Ø 75 mm	99.9%	Plansee S.E,
$Zr_{0.60}Al_{0.30}Y_{0.10}+$ Yttrium-platelets	Ø 75 mm + 5*17 mm	99.9%	Plansee S.E,

L. Hädicke

4.1.7   Deposition parameters

All films were produced under the same conditions except for the low-alloyed steel substrates, were no RF-etching was applied prior to deposition. The sapphire and the Silicon substrates were etched prior to depositing with the parameters listed in Table 5.3. The variable etching parameters were the cathode power (P_K), the total pressure (P_{tot}), the deposition temperature (T_{dep}), Ar flow and the deposition time (t_{dep}).

Table 5.3: Parameters for etching.

P_K [W]	Ar flow [sccm]	P_{tot} [Pa]	T_{dep} [°C]	t_{dep} [min]
300	40	$\sim 1*10^{-2}$	500	8

The deposition conditions are listed in Table 5.4. For ZrAlYON films the gas flow was kept constant but instead of pure N_2, synthetic air was utilized as reactive gas component consisting of 80% N_2 and 20% O. Additionally to the parameters adjusted during etching following parameters were used during deposition: the magnetron power (P_m), the bias voltage (U_{bias}), the N_2 flow and the flow of the used synthetic air (P_{air}).

Table 5.4: Deposition parameters.

System	P_M [W]	U_{bias} [V]	Ar flow [sccm]	N_2 flow [sccm]	P_{air} ($N_2/O_2= 4$) flow [sccm]	P_{tot} [Pa]	T_{dep} [°C]	t_{dep} [min]
ZrAlYN	300	50	14	8.3	0	$\sim 2.9*10^{-3}$	500	180
ZrAlYON	300	50	14	0	8.3	$\sim 2.9*10^{-3}$	500	180

4.2   Film Characterization

4.2.1   Scanning electron microscopy (SEM)

A Zeiss Evo50 scanning electron microscope was used to investigate the sample surfaces and the morphology. Through cross-section SEM investigation the film thickness was measured. The chemical composition was determined by an attached Oxford Instruments INCA energy-dispersive X-ray analysis device (EDX).

L. Hädicke

4.2.2   Transmission electron microscopy (TEM)

General considerations

Many properties of materials are determined by their microstructure. Due to the nm-scale grain size of our samples the resolution of an SEM was too low to resolve individual grains. Therefore, in this thesis structural investigations were performed by cross-sectional transmission electron microscopy (XTEM). Which allows to generate images, from the cross section of the samples with the TEM with a resolution in the order of 5 Å [57].

For the investigations a FEI Tecnai G2 TF20 UT scanning transmission electron microscope (STEM), shown in Figure 5.2, with an EDX unit and electron energy loss spectroscope (EELS) attached was used. The electron beam path in a TEM is shown in a schematic drawing in Figure 5.2. The illuminating part, consisting of the field emission gun (FEG) and mainly two condenser lenses, is responsible for the incident highly coherent electron beam. The electron waves are forward-scattered and diffracted from the atoms of the investigated area and magnified in the imaging part. The optical resolution is largely limited by the resolution of the objective lens [58,59].
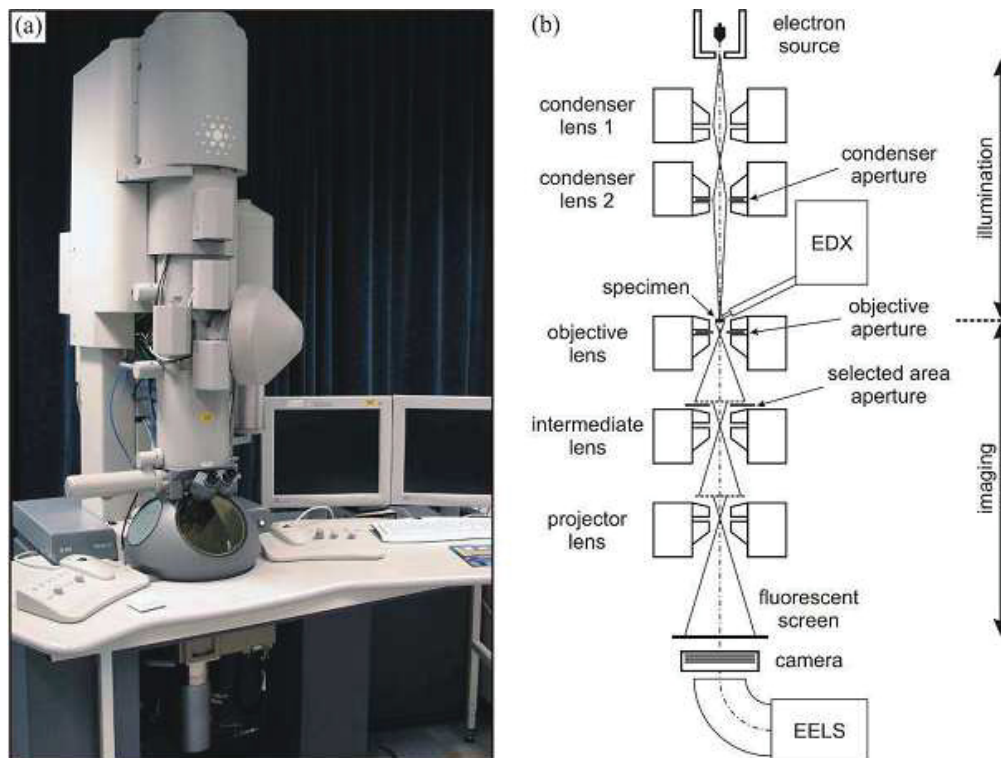
Figure 5.2: (a) TEM overview, (b) beam path of a High Resolution TEM (HRTEM) [77].

L. Hädicke

Changing the beam path allows to record diffraction patterns of an illuminated sample area. The obtained pattern is called selected area electron diffraction (SAED) and is completely equivalent to an X-ray diffraction pattern (XRD), see next chapter. By inserting an aperture the selected area can be very small and can thus be used to show the orientation of only a few crystallites. The interpretation of the SAED patterns is analogue to those of XRD patterns and is often used to obtain the interplanar spacing and therefore the Bravais lattice and phase composition of a material [60,61].
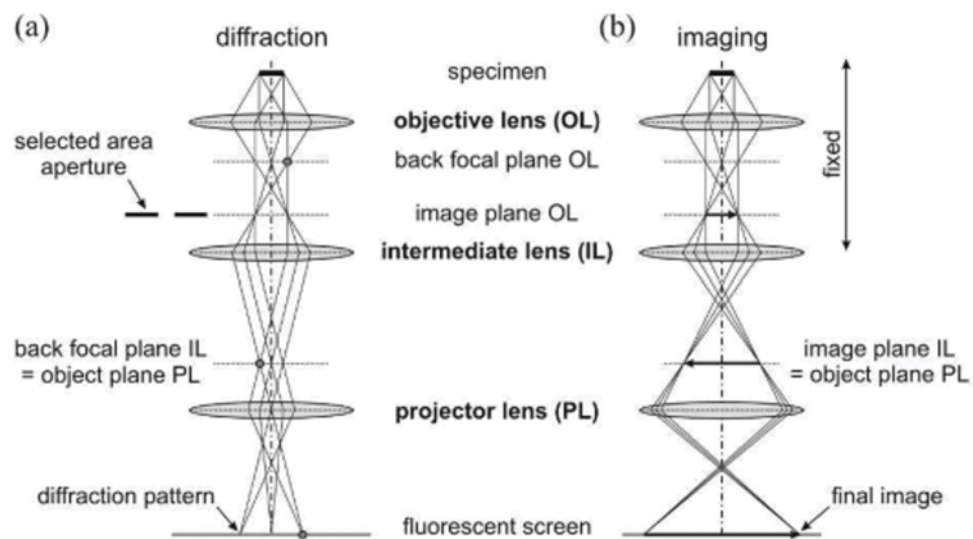
Figure 5.3: (a) beam path in diffraction mode, (b) beam path in imaging mode [77].

As TEM investigations require electron transparent sample thicknesses, special attention has to be paid on sample preparation which is listed in the following steps. On the basis of the need for electron transparent sample thicknesses the sample preparation got paid special attention.

- ◆ Cutting the coated substrates into two platelets of a size of 1.8*1 mm.
- ◆ Insertion of two platelets in a Ti-TEM-grid facing each other with the coated side.
- ◆ Fixing of the platelets in the disc with conductive glue.
- ◆ Grinding and polishing of the specimen disc down to a thickness of ~ 50 μm.
- ◆ Ar-ion polishing of the sample center in a Gatan precise ion polishing system (PIPS), with an energy of ~5 kV and at 5° angle from top and below, till a small hole emerged. Reducing the energy to ~2.2 kV for the last step gave a polished thin sample surface in the investigation regions.

L. Hädicke

4.2.3   X-ray diffraction

Since the beginning of the last century, X-ray diffraction (XRD) is the non-destructive method to determine the phase composition of solids and can also be used to perform stress analyzes and to determine grain sizes [62]. In dependence of wavelength, lattice spacing and lattice periodicity X-rays are scattered, leading to constructive or destructive interference. The basic condition for constructive interference, as a consequence of the periodicity of the lattice, is given by Bragg´s law [63].

$n * \lambda = 2 * d_{hkl} * \sin\Theta$ (5.1)

Where n is the value of order, λ is the wavelength of the X-rays, d(hkl) gives the lattice spacing with miller indices (h, k, l) and Θ is the incident angle.

Within this thesis, XRD was used to determine the different phases of the films deposited onto sapphire, powdered coatings (see chapter 5.2.4) and coatings after annealing by Differential Scanning Calorimetry and Thermogravimetry Analysis (DSC/TGA). Further the coatings thermal evolution was observed during in-situ high temperature XRD. The room temperature phase analysis was done using a Bruker D8 Diffractometer, according to the parameters in Table 5.5, in Bragg–Brentano mode, schematically shown in Figure 5.4. The in-situ HT-XRD measurements were performed by a Phillips X´pert MPD Diffractometer, combined with a Bühler HDK 2.4 high-temperature high-vacuum chamber with a Be-window.
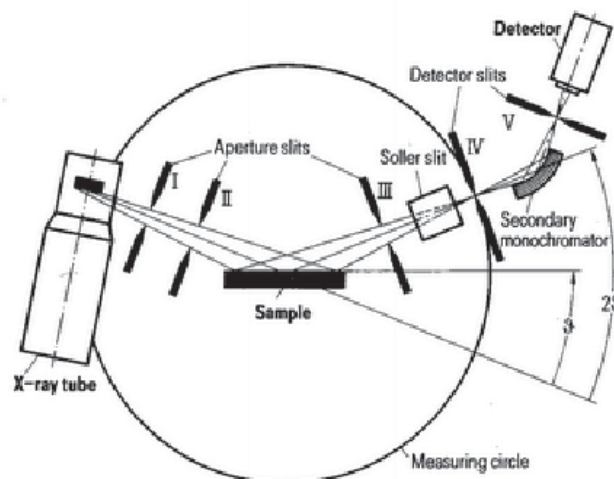
Figure 5.4: Schematic of an XRD with Bragg-Brentano configuration [64].

L. Hädicke

Table 5.5: XRD - parameters.

XRD-type	temperature	wavelength [Å]	voltage [kV]	current [mA]	timestep [s]
Phillips X´pert	high temperature	Cu Kα 1.54056	40	40	1.2
Bruker D8	room temperature	Cu Kα 1.54056	40	40	0.5

4.2.4 Differential scanning calorimetry (DSC) and thermo-gravimetric analysis (TGA)

Differential Scanning Calorimetry (DSC) is a technique to thermally characterize materials, such as metals and their alloys or coatings as within this thesis. This is achieved by measuring, as a function of time or temperature, the difference in heat flow a sample consumes (endothermic) or releases (exothermic) compared to a thermally inert reference material as a function of temperature or time. The term scanning refers to the fact that the sample is subjected to a user specified temperature program [65].

In this work a Netsch STA 409C system, schematically shown in Figure 5.5, and a Setaram STA were utilized. STA stands for Simultaneous Thermal Analysis. The equipment calibration is explained in detail in [21]. The Netsch STA 409C system was additionally equipped with a mass spectrometer, attached to the gas outlet. All samples where deposited on low-alloyed steel and it was possible to obtain free-standing material by dissolving the low-alloyed steel in 10 mol %-nitric-acid. Grinding the free-standing film material resulted in sample powders for testing. Only ZrAlYN: 1.1at%Y, 3.3at%Y and ZrAlYON: 0.8 at%Y, 1.4 at%Y, 10.6 at%Y where chosen for testing with the Netzsch unit to observe if volatile species occur during the heating.

L. Hädicke
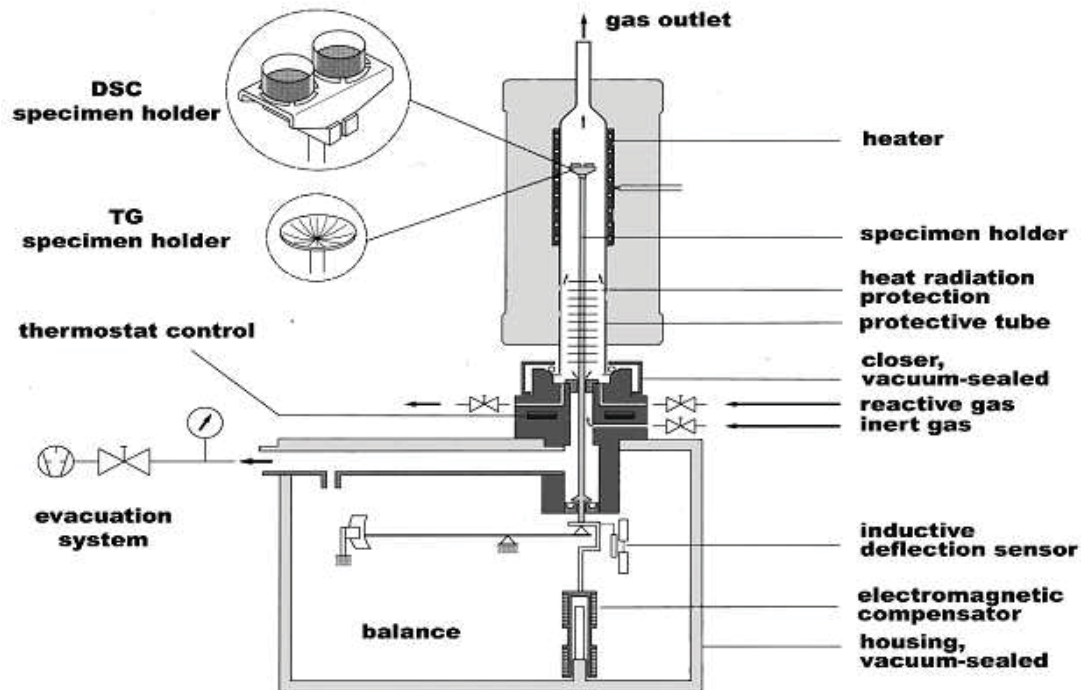
Figure 5.5: Functional scheme of the DSC/TGA/MS [78]

For DSC/TGA investigation, a Pt-Rh pan with an Al_2O_3 crucible was charged with the coating material and placed onto the DSC/TGA specimen holder of the Netzsch – or Setaram unit, respectively. The dynamic DSC experiments were carried out in an inert atmosphere of Helium to prevent the samples from oxidation. A so called heat-cool-heat-cool cycle was chosen to investigate the samples for their thermodynamic behaviour, as displayed in Figure 5.6. This allows to differentiate between reversible and irreversible reactions. Whereas the irreversible reactions, like mass loss or recovery only occur in the first heating, the reversible reactions like phase transitions occur in both heating cycles.
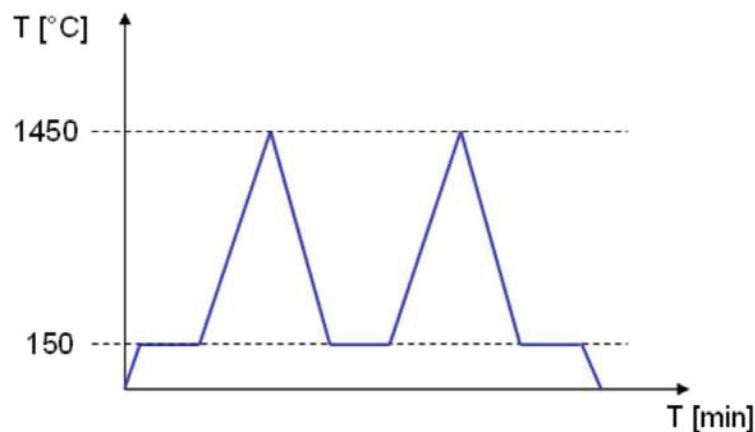
Figure 5.6: Time – temperature characteristics.

L. Hädicke

The heating and cooling rate was 20K/min. Additionally to this time temperature program, some samples were annealed by heating to a certain temperature and then quenched with 50 K/min to conserve the thermodynamic state and consequently the structure and phase composition of a given annealing temperature T_a.

4.2.5 Elastic recoil detection analysis (ERDA)

Elastic recoil detection analysis is a nuclear technique which allows obtaining elemental concentration depth profiles of thin films. An energetic ion beam is directed at the sample to be depth profiled and is stimulating an elastic nuclear interaction with the atoms of the sample. The facility used in this thesis is the tandem accelerator of the Ångström laboratory of the University of Uppsala, Sweden, shown in Figure 5.7. The accelerated Iodine-ions have an average energy of about 35MeV. These ions react with the surface of the sample in an area of 4*4 mm. The recoiled atoms of the film are detected with a time of flight detector. The advantage of this analysis is the high accuracy of the method for lighter elements than the accelerated I-ions. The drawback is that the heavier atoms like Zr and Y in the film were not distinguishable. ERDA was used to measure the exact ratio of O to N in the oxinitride system [66].
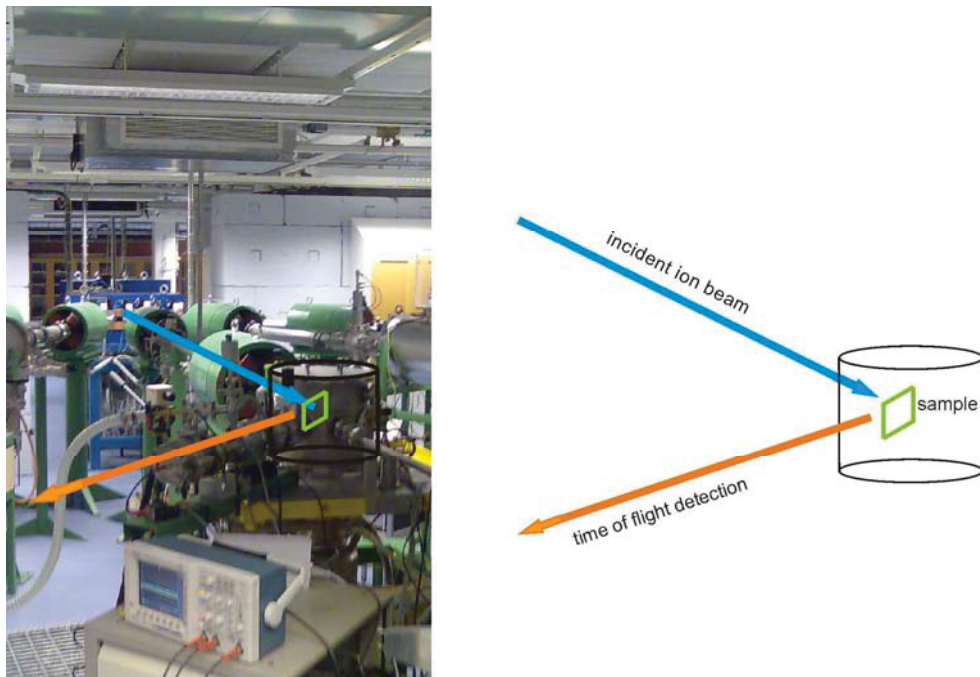
Figure 5.7: Tandem accelerator of the Ångström laboratory of the University of Uppsala, Sweden.

L. Hädicke

4.2.6   Nanoindentation

For the mechanical characterization of nanostructured materials the so called nanoindentation is a suitable method. It permits the determination of hardness and elastic modulus (Young's modulus). In a nanoindentation measurement, an indenter is pressed into the surface of a material while the applied force and the displacement of the indenter are recorded. From the load-displacement curve (Figure 5.8) the hardness and the elastic modulus are determined after the Oliver-Pharr method [67] using a CISRO nanoindenter
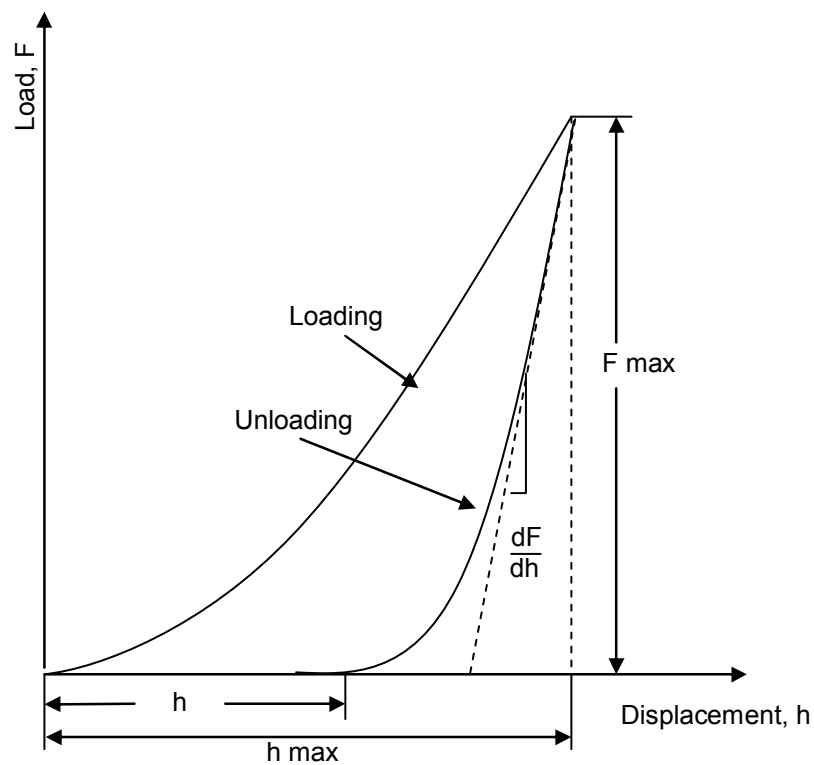
Figure 5.8: Nanoindentation load-displacement-curve.

L. Hädicke

5   Results and discussion

5.1   Zr-Al-Y-N

5.1.1   Elemental composition

The elemental composition of the investigated films derived from EDX and ERDA measurements is presented in Table 6.1. EDX has its strengths in the resolution of heavy elements like Zr and Y but not for light elements like N and O. ERDA has its advantages, because its using I-ions, for lighter elements like N and O and is not able to resolve heavier elements than iodine. Although it is not able to resolve heavier elements the quantity of the result is better than from EDX. Consequently, the sum of all heavier elements Zr+Y measured from ERDA were separated according to the ratio Zr/Y which was measured with EDX.

Table 6.1: Chemical composition measured with EDX and ERDA.

Sample designated to the Y content	Zr [at%]	Al [at%]	Y [at%]	N [at%]	O [at%]
0Y	27.25	17.70	0.00	54.35	0
0.002Y	26.02	17.38	0.002	56.07	2.60
1.2Y	27.57	18.04	1.26	53.22	2.80
3.4Y	24.39	16.77	3.45	54.63	0
15.9Y	16.34	12.70	15.96	47.40	6.20

For the three films, with the Y contents of 0.002, 1.26 and 15.96 at %Y an oxygen content is given, as these three are additionally measured with ERDA. ERDA measurements give a chemical composition versus film thickness. The heavier elements are displayed as a sum which is shown in Figure 6.1 where the Zr and Y content are displayed together. All films investigated contained traces of Ar, C and H < 1 at%.

L. Hädicke
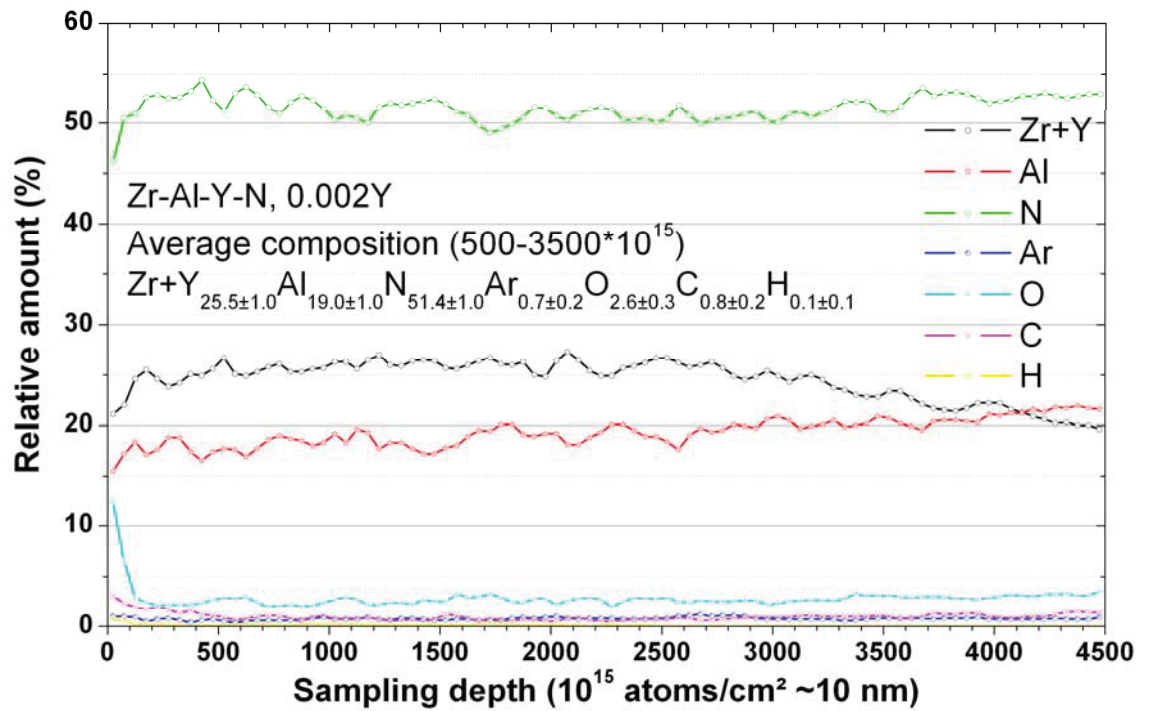
Figure 6.1: Elemental depth profile of 0.002Y from ERDA
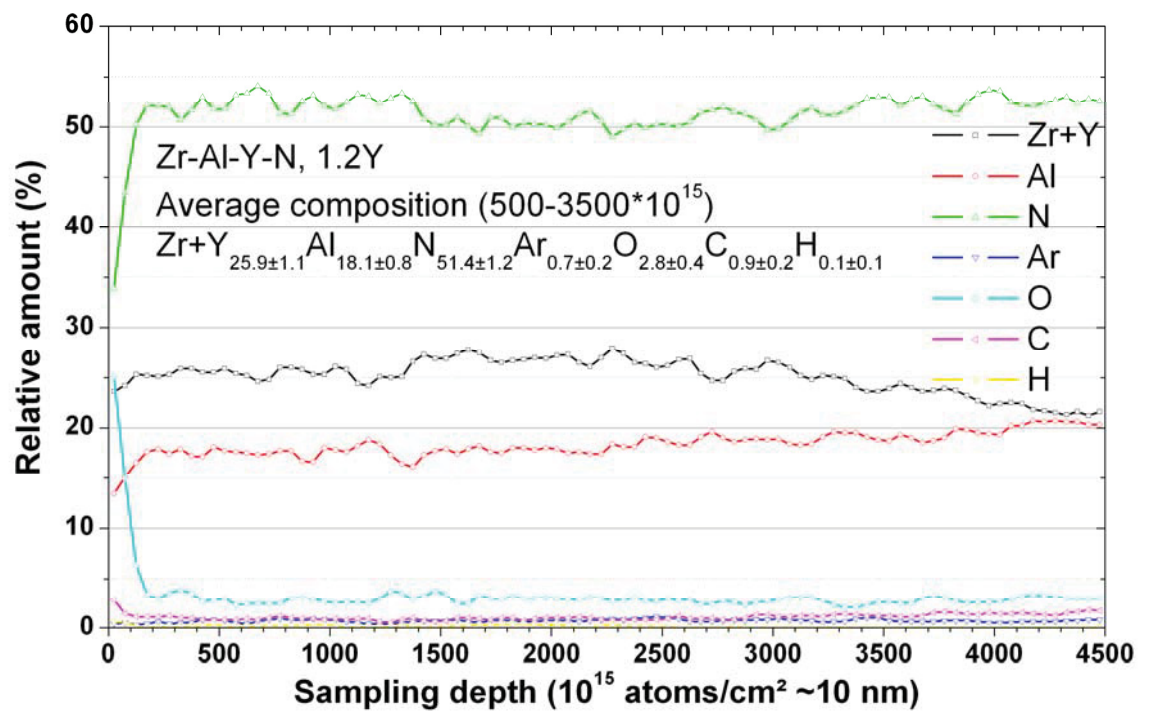
Figure 6.2: Elemental depth profile of 1.2Y from ERDA

L. Hädicke
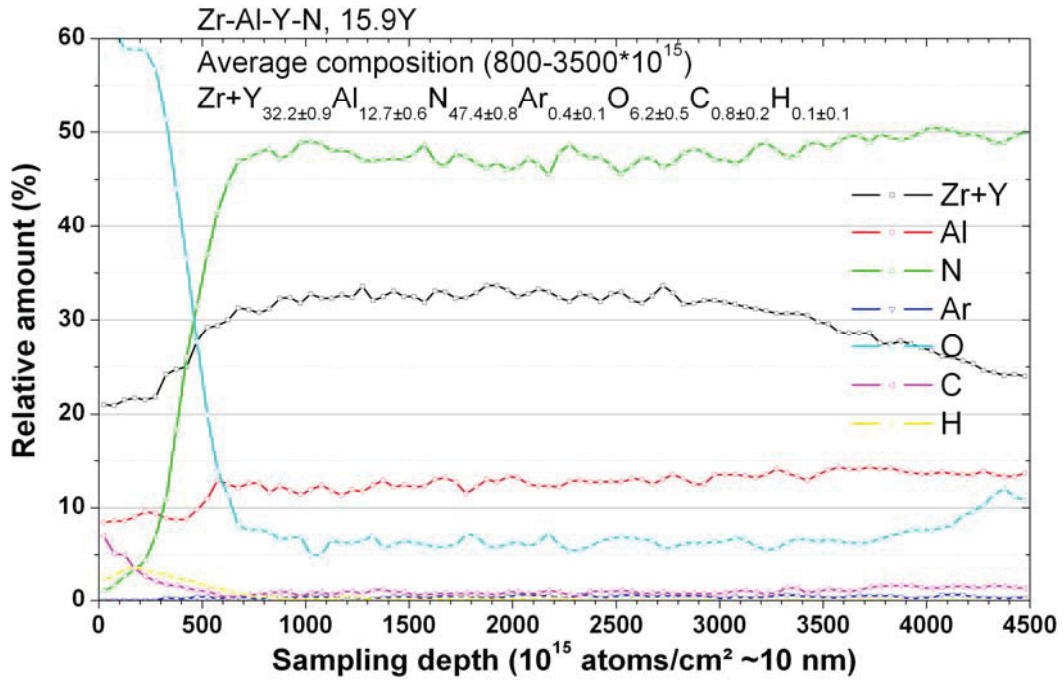
Figure 6.3: elemental depth profile of 15.9%Y from ERDA

The ERDA depth profile of 15.9Y shows a higher O content than the other investigated coatings because of the use of Y platelets (see chapter 5) which were partially oxidized and served as O_2 source during deposition. A vacuum pump failure occurred at the end of the deposition of the 15.9Y sample which is the reason for the high O_2 content at the surface of the film. The oxidized surface layer which is visible in Figure 6.3 had no influence on further investigations because the TEM samples were taken close to the interface.

5.1.2 Phase analysis

In addition to the optical HRTEM mode the diffraction mode was used to determine the phase composition of the samples in the as-deposited state. Therefore the software PocessDiffraction [68] was used. At first the cameralength was calculated by analysing the diffraction pattern of sapphire single crystal at the substrate-coating interface [69].This cameralength was then used for the SAEDs taken from the film.

An example for the cameralength calculation is shown in Figure 6.4. Here the single crystal reflections of the (0001) sapphire orientation with the typically six fold symmetry are shown together with the typical diffraction rings of the randomly orientated coating crystallites of the 3.4Y sample at the substrate-coating interface.
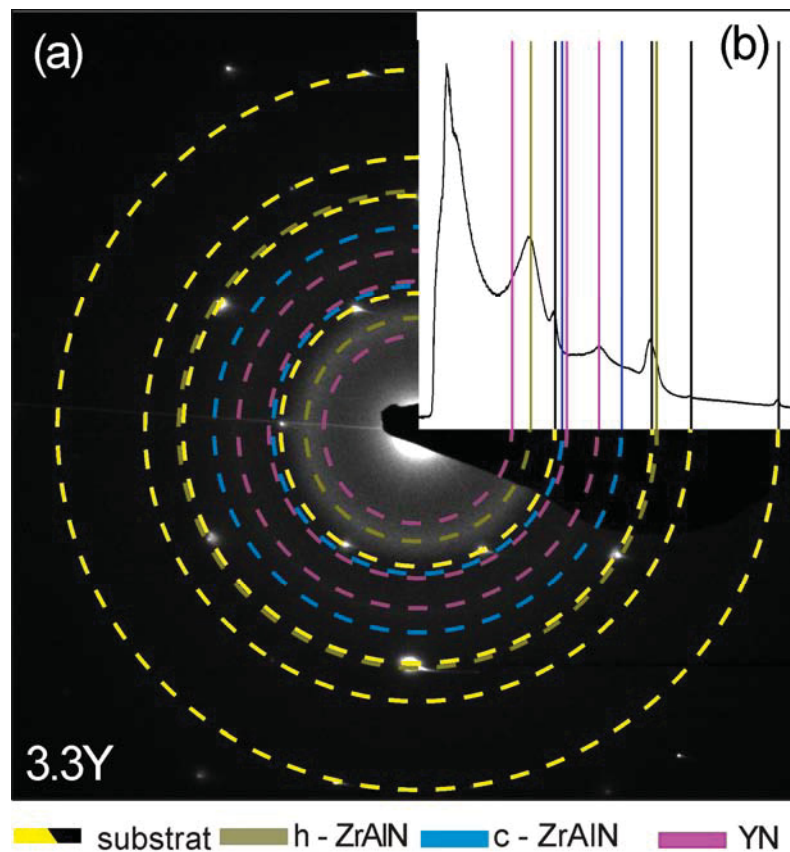
Figure 6.4: (a) 3.4Y SAED pattern (b) with ProcessDiffraction intensity distribution taken at the coating substrate interface of the sample.

Figure 6.4 (b) shows the intensity integral versus the radius of the SAED as calculated by the ProcessDiffraction program. From the reflexes of the sapphire substrate and its known symmetry the cameralength was calculated.

All samples show polycrystalline rings at the interface. Whereas the bright dots indicate the sapphire single crystal, the diffuse concentric rings indicate other existing phases. The identified phases are fcc-YN, solid solution c-Zr(Al)N, and hexagonal solid solution ZrAlN. These phases have randomly orientated crystallites as visible by the diffuse rings which show the same brightness along the circumference.

L. Hädicke

Figure 6.5 (b) is the SAED taken from the film bulk and shows dots along a concentric ring and some diffuse brightness along the same rings.
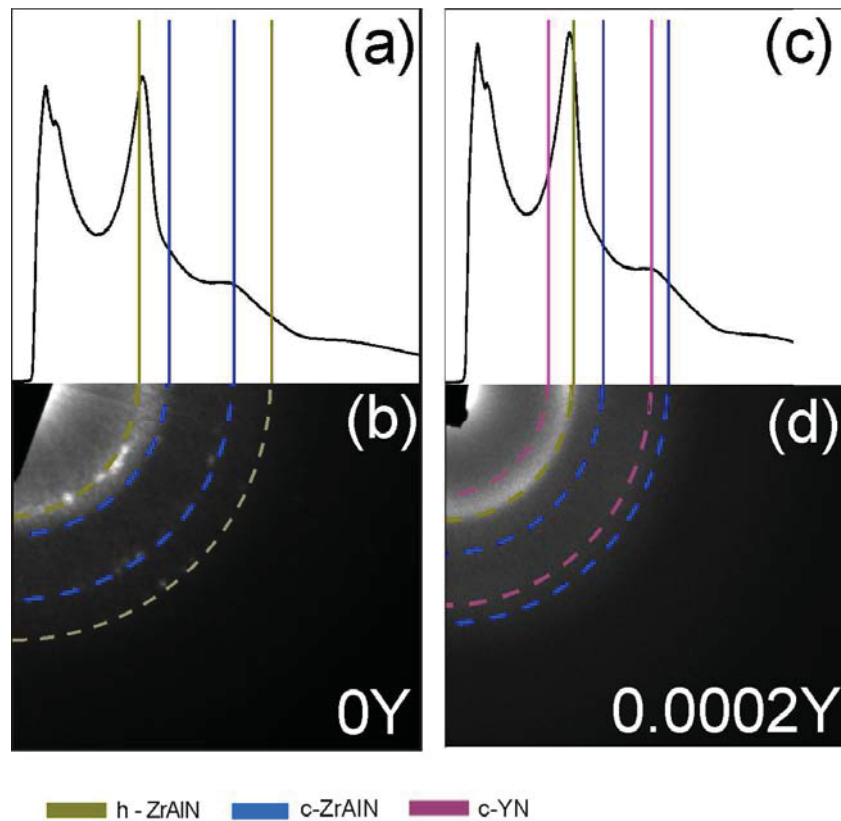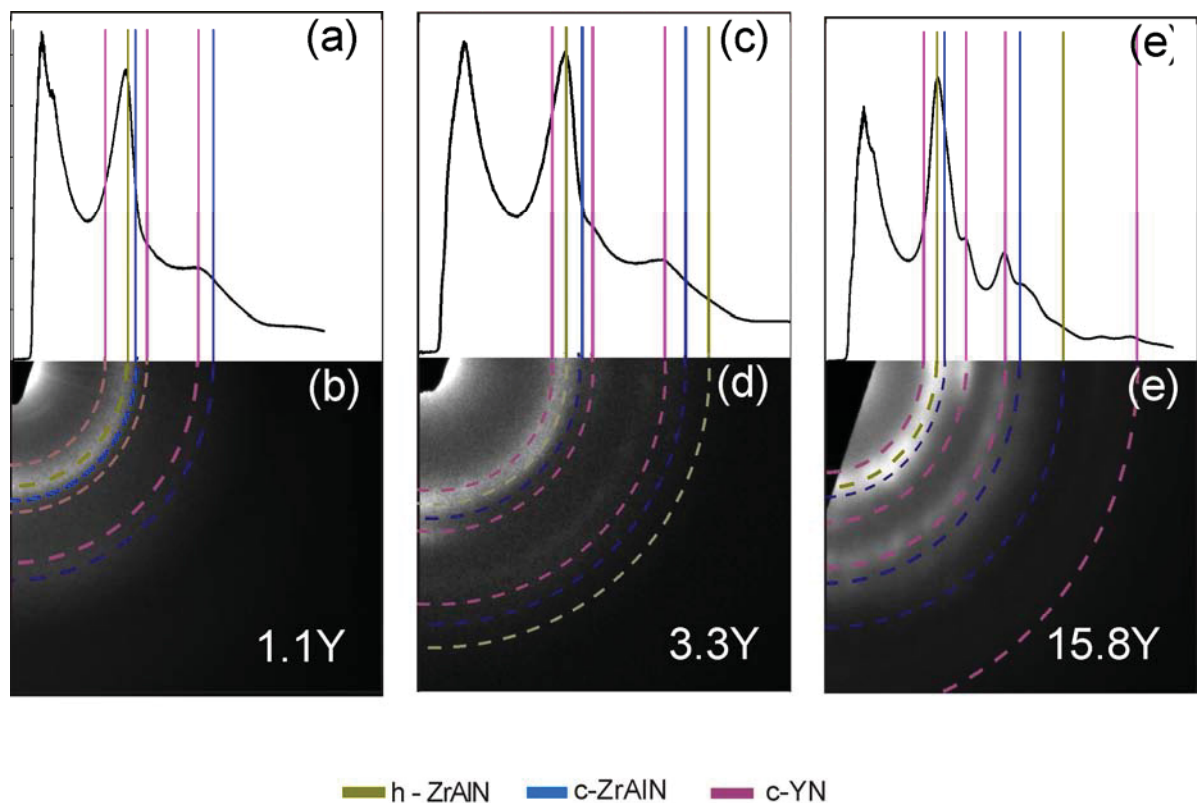

Figure 6.5: (a) Intensity distribution of 0Y with (b) associated SAED. (c) Intensity distribution of 0.002Y with (d) associated SAED

Figure 6.5 (b) is the SAED taken from the film bulk and shows dots along a concentric ring and some diffuse brightness along the same rings. The brightness decreases with the radius because of the background radiation. The rings and their radius are indicating a lattice parameter which again stands for a phase present in this sample. In Figure 6.5 (a) the density integral versus the radius is displayed and helps indicating the radius of the diffuse rings. Here we found hexagonal (h, B4, wurtzite) ZrAlN and c-ZrAlN. The hexagonal phase has lattice parameters of c=5.23 Å and a=3.16 Å and show random oriented crystallites. A few larger grains are visible through the dots in the diffraction ring.

The cubic ZrAlN phase matches a lattice parameter a of 4.50 Å and is a solid solution of the cubic ZrN phase alloyed with Al. According to Vegard's law the cubic ZrAlN phase with a a= 4.50 Å dissolves an amount of about 14.7 at% of Al. This fits well to the 17.7 at% found for this coating in the elemental analysis.

L. Hädicke

Figure 6.5 (d) displays diffuse concentric rings without dots along the circumference. In Figure 6.5 (c) the density distribution shows the same phases like the 0Y film with the same lattice parameters and additionally the cubic YN phase. This phase has a lattice parameter of 4.89 Å.

In Figure 4.6 the SAEDs and their corresponding density integral are displayed. The phases remain the same for all samples in Figure 6.6. The visible difference between these three is that the rings get less diffuse with increasing Y content. Consequently the corresponding density-integral distributions show more clearly where the ring's radii are located, corresponding to a higher crystallinity with higher Y content.

Figure 6.6: (a) Intensity distribution of 1.1Y with (b) associated SAED. (c) Intensity distribution of 3.3Y with (d) associated SAED. (e) Intensity distribution of 15.8Y with (f) associated SAED

The XRD measurements presented in Figure 6.7 of powdered sample-materials in the as-dep. state correspond well to the analysis of the SAED patterns. The Y-free ZrAlN film has a XRD-pattern of an ordered crystalline structure, with clear reflexes of h-ZrAlN and c-ZrAlN as observed in the SAED analysis. The phases indicated in the XRD are the same like in the SAEDs.

L. Hädicke

With the addition of Y the peak reflexes become featureless and with 1.26 at% Y only broad reflexes are observable. This may be a result of reduced diffusion during film growth due to the addition of the "large" element Y and a consequently reduced crystallite size in the film. Whereas the intensity in XRD depends on the grain size in the SAED the more fraction of amorphous phase the less intensity and so the less contrast.
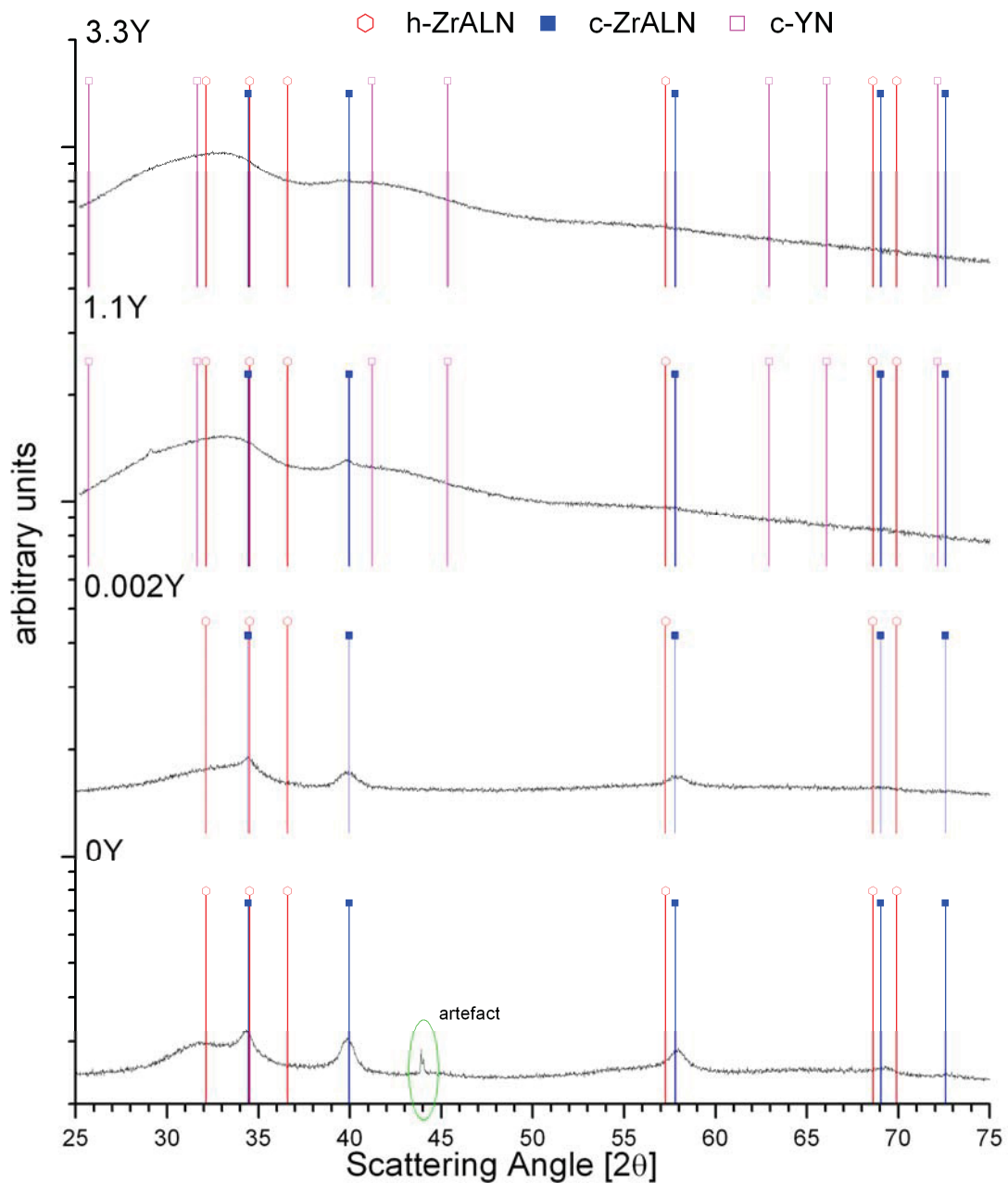

Figure 6.7: XRD of Zr-Al-Y-N 0Y, 0.002Y, 1.2Y and 3.4 Y in the as-deposited state.

L. Hädicke

5.1.3 Structure and morphology

Fracture-cross-section SEM images of the samples were made to determine film-thickness and morphology. The films were deposited on silicon for better conductivity.
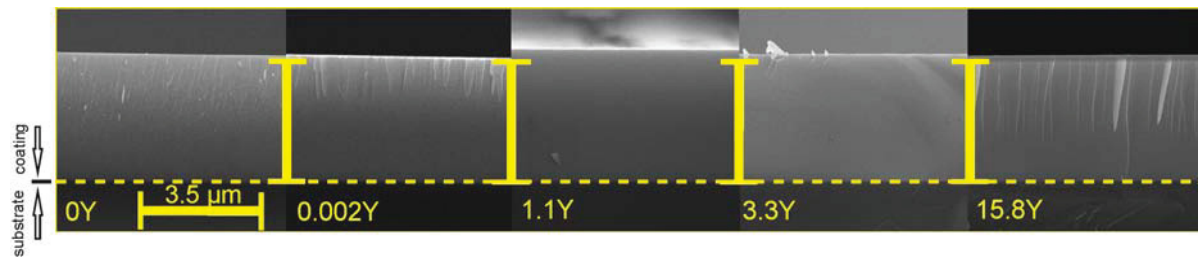
Figure 6.8:Cross section SEM images of Zr-Al-Y-N films with 0, 0.002, 1.2, and 15.8at% Y

All cross section images shown in Figure 6.8 are taken at the same magnification and have therefore the same scale. A thickness of 3.5μm was achieved for all samples. The SEM investigation of the cross sections of our films reveals dense, but otherwise feature-less cross sections, typical for nanostructured films [31].

The TEM images show a structure with nm sized crystallites and a thin amorphous layer at the interface (Figure 6.9).
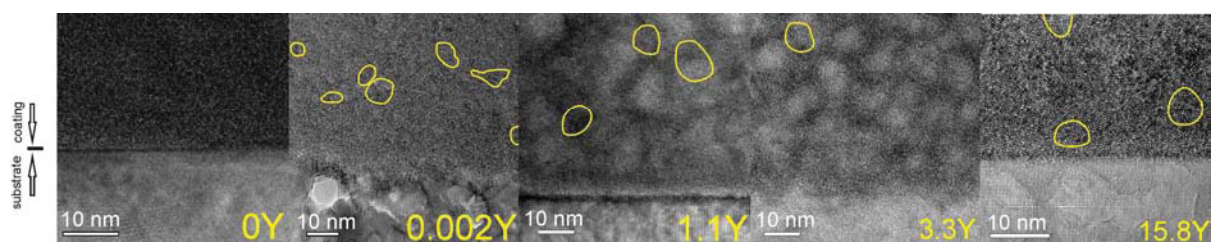
Figure 4.9: Cross section TEM image from interface of the Zr-Al-Y-N films with 0, 0.002, 1.2, and 15.8at% Y

In the bulk of the ZrAlN film (Figure 6.9) the morphology shows crystalline areas. Clear lattice places are visible which are surrounded by a boundary phase with a low short range order (amorphous). The latter has high electron (TEM, SAED) and X-ray (XRD) transparency and cannot be resolved by these methods. From Figure 6.10 an average

L. Hädicke

grainsize of 11 nm was determined for the 0Y film (Figure 6.10 (a)) and 10 nm for the 0.002Y film, visible in Figure 6.10 (b).
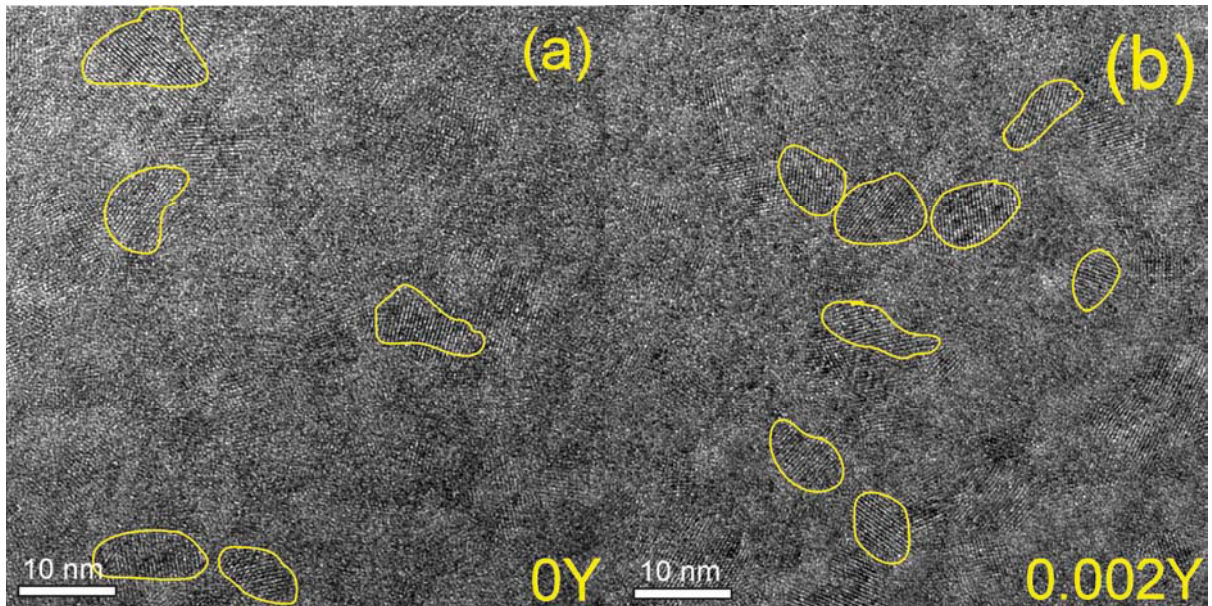
Figure 6.10: HR-XTEM image of (a) $Zr_{0.82}Al_{18}N$ and (b) $(Zr_{0.83}Al_{17})_{0.998}Y_{0.002}N$ films

The $(Zr_{0.83}Al_{0.17})_{0.998}Y_{0.002}N$ coating (Figure 6.10 (b) containing only 0.002 at% Y has a similar structure than the 0 at% Y film (Figure 6.10(a)) as it can be expected from the low Y content. Again the crystalline areas are embedded in a low short-range order phase.
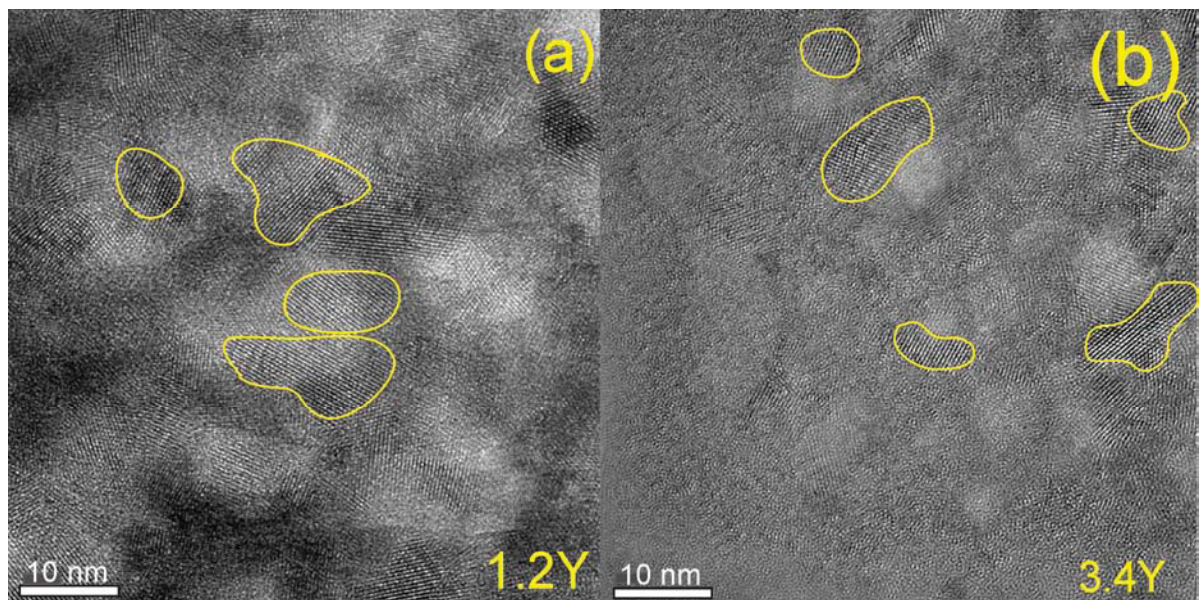
Figure 6.11: XTEM image of (a) $(Zr_{0.82}Al_{18})_{0.988}Y_{0.012}N$ and (b) $(Zr_{0.83}Al_{17})_{0.966}Y_{0.034}N$ films

With increasing Y content the grainsize increases reaching a maximum among the nitride films of 15 nm at an Yttrium content of 1.16 at% Y (Figure 66.11(a)). Also the amorphous grainboundary phase decreased. At an Y content of 3.4 at% Y (Figure 6.11(b)) an average

L. Hädicke

grainsize of 9 nm is observable. The maximum content of 15.9% Y shows only traces of amorphous boundary phase and the grainsize has decreased to ~7 nm, see Figure 6.12.

In the displayed HRTEM images the most apparent grains are encircled by yellow lines.
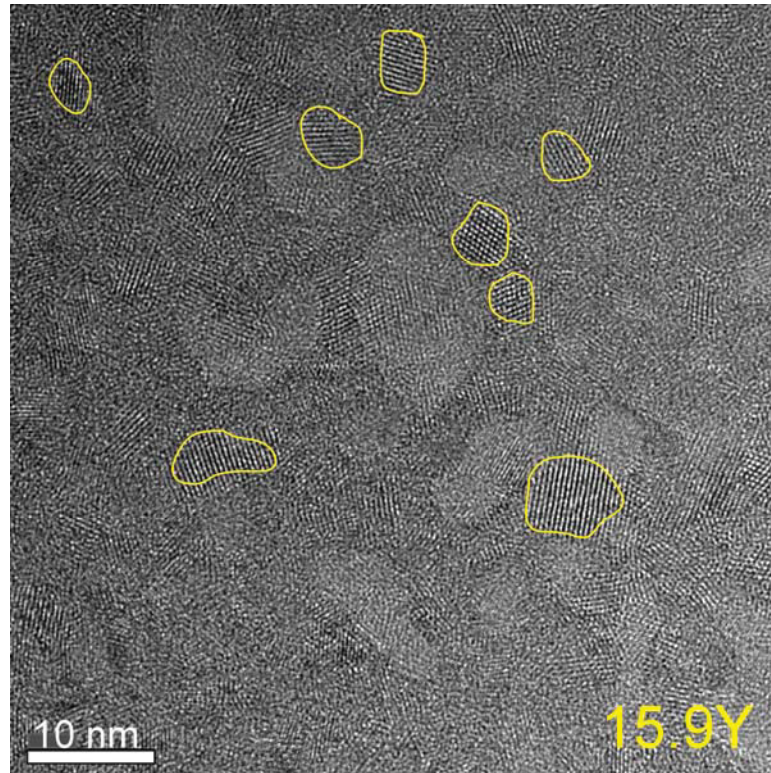
Figure 6.12: HR-XTEM image of $(Zr_{0.87}Al_{13})_{0.841}Y_{0.159}N$

5.1.4 Mechanical properties

The hardness (H) and the Young's modulus (E) of the films were measured on samples deposited on sapphire. Figure (6.13) shows a hardness value of 16.07 GPa for the Y free coating. With increasing Y-content the hardness decreases rapidly till it reaches a plateau of 15.5 GPa at about 3.4 at% of Y where the hardness does not change with a further increase in Y-content.

L. Hädicke
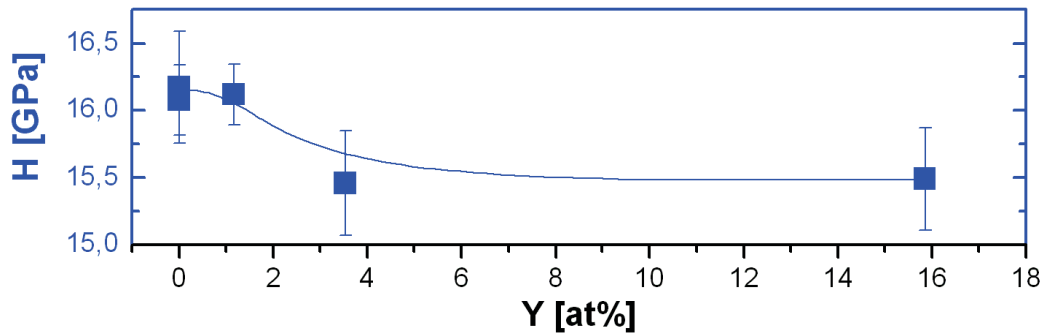
Figure 6.13: Hardness versus Y-content for the Zr-Al-Y-N films.

The effect of solid solution, results in an increase of the Young's modulus from 194.43 to 201.44 GPa with the addition of 0.002 at% Y. The Young's modulus has a maximum of 208 GPa at an Y-content of 1.26 at% Y. At a higher Y-content the Young's modulus decreases to a level of 203.67 GPa and reaches 201.34 GPa at an Y-content of 15.96 at% Y. This decrease in Young's modulus can be explained in the formation of the relatively soft c-YN phase. Y. Cherchab et al. [80] gave an average bulk modulus of 166 GPa which explains the decrease with increasing Y-content.
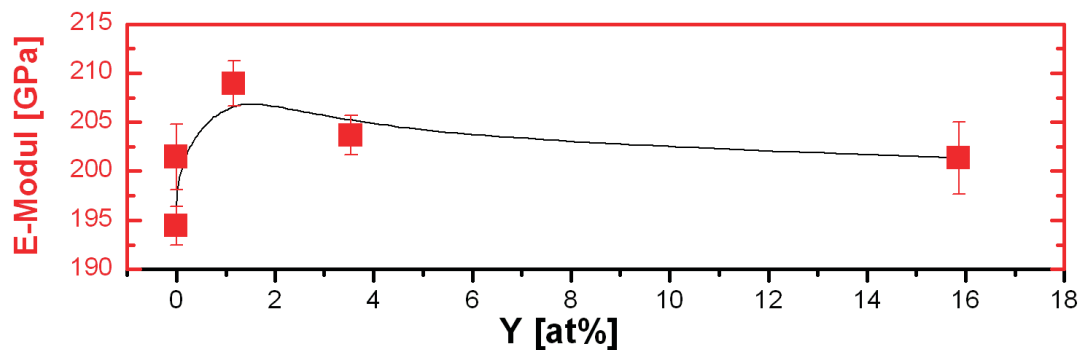
Figure 6.14: Young's modulus versus Y-content.

5.1.5   Thermal stability

In this work the thermal stability was investigated by STA to compare the structural evolution of the films with different Y contents. Figure 6.15 shows DSC traces measured of our coatings up to a temperature of 1450°C. Several exothermal and one endothermal reaction can be distinguished for all investigated films. A small exothermal heatflow starting at ~500°C (the deposition temperature) is a consequence of the recovery and recrystallization process and decreases with increasing Y-content. The first exothermal reaction (Ex 1) which is situated at 1010°C for the 0 at% Y film, shifts to higher temperatures with higher Y-

L. Hädicke

content while the second exothermal reaction (Ex 2), which has sinusoidal shape, moves to lower temperatures. Consequently, for the coating containing 3.4 at% Y Ex 1 is at 1045°C and Ex 2 at 1180°C. The higher the Y-content the more exothermal are the reactions Ex 1 and Ex 2. The endothermal reaction En 1 is at 1310°C for the Y-free coating and its peak temperature decreases for higher Y- contents, e.g. 1280°C for 1.2 at% Y. In the graph of the 0 at% Y film there is a second endothermal reaction (En 2) at about 1360°C. This reaction is not detectable at higher Y contents.
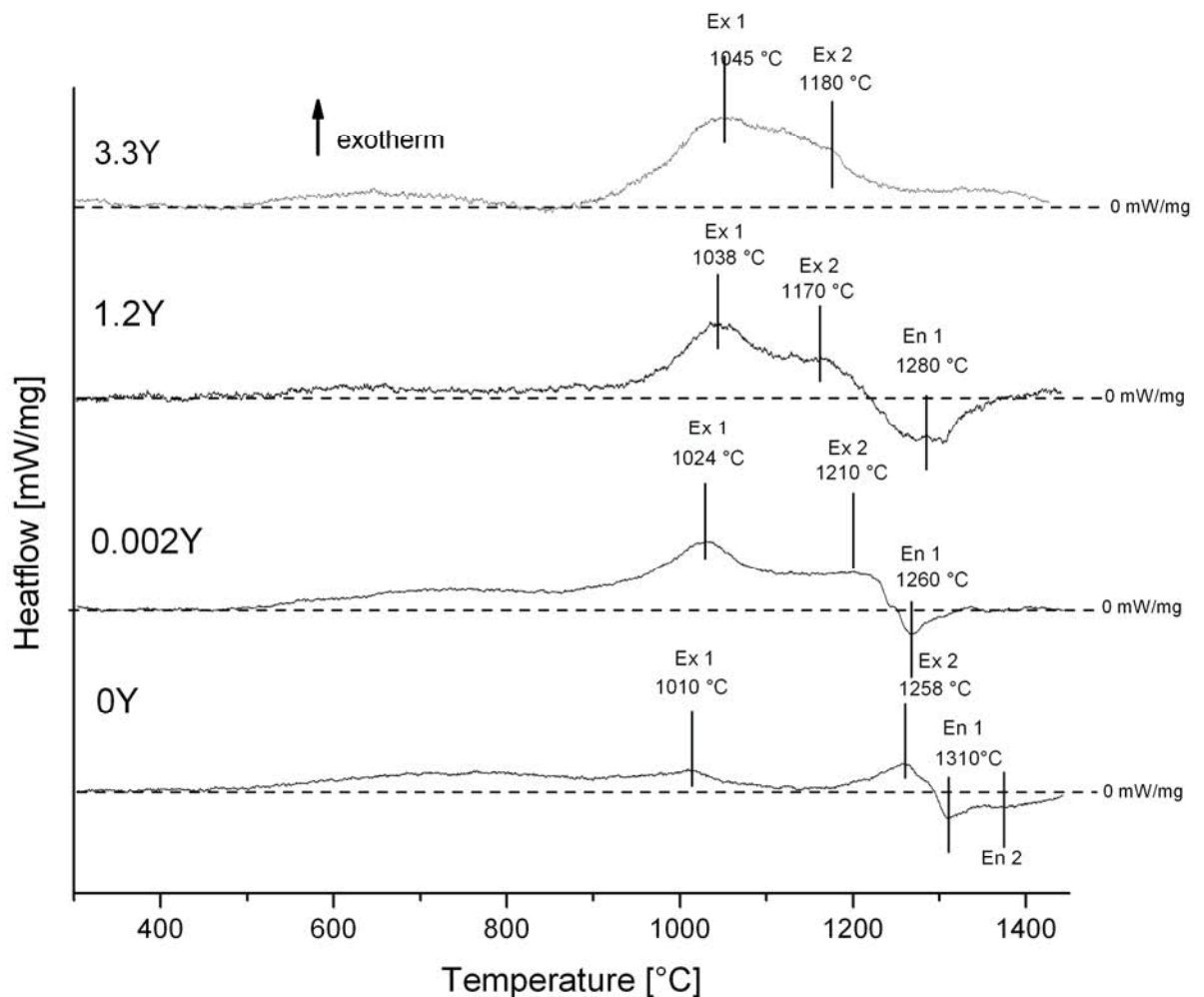
Figure 6.15: The heatflow versus temperature of the Zr-Al-Y-N coatings during DSC to 1450°C.

Figure 6.15, which show the TGA measurements during DSC. All data are buoyancy corrected so the mass loss is also quantitatively correct. At an onset temperature of ~200°C up to ~1200°C a mass loss of 0.12% is measured for the 0 and 0.002 at% Y films, 0.84% and 0.39% for the 1.2 and 3.3at% Y, respectively. A strong mass loss starts at the temperature where the reaction Ex 2 (Figure 6.15) has its maximum. The mass loss for the films was

L. Hädicke

determined from the maximum temperature of the reaction Ex 2 till the end of the measurement at 1450°C. The highest mass loss of 5.5% occurs in the 3.5Y film and the lowest mass loss of 3.7% in the 1.2Y film. Another support of the DSC data is that the increasing mass loss around the deposition temperature causes an endothermal heatflow which is visible as a decrease of the exothermal heatflow of the recovery and recrystallization reaction.
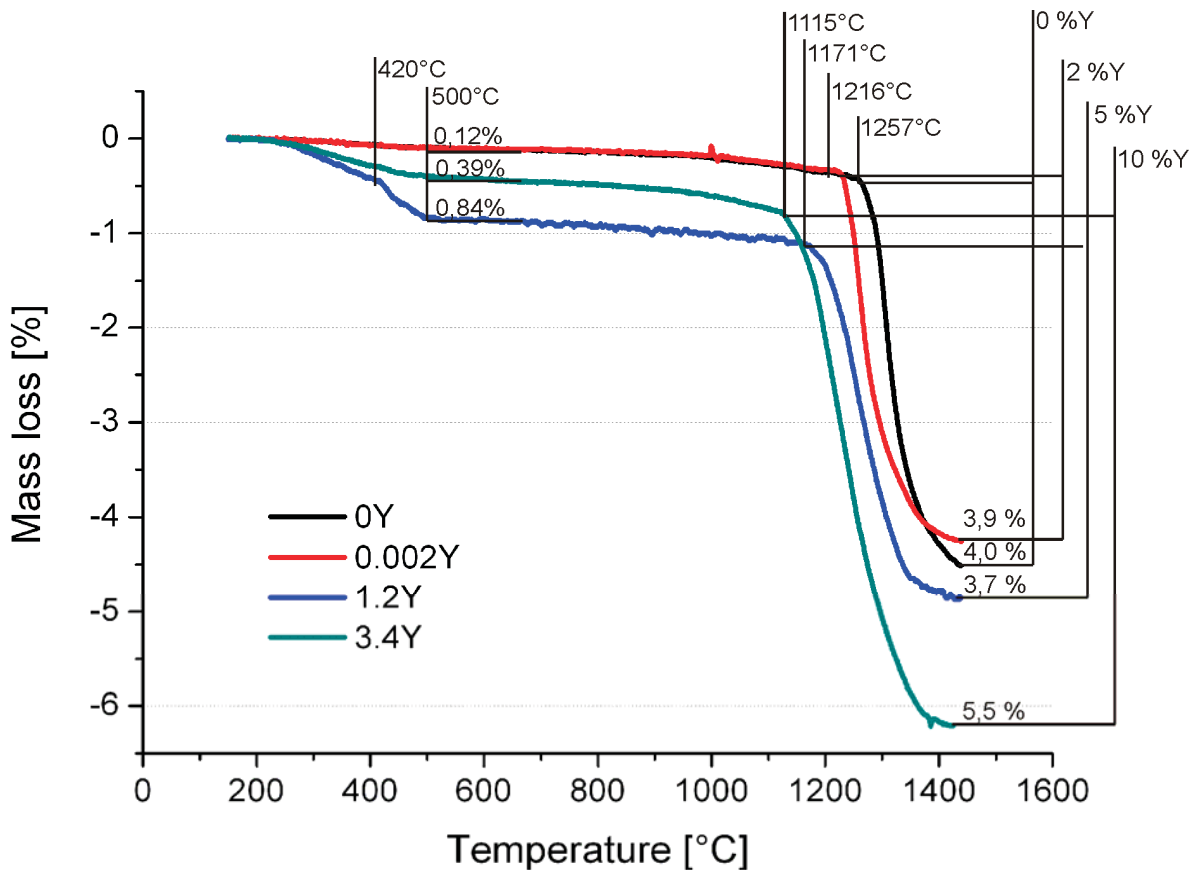

Figure 6.16:Mass loss of the Zr-Al-Y-N films during DSC to 1450°C.

Additionally, mass spectrometer scans were executed during DSC. The spectrometer was set to detect the gases N_2 and O_2. In Figure 6.17 the ion current versus temperature is showing qualitatively the detected gases of the 1.2Y film. Up to 500°C, the deposition-temperature, O_2 and N_2 are detected corresponding to the mass loss found in the TGA. From about 800°C strongly increasing amounts of O_2 and N_2 are detected. In the temperature range between 800 – 1450°C we detect a higher increase in N_2 compared to O_2 so the mass loss shown in Figure 6.17 can be attributed to the release of N_2 from the samples.
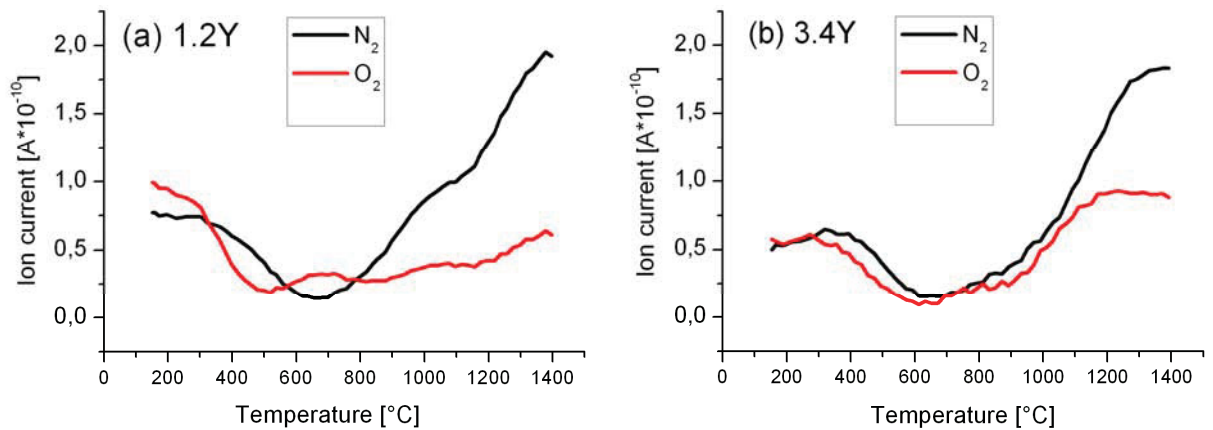
L. Hädicke

Figure 6.17: Mass spectroscopy of the 1.2Y film (a) and the of the 3.4Y film (b)

The characteristics of the mass spectroscopy of the 3.4Y film (Figure 6.17(b)) shows similarities to the 1.2Y film. At 500°C the mass loss stops and starts again at a higher rate at about 800°C with the stronger signal detected for N_2.

5.1.6 Phase stability

All samples where investigated using in-situ XRD. The patterns in Figure 6.18 give a characteristic overview of all compositions and measured temperatures in the scattering angle 2Θ from 30° to 37°. In between this angle the reflexes of c-ZrN [111], h-AlN [002] as well as h-ZrAlN [100] and [101] indicate the formation of these phases at a certain temperature. The patterns in Figure 6.18 are not temperature corrected so the peaks are temperature shifted. Caused through the higher solubility for other elements the peaks are also shifted. From the as deposited state up to 900°C no reaction is detectable indicating that the exothermal heatflow till 900°C is due to recovery. The measurement at 1100°C for the 0%Y film was not executed. Above 900°C reflexes for c-ZrN, h-ZrAlN and h-AlN can be detected corresponding to reaction Ex 1 in the DSC measurements.
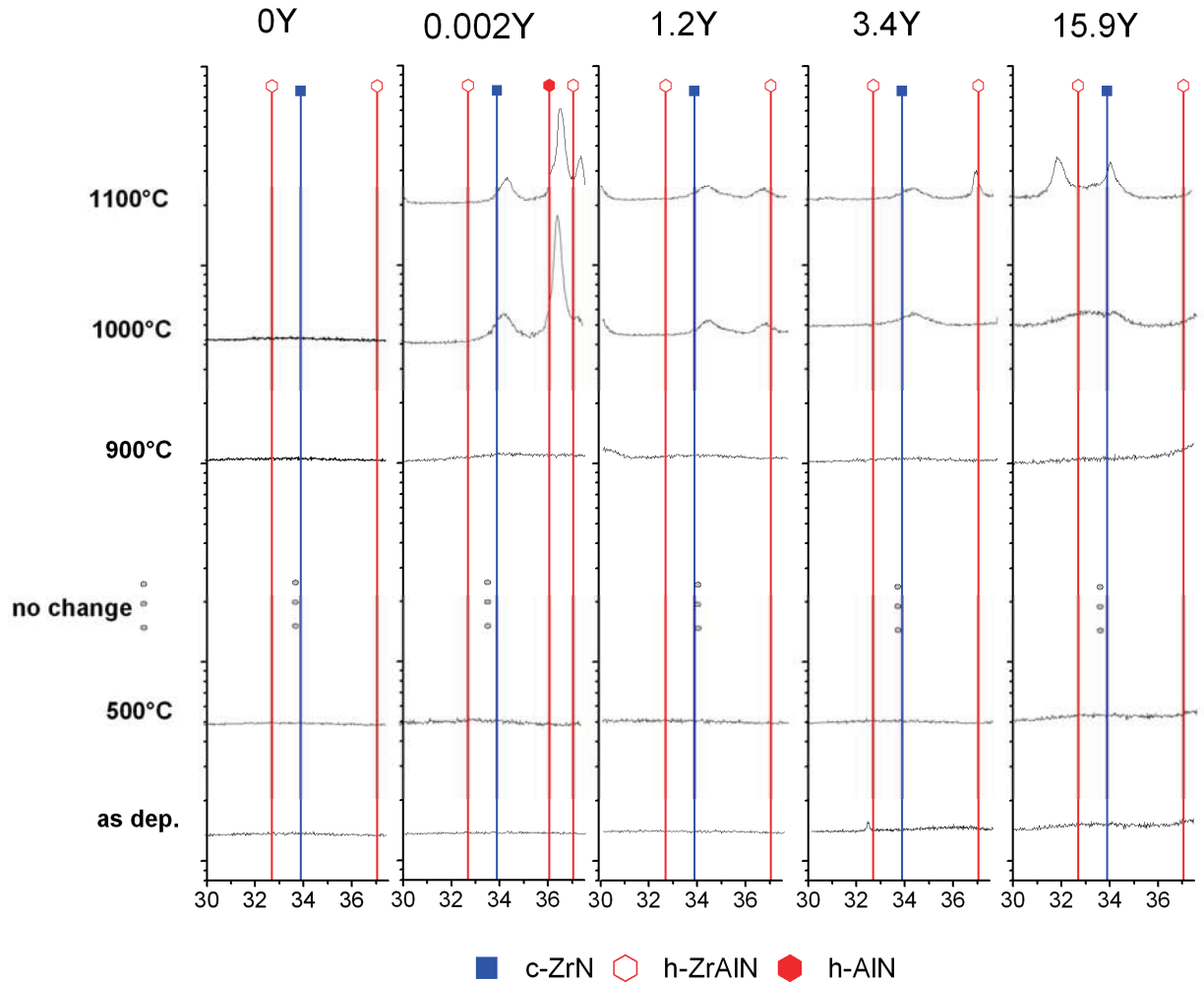
L. Hädicke

Figure 6.18: In-situ XRD patterns of the Zr-AlY-N films at several temperatures.

For an investigation of the formation of phases during the DSC measurement the samples were heated with a rate of 20K/min to temperatures above the peak temperature of Ex 1, Ex 2, En 1 and En 2 and subsequently quenched with 50K/min to room temperature (RT). Thus, the phase configuration after a DSC reaction can be conserved and analysed. This was done for the coatings containing 0 and 1.2 at% Y.

The 0Y film was annealed to 1115°C and 1286°C and then investigated with XRD at RT. These measurements are combined in Figure 6.19 with the RT-XRD of the as-deposited coating and the sample after the DSC cycle. With this comparison the first reaction (Ex 1) at 1010°C can be attributed to a recovery. The c-AlN phase found in SAED was not detected in RT-XRD and in the sample quenched at 1115°C. In the quenched sample at 1115°C the peaks of the c-ZrAlN and the h-ZrAlN are shifted to higher angles. The second reaction (Ex 2) at 1260°C is the decomposition of h-ZrAlN and c-ZrAlN to c-ZrN and h-AlN. After the

DSC cycle the measurement shows the phases detected after Ex 2 plus some oxidized Zr in the tetragonal configuration. The sharper peaks suggest a coarsened structure.
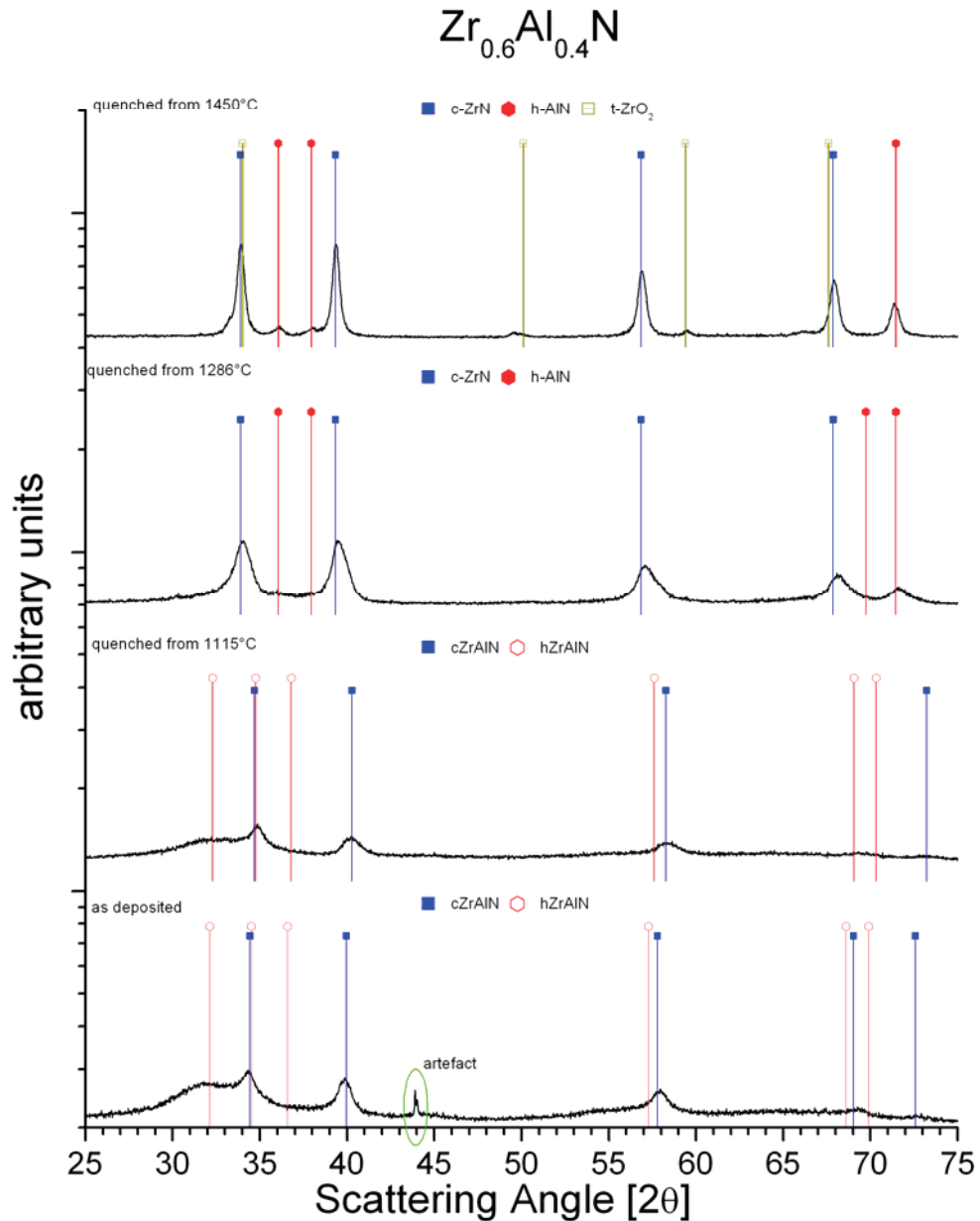

Figure 6.19: RT-XRD of 0Y in the as-deposited state, quenched from 1115°C, 1286°C and 1450°C.

The same procedure was applied on the 1.2Y film where additionally c-YN detected by SAED, should be present in the as deposited state, Figure 6.20. This coating's reaction at 1124°C is again dedicated to recovery processes as there is no change in phase composition and orientation detected. The decomposition of c-ZrAlN and h-ZrAlN to c-ZrN and h-AlN occurs at about 1220°C. After the DSC cycle to 1450°C the phases c-ZrN and h-AlN remain

L. Hädicke

but different oxides were formed than as compared to the 0%Y film. Here, the ZrO_2 is doped with Y and forms the YSZ and some m-ZrO_2. Also the Al reacts with O and forms corundum.
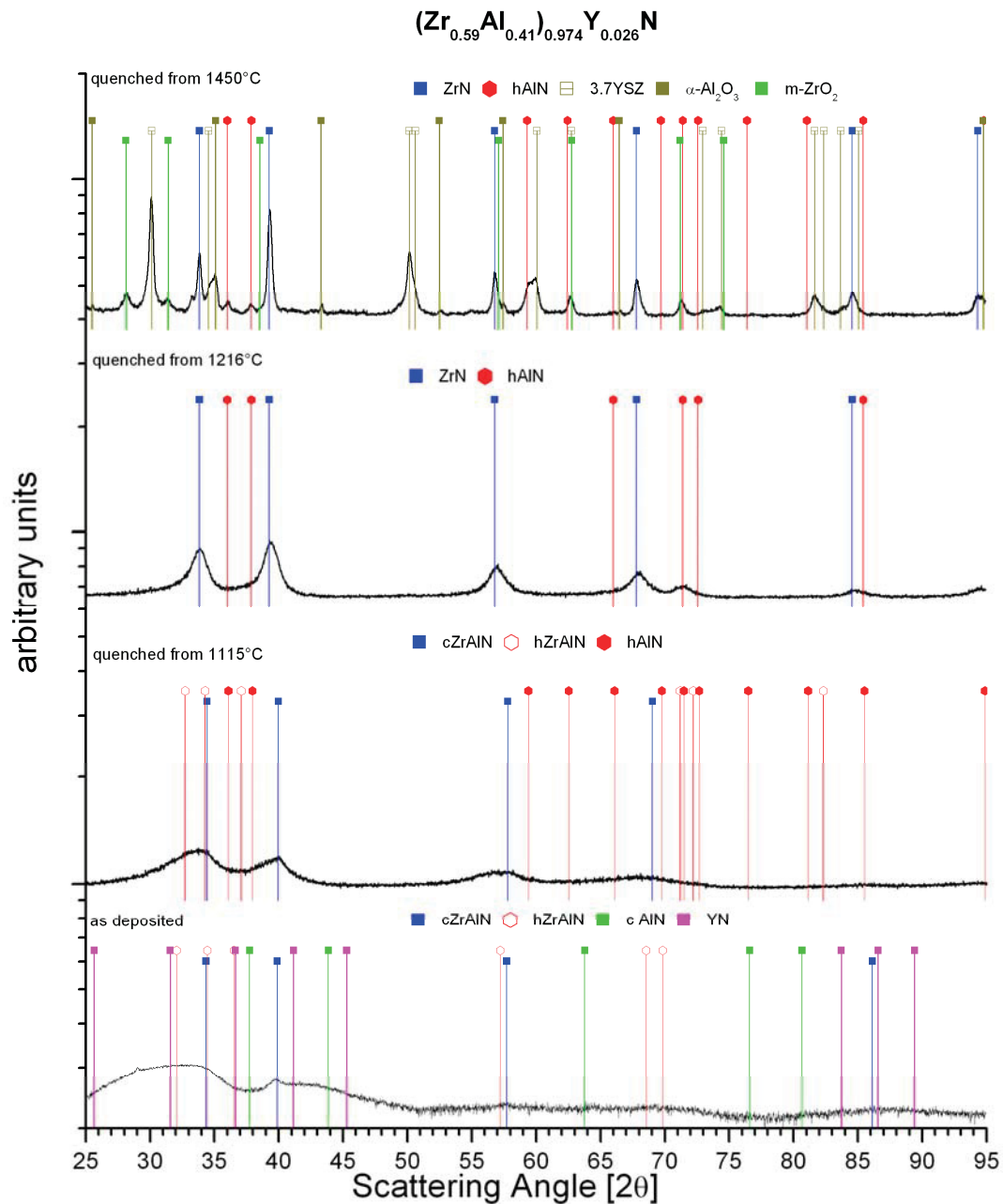

Figure 6.20: RT-XRD patterns for the 1.2Y film in the as-deposited state, quenched from 1115°C, 1286°C and 1450°C.

Although the measurements were conducted in inert atmosphere (He) the sample material formed oxides. This is due to the high affinity of Y, Zr and Al to oxygen and the high specific surface of the used powder.

L. Hädicke
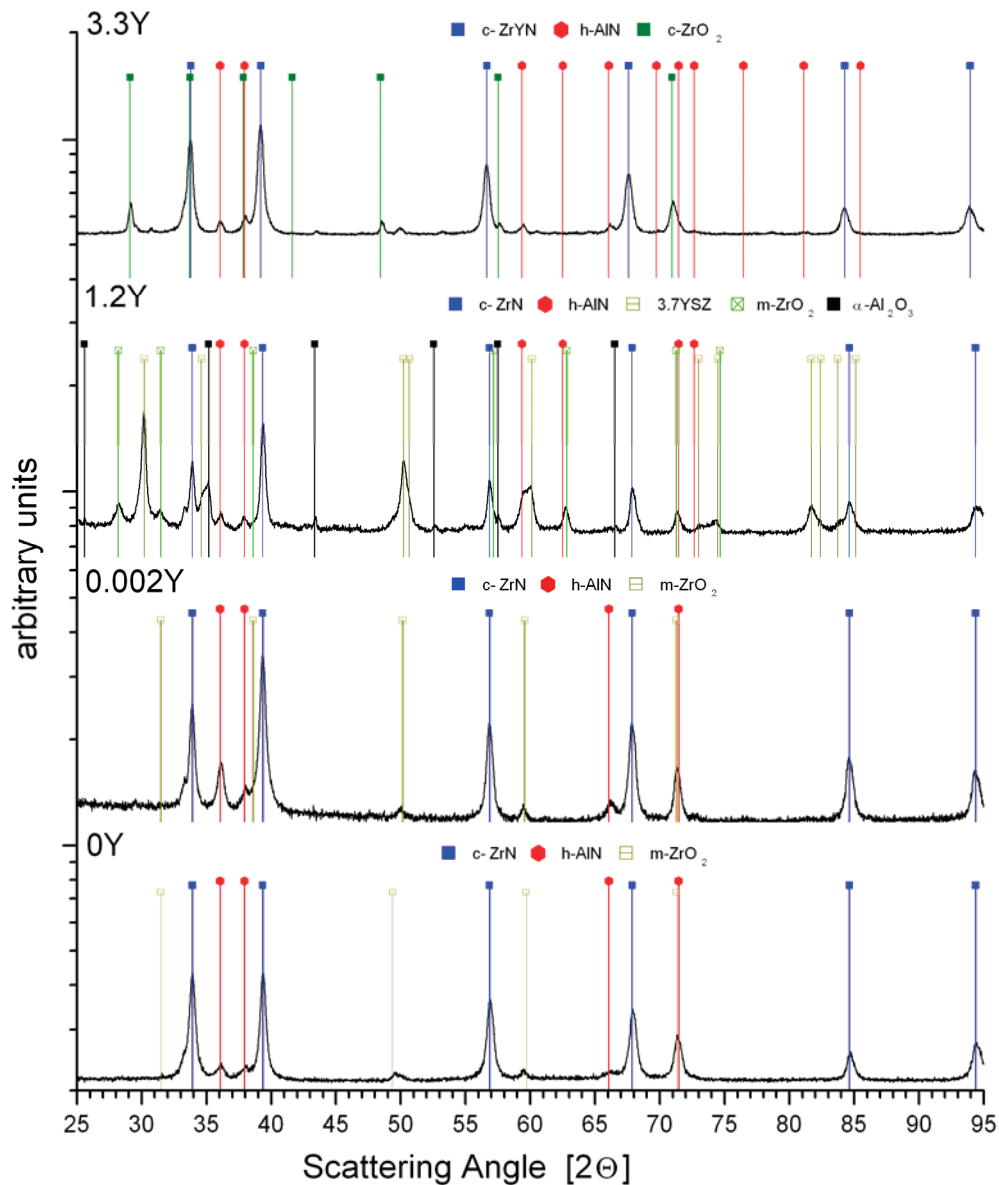
Figure 6.21: XRD patterns of Zr-Al-Y-N films with 0, 0.002Y 1.2Yand 3.4 at% Y measured at RT after the DSC –cycle to 1450°C.

In Figure 6.21 an overview of all samples after the DSC-cycle to 1450°C is given. No apparent difference is observed for the peak positions between the Y-free film and the coating containing 0.002 at% Y, due to the low amount of Y.

At an Y content of 1.2 at % the phases c-ZrN and h-AlN remain but instead of the m-ZrO$_2$ there the yttrium-stabilized tetragonal ZrO$_2$ and the monoclinic configuration of ZrO$_2$ are formed along with α-Al$_2$O$_3$.

With increasing Y content the h-AlN still remains but the c-ZrN peaks are shifted to lower angles. The fcc-ZrO$_2$ detected at the 3.3Y sample is found at lower angle than listed in the

L. Hädicke

database [70]. From this shift an increase in the lattice from 5.135 to 5.315Å is calculated, suggesting that Y is dissolved in the c-ZrO$_2$.

A plot of the transformation maxima against the Y content gives an overview of the phase evolution, see Figure 6.22. In this diagram the formation of oxides is not included.
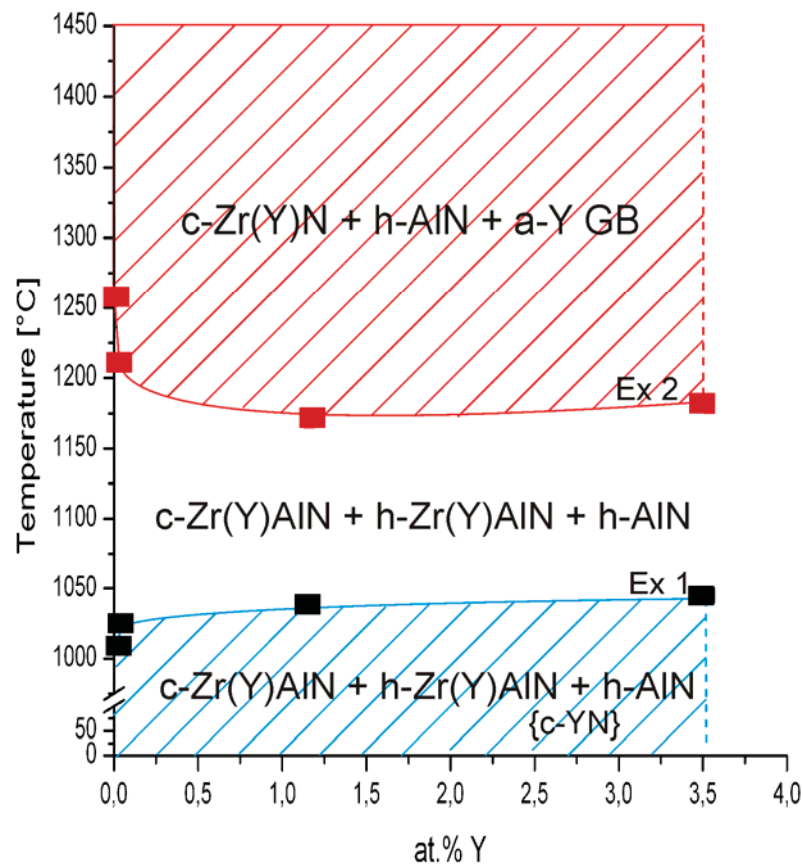

Figure 6.22: Phase stability range of Zr-Al-Y-N films as a function of the Y content.

As visible in Figure 6.22 Yttrium stabilises the Ex 1 reaction to higher temperatures. This reaction can be dedicated to a recovery and recrystallisation reaction because the phases c-YN can only be detected in the SAED but not in the as-deposited XRD results. Hence c-YN is shown in Figure 6.22 in brackets.

The Y-content also decreases the temperature of the c-ZrAlN + h-ZrAlN → c-ZrN + h-AlN decomposition from 1258°C to about 1180°C. Remarkable is that only the film with the highest overall Y content of 3.54 at% Y shows a peak-shift of the ZrN phase after the decomposition. Whereas the lower Y and hexagonal phase containing films show no shift after the decomposition. With increasing amount of Y the decomposition of the solid solution stabilizes to higher temperatures.

L. Hädicke

5.2 Zr-Al-Y-O-N

5.2.1 Elemental composition

To designate the films they are abbreviated by the Y content in the film, corresponding to the nitride films. The chemical composition of all oxinitride films was measured with ERDA to determine the exact O to N ratio. As described in the part chemical composition of chapter 6.1 the advantages of ERDA and EDX were balanced to calculate the elemental composition, Table 6.2.

Table 6.2: Chemical Composition measured with EDX and ERDA

Sample designated to the Y content	Zr [at%]	Al [at%]	Y [at%]	N [at%]	O [at%]
0Y	17.4	12.2	0	12.5	56.8
0.8Y	17.0	11.8	0.8	11.5	57.4
1.4Y	16.3	12.2	1.4	10.9	57.5
3Y	17.5	10.6	3.0	8.4	59.4
10.4Y	13.0	8.6	10.4	6.7	60.0

All samples have traces of Ar, C and H. The Argon is incorporated as it is used as working gas during deposition. C and H originate from contamination inside the decomposition chamber. These elements are found with a concentration below 1 at%. The used reactive gas was a mixture of 20% O_2 and 80% N_2 as described in chapter 2.1. The O/N ration of 0.25 in the gas changes into an O/N ratio of about 5 in the film. This can be explained through a higher chemical affinity of the sputtered species for O_2 than for N_2.

The chemical depth profile shows for coatings with 0 to 3 at % Y an increase of oxygen in the top 250 nm of the films (Figure 6.23). This is an oxide layer which grows after deposition. This trend is not observable for the coating containing 10.4 at% Y, see Figure 6.25.
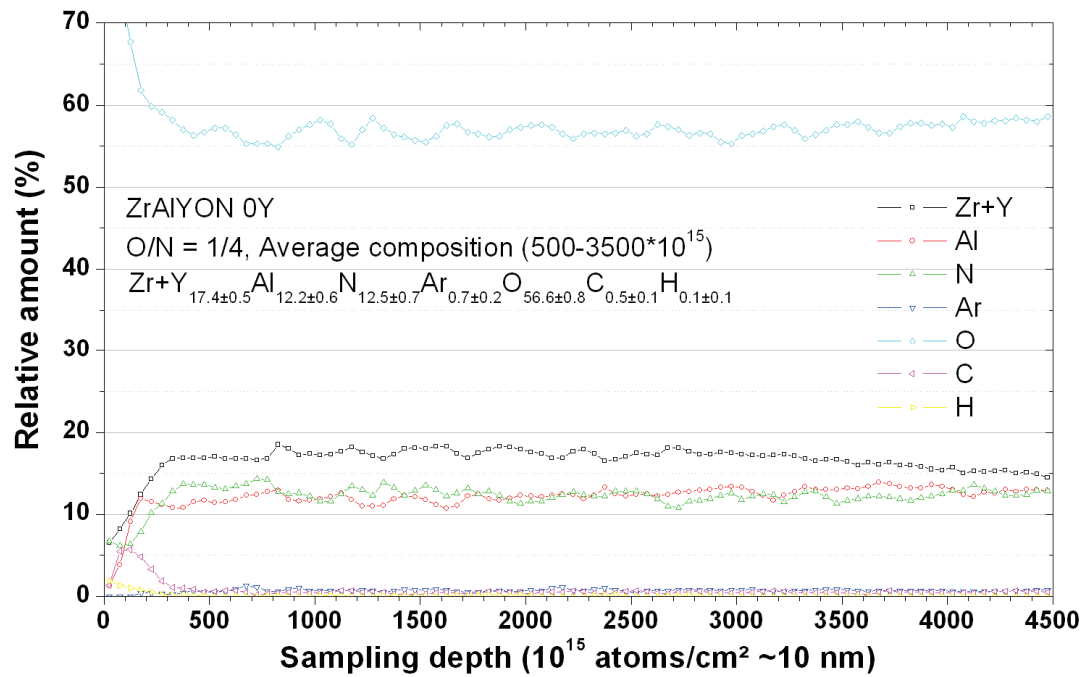
L. Hädicke

Figure 6.23: Elemental depth profile of the 0 at% Y film obtained by ERDA
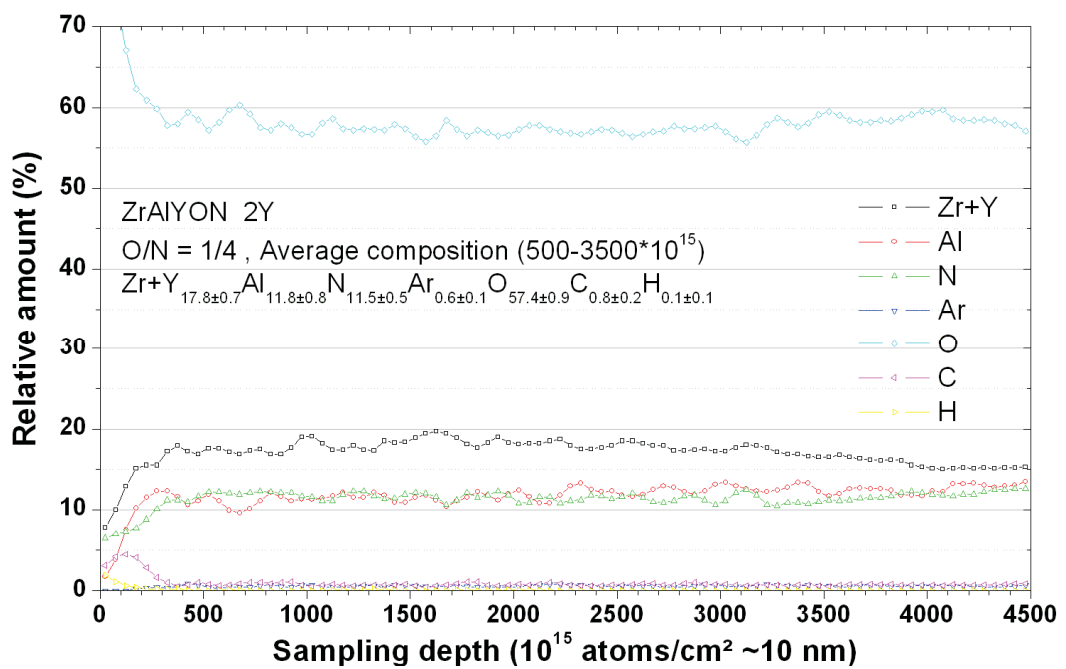

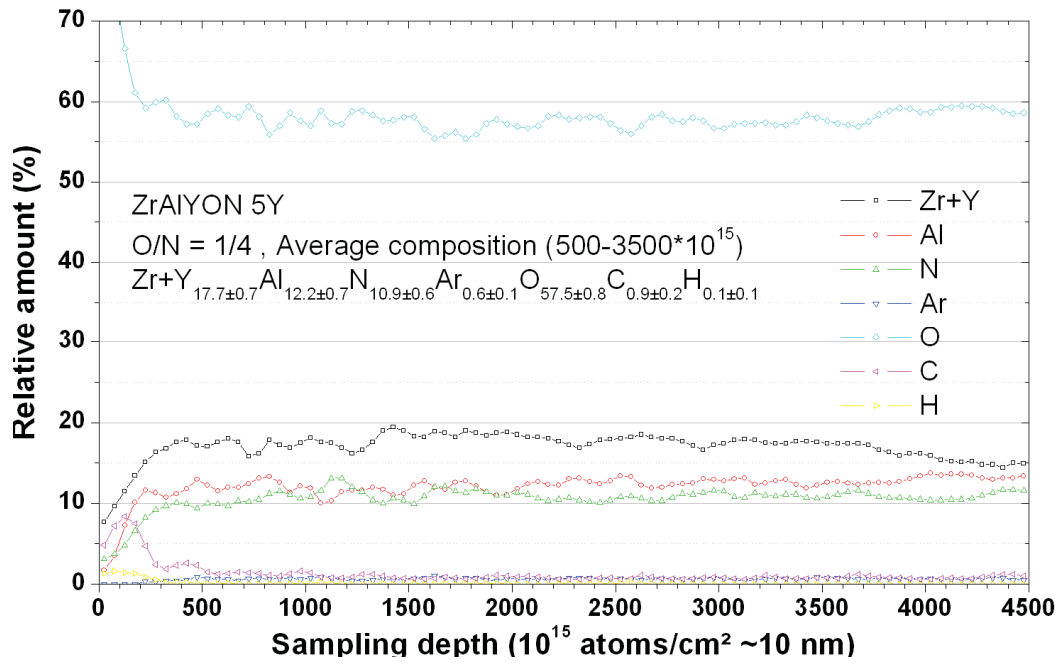Figure 6.24: Elemental depth profile of the 0.8 at% Y film obtained by ERDA

Figure 6.25: Elemental depth profile of the 1.4 at% Y film obtained by ERDA

Figure 6.26 shows a variation of the composition from about 2000 nm to the surface (0 nm) visible which is higher than in the other composition depth profiles. This variation shows a higher Zr+Y content and a lower Al and N content.
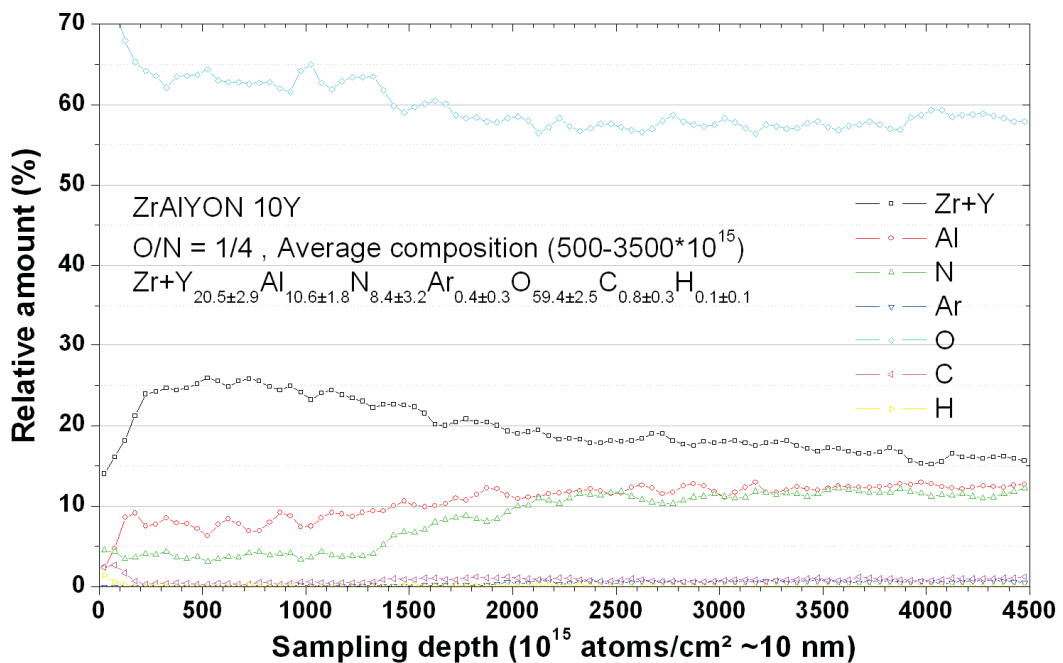

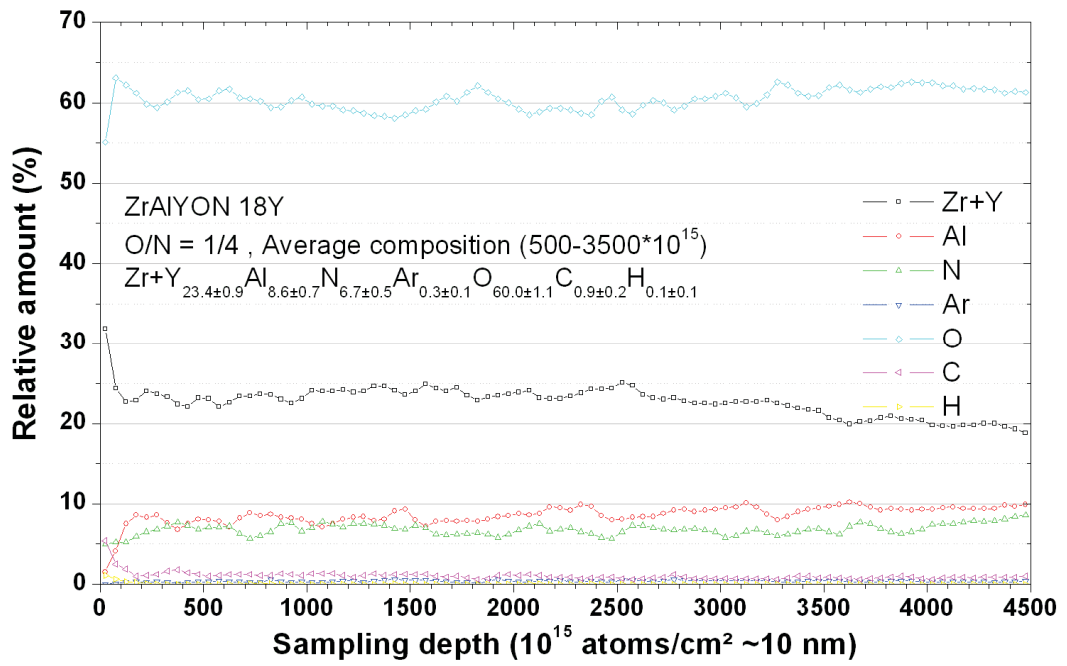Figure 6.26: Elemental depth profile of the 3 at% Y obtained by ERDA

Figure 6.27: Elemental depth profile of the 10.4 at% Y film obtained by ERDA

5.2.2   Phase analysis

As described in chapter 6.1.2 (phase analysis of the nitrides), the HRTEM was used in diffraction mode to determine the phases of the deposited films. Again the software PocessDiffraction [68] was utilized. The same procedure was performed to derive the camera length [69].
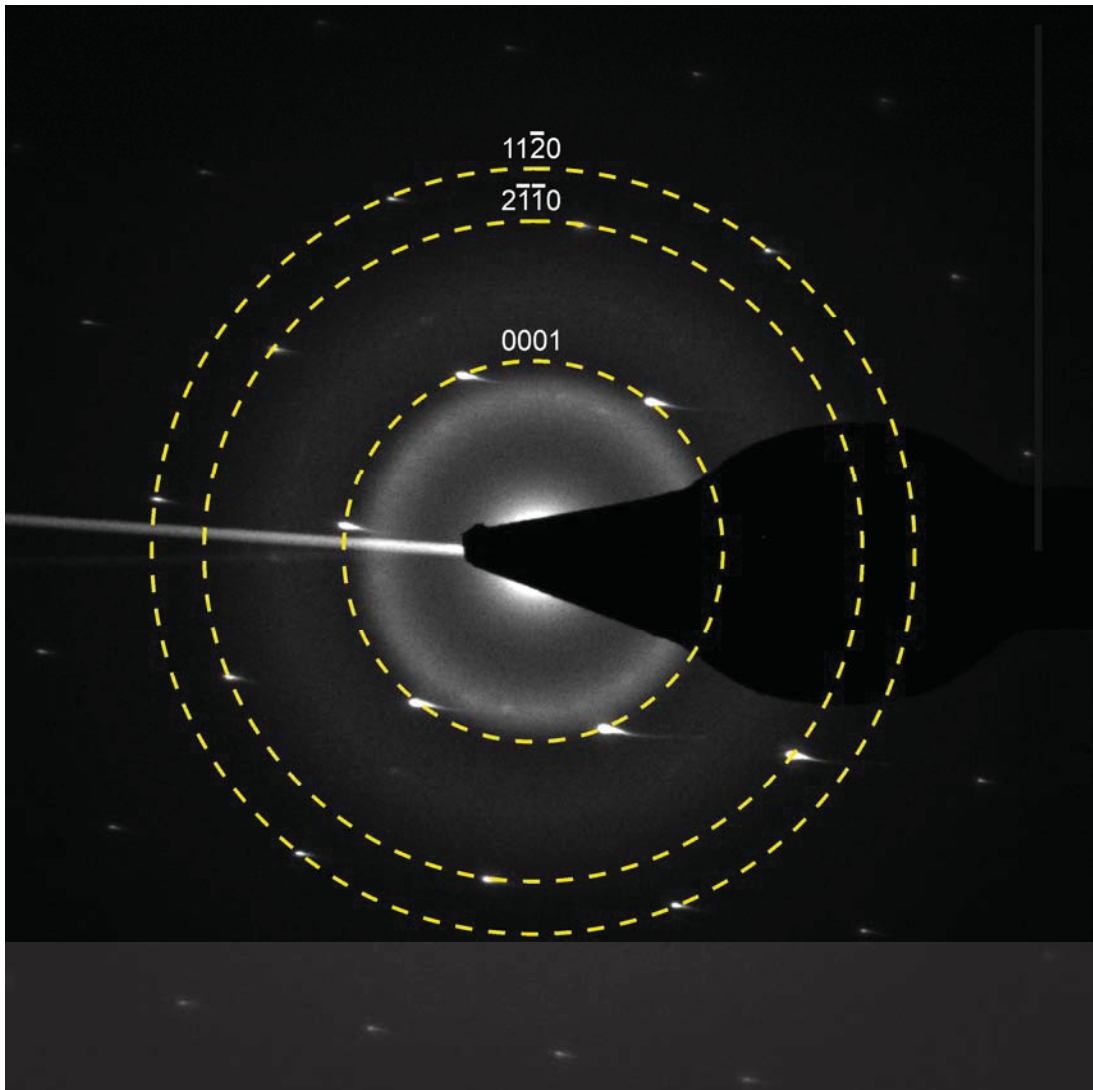

Figure 6.28: SAED at the interface of the Zr-Al-Y-O-N film with 0at%.

In Figure 6.28 the reflexes of the sapphire single crystal are clearly visible. Every ring represents one crystal plane leading to 6 reflexes in the ring of the [0001] plane. The reflexes for the [$2\overline{1}\overline{1}0$] and [$11\overline{2}0$] plane are indicated. The concentric diffuse rings which are inside the sapphire [0001] plane reflex originate from the film close to the interface.
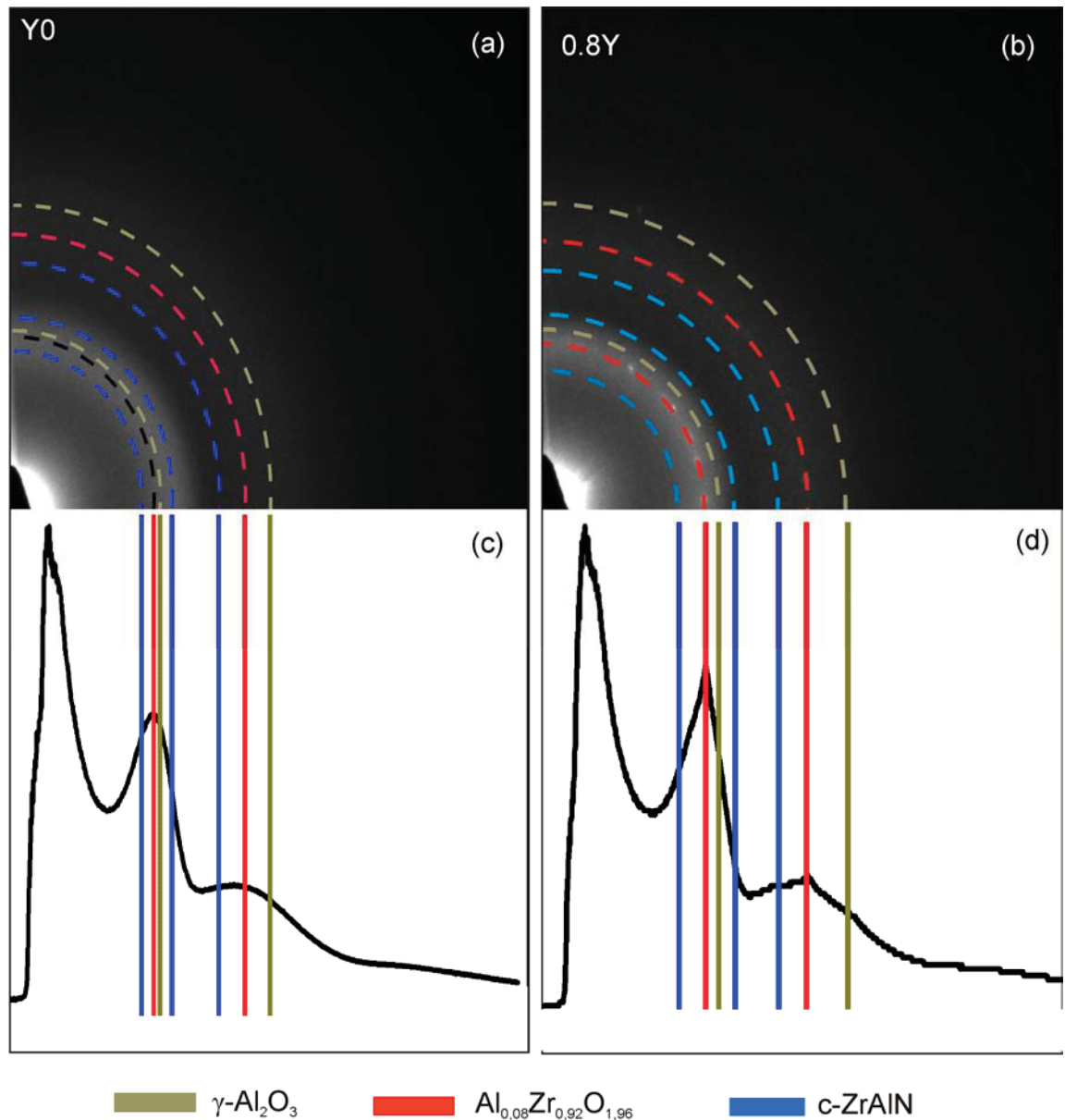
L. Hädicke

Figure 6.29: SAED for the Zr-Al-Y-O-N films with (a) 0 at% Y and (b) 0.8 at% Y and the corresponding intensity distributions (c) and (d)respectively.

The phases found in the diffraction pattern of the 0 at% Y and the 0.8 at% Y containing Zr-Al-Y-ON film are γ-Al_2O_3, t-$Al_{0.08}Zr_{0.92}O_{1.96}$ [87] and c-ZrAlN. In Figure 6.29(a) the diffuse diffraction rings indicate random oriented small crystallites. In contrast to Figure 6.29(b) where small point reflexes along the rings indicate distinct orientations of crystallites which are more frequent than others. In this case the bright points indicate larger grains (Figure 6.29(b)) since the selected area is about 1000 nm^2. The integral versus radius graph of the 0 at% Y film (Figure 6.29(c)) shows broader peaks than the 0.8 at% Y containing film (Figure 6.29 (d)).

L. Hädicke

The γ-Al_2O_3 is a fcc crystal with a lattice parameter of 3.95 Å as described in [71]. $Al_{0.08}Zr_{0.92}O_{1.96}$ is a solid solution of ZrO_2 and Al [72]. It is tetragonal and has a lattice parameter of a=3.587 Å and c=5.077 Å. Also the fcc ZrAlN phase is a solid solution of ZrN and AlN. Although Y is detected in the 0.8 at% Y containing film no YN or Y_2O_3 is formed. According to its high solubility in Zr it is supposed to be dissolved in ZrAlN [73], forming a $(Zr_{1-x}Al_x)_{1-y}Y_yN$ solid solution.
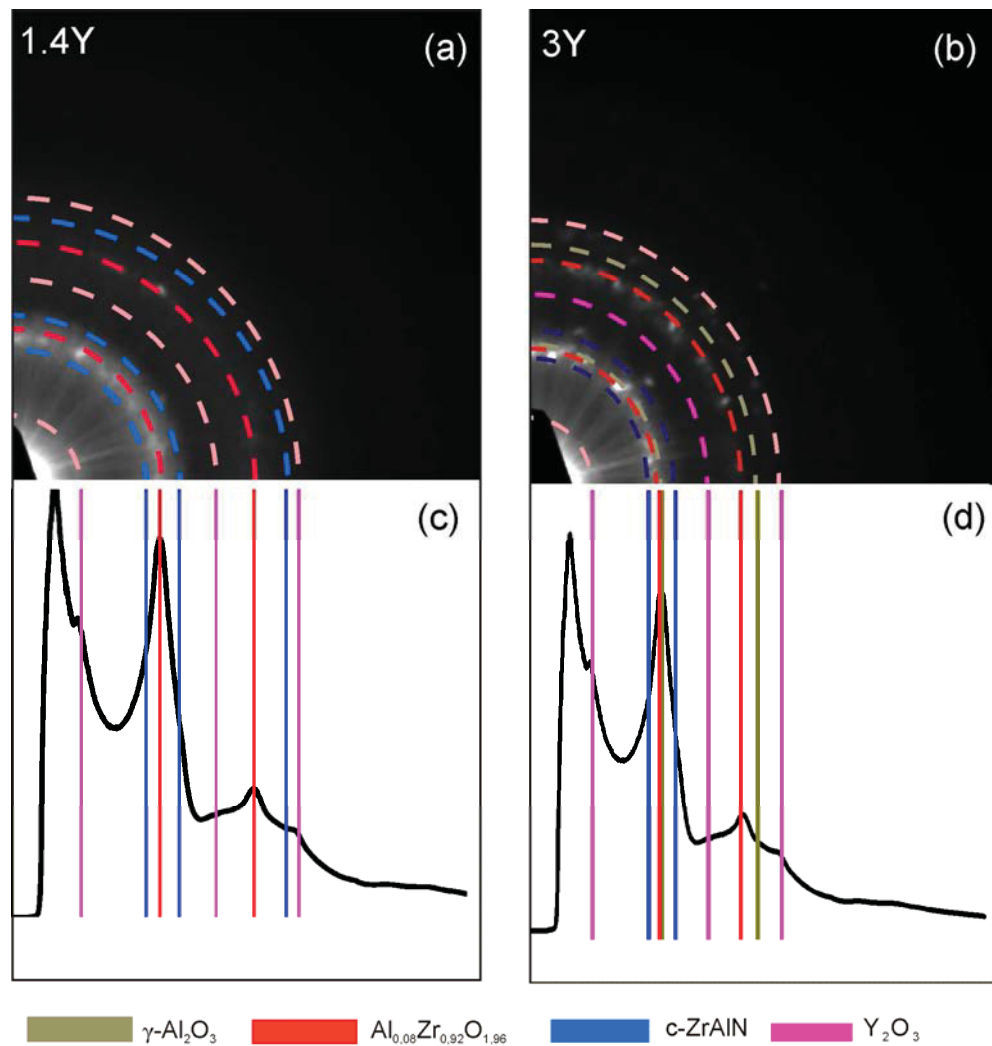

Figure 6.30: SAED for the Zr-Al-Y-O-N films with (a) 1.4 at% Y and (b) 3 at% Y and the corresponding intensity distributions (c) and (d) respectively.

At a content of 1.4 at%, in addition to γ-Al_2O_3, $AlZrO_2$ and fcc-ZrAlN, a fcc-Y_2O_3 is formed. This Y_2O_3 is larger than the other phases and has a parameter of 10.6 Å [81]. A comparison between Figure 6.30 (b) and (d) shows more and stronger intense spots than in Figure 6.30. This indicates an increase in crystallinity, accompanied by sharper rings and higher peaks in the intensity integral versus radius diagrams.

L. Hädicke

In the film with the highest Y content, the rings are very sharp, as shown in Figure 6.31. In opposite to the other coatings no spot reflexes along the diffraction rings are visible. So the combination of sharp rings and no spots hints towards coating with smaller crystallites but less amorphous fraction than the samples with lower Y content, similar to the results for Zr-Al-Y-N films. The high reflex of $Al_{0.08}Zr_{0.92}O_{1.96}$ shows a variation along the ring which is typical for a preferred orientation.
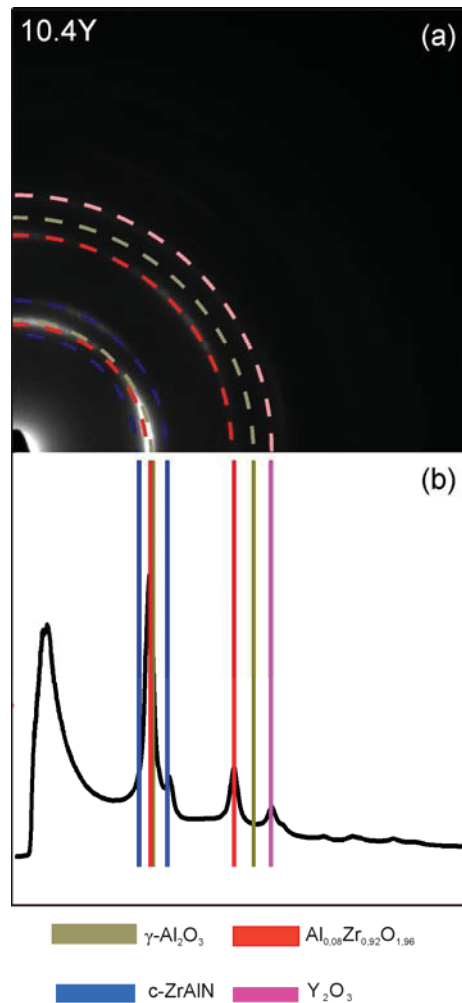

Figure 6.31: : SAED for the Zr-Al-Y-O-N films with (a) 10.4 at% Y and the corresponding intensity distributions (b).

An XRD investigation of the powdered sample material shows no remarkable features, see Figure 6.32. The angle range where the phases should have their highest intensity reflexes have broadly increased intensity but no particular peak can be detected. This shows that the microstructure is too fine to be analysed by XRD.
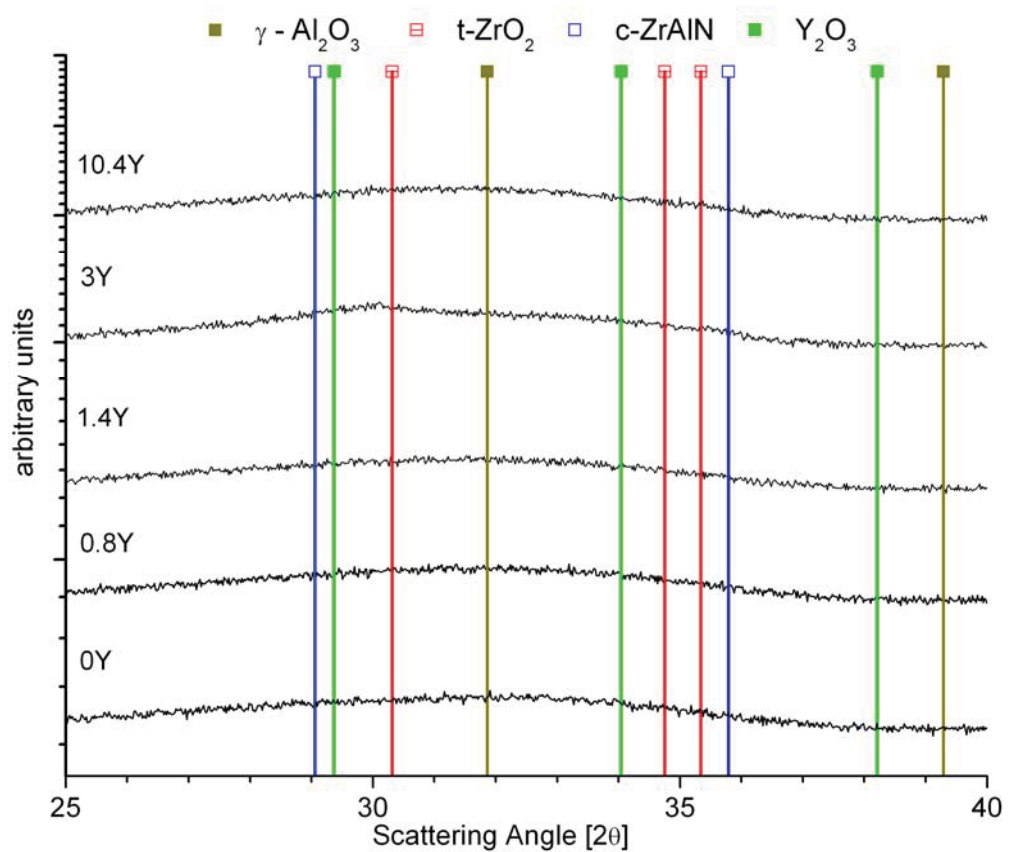
L. Hädicke

Figure 6.32: XRD of all oxinitrides in the as-deposited state.

5.2.3   Structure and morphology

By SEM the fracture surface was investigated. These samples are deposited on silicon for a better conductivity and therefore a better image of the samples.
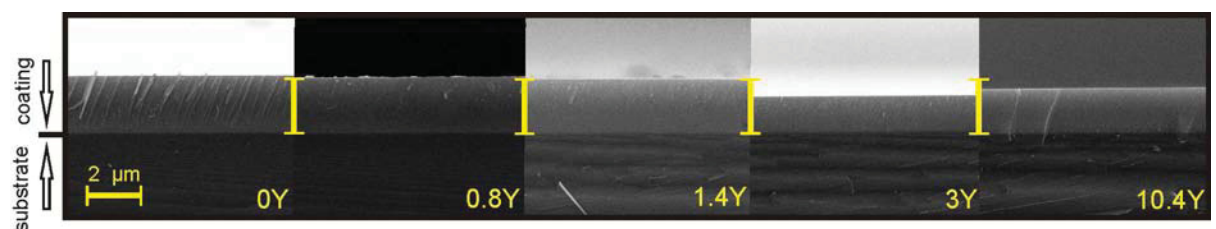

Figure 6.33: SEM cross section images of the oxinitrides with 0, 0.8, 1.4, 3 and 10.4 at% Y

All SEM cross section images (Figure 6.33) are taken at the same magnification and therefore have the same scale. The maximum thickness is measured for the 0Y film with 2.6 µm. With increasing Y content the thickness decreases from about 2.5 µm for the 0.8Y and

L. Hädicke

the 1.6Y film, to 1.7 μm and 2.0 μm for the 3Y and 10.4Y film, respectively. A reason for the slow deposition rate may be the target poisoning caused by the incorporated oxygen and the low diffusion rate of Y.

The SEM fracture surface shows no remarkable features in the films, they are very dense. Furthermore, all samples were investigated with HR-XTEM. At this high magnification the microstructure of the samples is visible and shows small crystalline areas which can be described as grains, embedded in an amorphous phase.
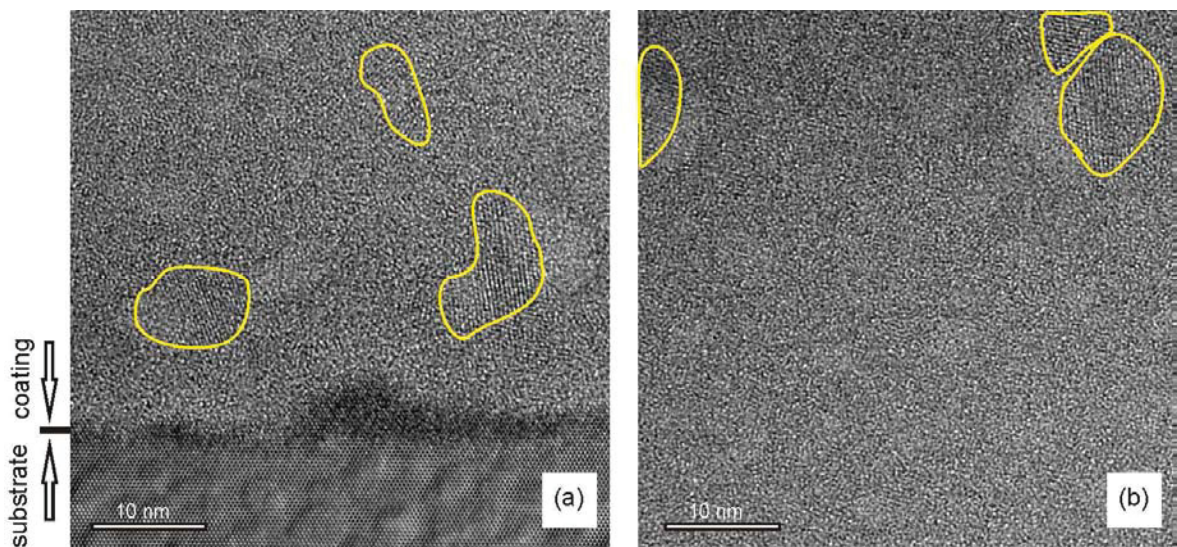

Figure 6.34: HR-XTEM image of the 0Y film of the (a) substrate-film interface and (b) the film bulk

The 0Y film shows wide areas of non crystalline structures. Especially, at the interface to the sapphire substrate, there is an amorphous layer, typical for films grown on Ar+ - etched sapphire substrates, see Figure 6.34 (a). The estimated grain size for the small crystallites embedded in the amorphous structure is ~11 nm, see Figure 6.34 (a) and (b).
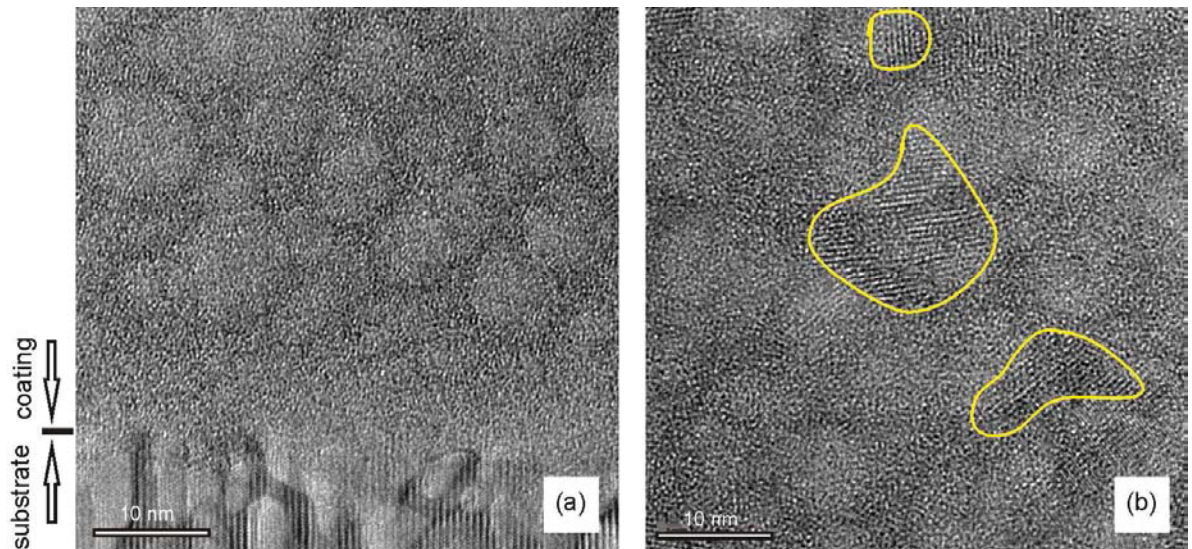
L. Hädicke

Figure 6.35: HR-XTEM image of the 0.8Y film of the (a) substrate-film interface and (b) the film bulk.

With increasing Y content the microstructure of the Zr-Al-Y-O-N films changes to more crystallinity, larger grains and smaller amorphous regions. The estimated average grain size for the 0.8 at% Y containing film is 12 nm.
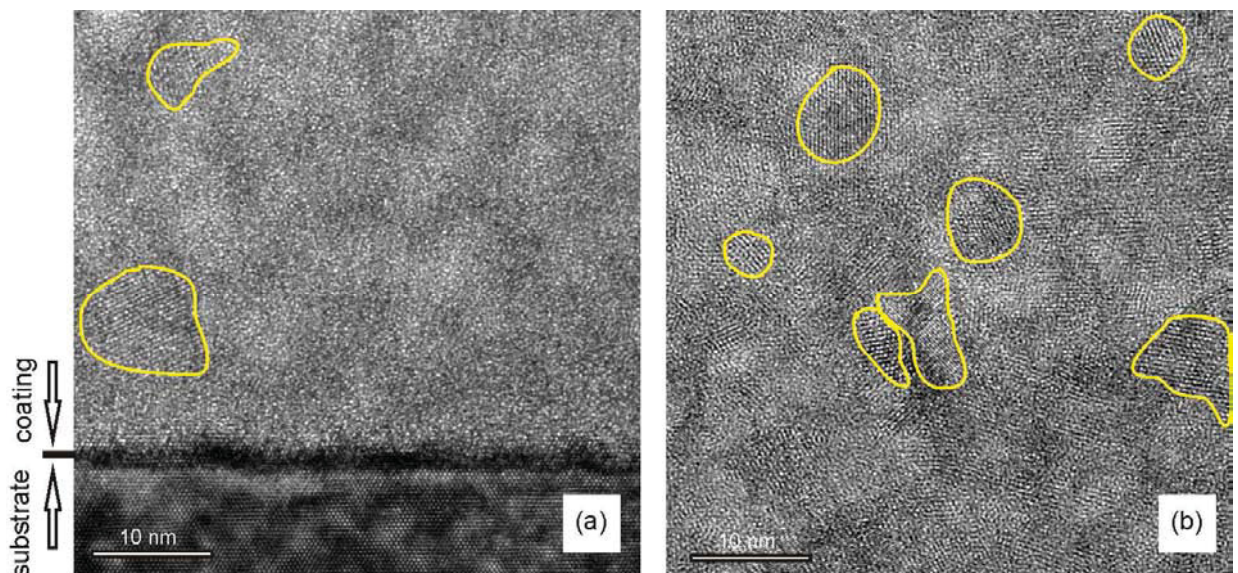

Figure 6.36: HR-XTEM image of the 1.4Y film of the (a) substrate-film interface and (b) the film bulk

The 1.4Y and the 3Y films show an increase in crystallinity and therefore more grain, see Figure 6.34 and 6.37 (a) and (b). The average grainsize is 7 nm and 10 nm for the 1.6Y and 3Y film, respectively and is decreased compared to the Y-free film. This behaviour is in

L. Hädicke

excellent agreement to the SAED analysis indicating decreasing grainsize and amorphous fractions of the Zr-Al-Y-O-N films with increasing Y-content.
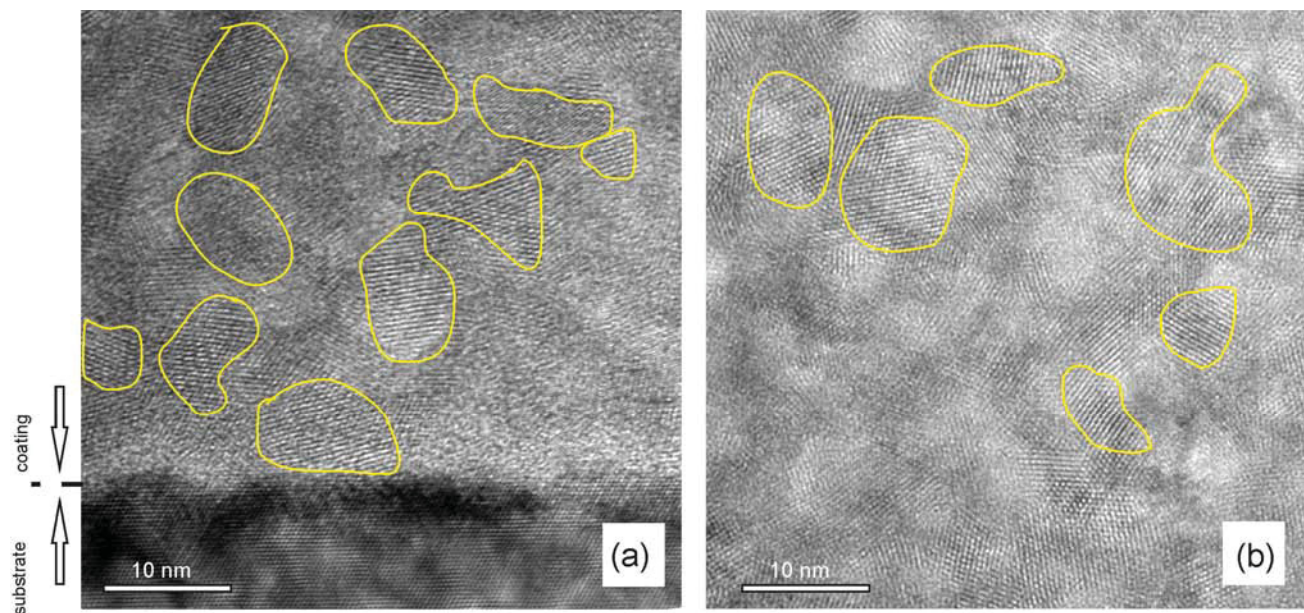

Figure 6.37: HR-XTEM image of the 3Y film of the (a)substrate-film interface and (b) the film bulk.
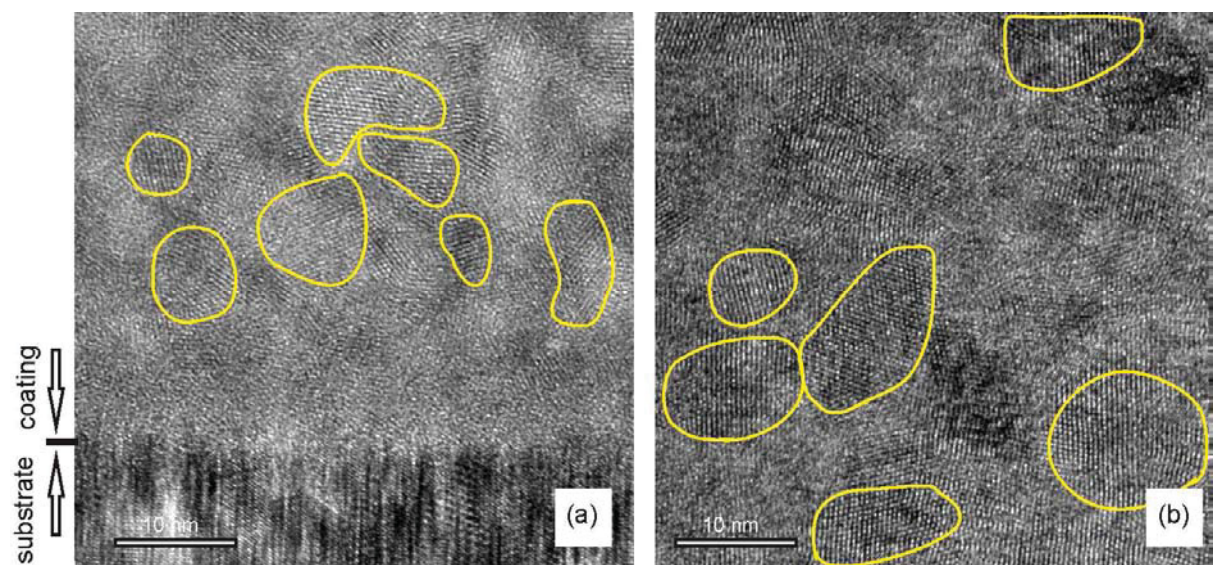

Figure 6.38: HR-XTEM image of the 10.4Y film of the (a) substrate-film interface and (b) the film bulk

For the highest Y containing Zr-Al-Y-O-N film with 10.4 at% Y (10.4Y) the grain size is ~10 nm and the amorphous region separating them is thin, see Figure 6.38 (a) and (b).

L. Hädicke

5.2.4 Mechanical properties

The hardness (H) and the elastic-modulus (E) of the films were measured on samples deposited on sapphire. Figure 6.39 presents a hardness of ~8.3 GPa for the coatings below 3 at% Y, but at an Y content of 10.4 at% the hardness increases to 12.2 GPa. This can be explained with the higher crystallinity of the sample.
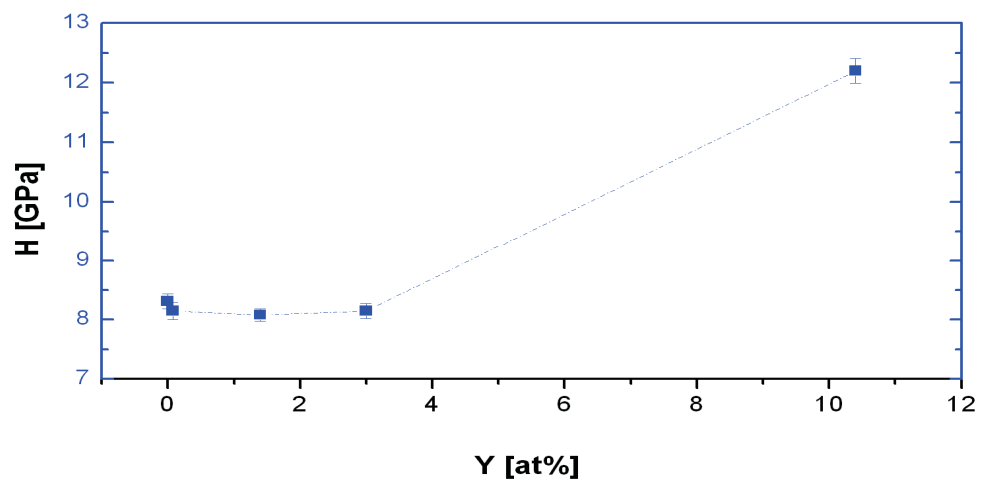
Figure 6.39: Hardness versus Y-content of the Zr-Al-Y-O-N film.

The Young's modulus has a maximum of 169.9 GPa at an Y-content of 10.4 at% Y. At a lower Y-content the Young's modulus decreases to a level of about 150 GPa, see Figure 6.40. Again this can be explained by the increasing amorphous fraction because amorphous regions have lower elastic –modulus as their crystalline counterparts.
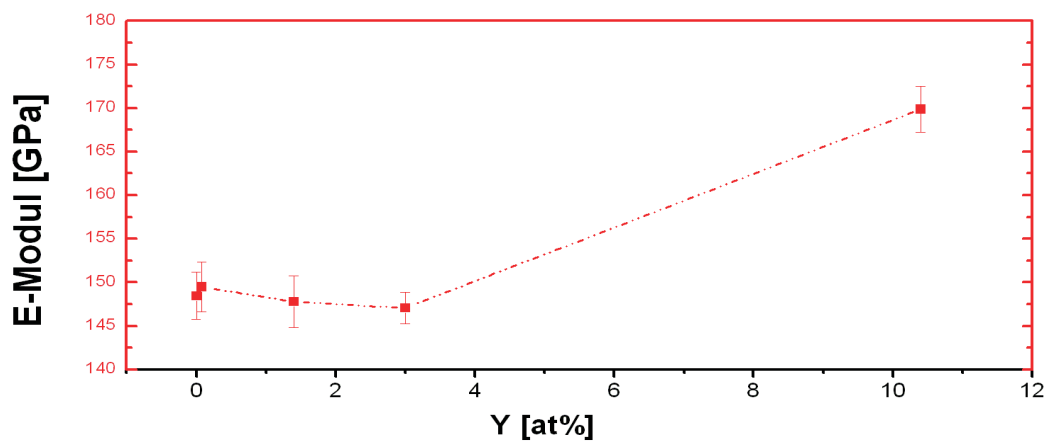

Figure 6.40: Young's modulus versus Y-content.

L. Hädicke

5.2.5   Thermal stability

An investigation of the thermal stability shows two clearly distinguishable reactions, named Ex 1 and Ex 2. In the 0Y film a third reaction, Ex 3,can be detected (Figure 6.40).

At smaller temperatures than the peak temperature Ex 1, all samples show a moderate exothermal heatflow which starts at about 500°C, the deposition temperature. This heatflow is attributed to recovery.

The Ex 1 reaction has its maximum at ~877°C for the 0Y film, and shifts with increasing Y content to higher temperatures. At a Y content of 0.8 and 1.6 at% Y the maximum temperature is about 896°C and decreases to 888°C for the 3Y and 10.6Y film. A quantitative comparison of the energy release of Ex 1 shows no particular difference or tendency. With higher temperatures the heatflow remains exothermal up to Ex 2.

Ex 2 is also an exothermal reaction but has a sinusoidal shape and is by a factor 5 smaller than Ex 1. A sinusoidal shape can be interpreted as two reactions with interfering endothermic and exothermic contribution. This reaction shows an increase of temperature with increasing Y content. At a content of 0 at% Y the reaction maximum is at 1167°C and increases to 1192°C with 0.8 at% Y. From an Y content of 1.4 at% to 10.4 at% the reaction temperature changes to ~ 1225°C.

The 0Y film shows a third reaction at 1365°C. This Ex 3 is clearly exothermal and releases about the same energy than Ex 2.
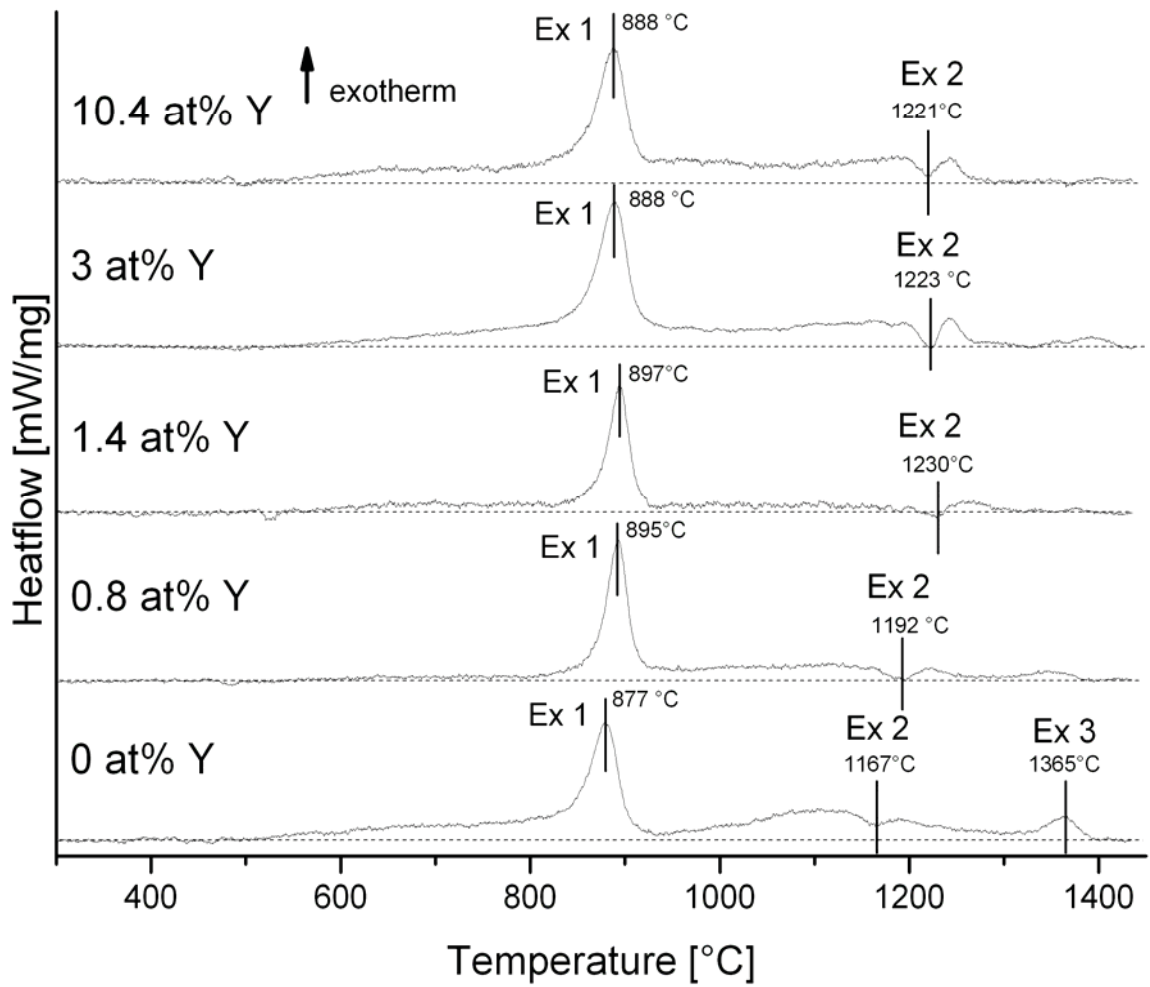
L. Hädicke

Figure 6.40: Dynamical DSC traces for Zr-Al-Y-O-N with 0, 0.8, 1.4, 3 and 10.4 at% Y.
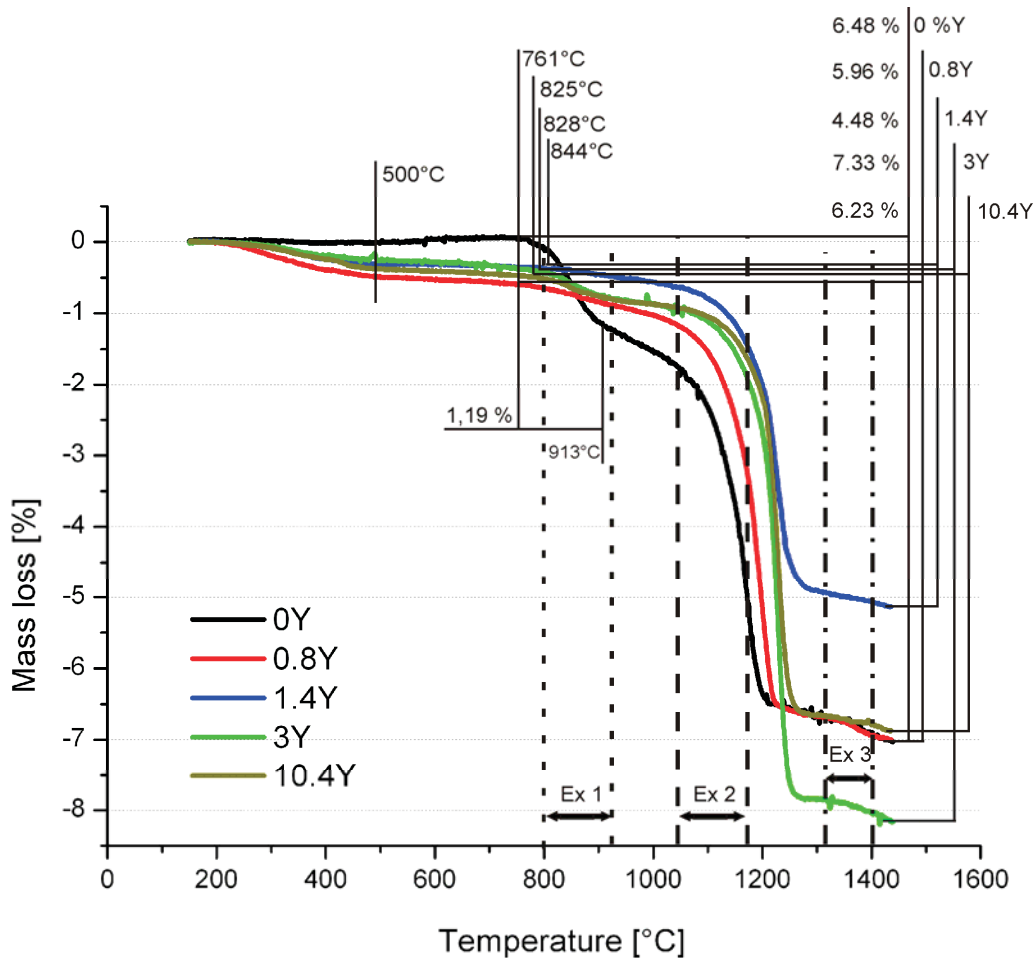
Figure 6.41: Mass loss of all samples versus temperature during DSC to 1450°C with a heating rate of 20K/min.

Parallel to the DSC a TGA measurement was executed. As displayed in Figure 6.41 there is a clear difference between the Y-free and the Y containing films.

The film without Y, shows a relatively constant mass up to 761°C. Between 761°C and 913°C the sample looses about 1.19% of its mass. This mass loss occurs during the Ex 1 reaction. For the 0Y film, at about 1010°C a second mass loss reaction occurs. This mass loss stops at ~1200°C close to the offset temperature of Ex 2.

The Y containing films continuously loose mass of ~0.5 % up to 500°C and then stay stable up to ~ 830°C where a pronounced mass loss reaction starts. This additional mass loss, which is in the dimension of 0.5%, stops at approximately 950°C and occurs in the temperature range of Ex 1. The Ex 2 mass loss is higher than the mass loss observed during Ex 1. This loss is measured between 1000°C and 1280°C for all Y containing films. At a temperature of 1365°C a kink is visible in the characteristics of all samples. Ex 3 is detected in the same temperature range around 1365°C. This mass loss is consequently attributed to Ex 3. The

L. Hädicke

relation of mass loss and Y content shows no tendency. The most stable sample is the 1.6Y sample with a loss of 4.48 % and the highest loss of 7.33% is detected for the 3Y film. The mass losses of the Zr-Al-Y-O-N films can basically attributed to release of N and O, as detected by simultaneous mass spectrography, see Figure 6.42, 6.43, 6.44 for the films with 0.8, 1.4 and 10.4 at% Y.
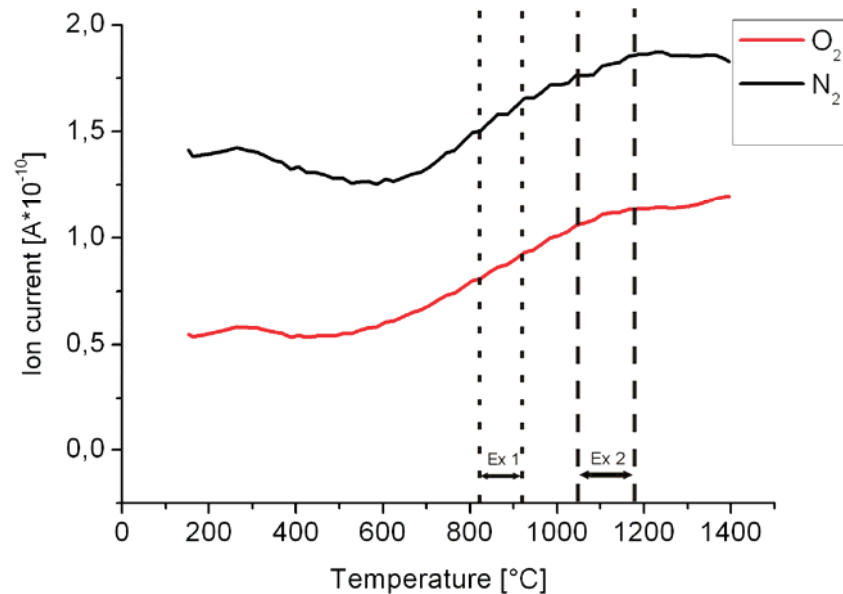
Figure 6.42: Mass spectroscopy of the Zr-Al-Y-O-N film with 0.8 at% Y.

The volatile species for the 0.8Y film are N_2 and O_2 where N_2 has a higher signal than O_2. Both have a comparable shape and show an emission up to ~500°C where a loss of 0.5% is detected in TGA measurement. Between 600°C and 1100°C the mass loss stays at a constantly increasing rate up to Ex 2.

Figure 6.43: Mass spectroscopy of the Zr-Al-Y-O-N film with 0.1.4 at% Y.

L. Hädicke

The 1.4Y film shows comparable amount of N_2 and O_2 in the measurement. Both signals increase with temperature only N_2 has a decreasing current between 400°C and 800°C.

Figure 6.44: Mass spectroscopy of the Zr-Al-Y-O-N film with 10.4 at% Y.

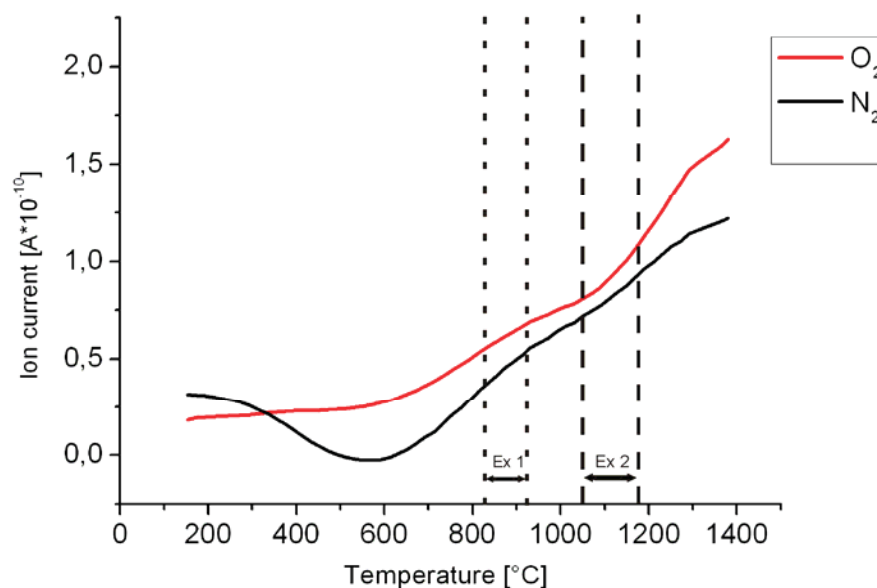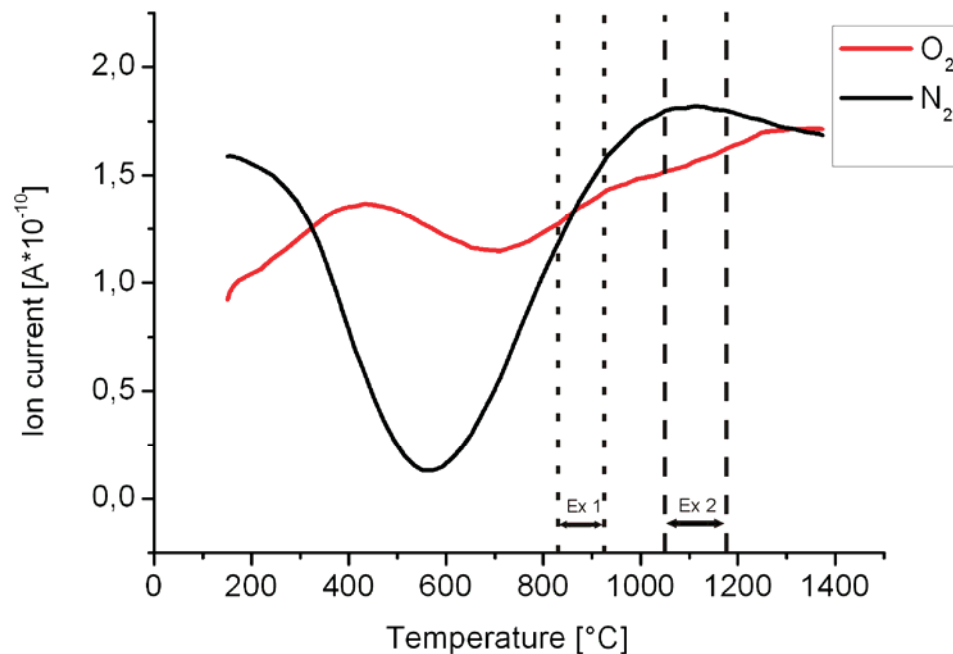Nitrogen shows in Figure 6.44 a high reduction between 300°C and 900°C, the rate decreases up to the deposition temperature but increases from ~550°C up to a maximum at ~1100°C. Between ~1150°C and 1450°C a slight rate decrease is observable. Oxygen shows an increasing rate up to the deposition temperature of ~500°C. From ~ 500°C to ~650°C the ion current of O_2 decreases. The signal starts increasing at ~650°C. The used atmosphere in these measurements was Argon so reactions between atmosphere and samples can be avoided.

5.2.6   Phase stability

All samples where investigated by in-situ XRD. Figure 6.45 gives an overview of all compositions and measured temperatures between the scattering angle 2Θ of 30° to 37°. This measurement was taken from samples deposited on sapphire. At an angle of 2Θ=35.75° the [111] reflex of c-ZrAlN is indicated. The data is not temperature corrected therefore the peak shifts with temperature. At lower temperatures than 1100°C no change in the XRD graph is

L. Hädicke

observable for all compositions. Although Ex 1 shows a stronger exothermal peak as compared to Ex 2 no change in the in situ XRD measurement can be detected consequently. The Ex 1 reaction measured at around 880°C may originate from recovery processes of the film and the detected N_2 and O_2 release.
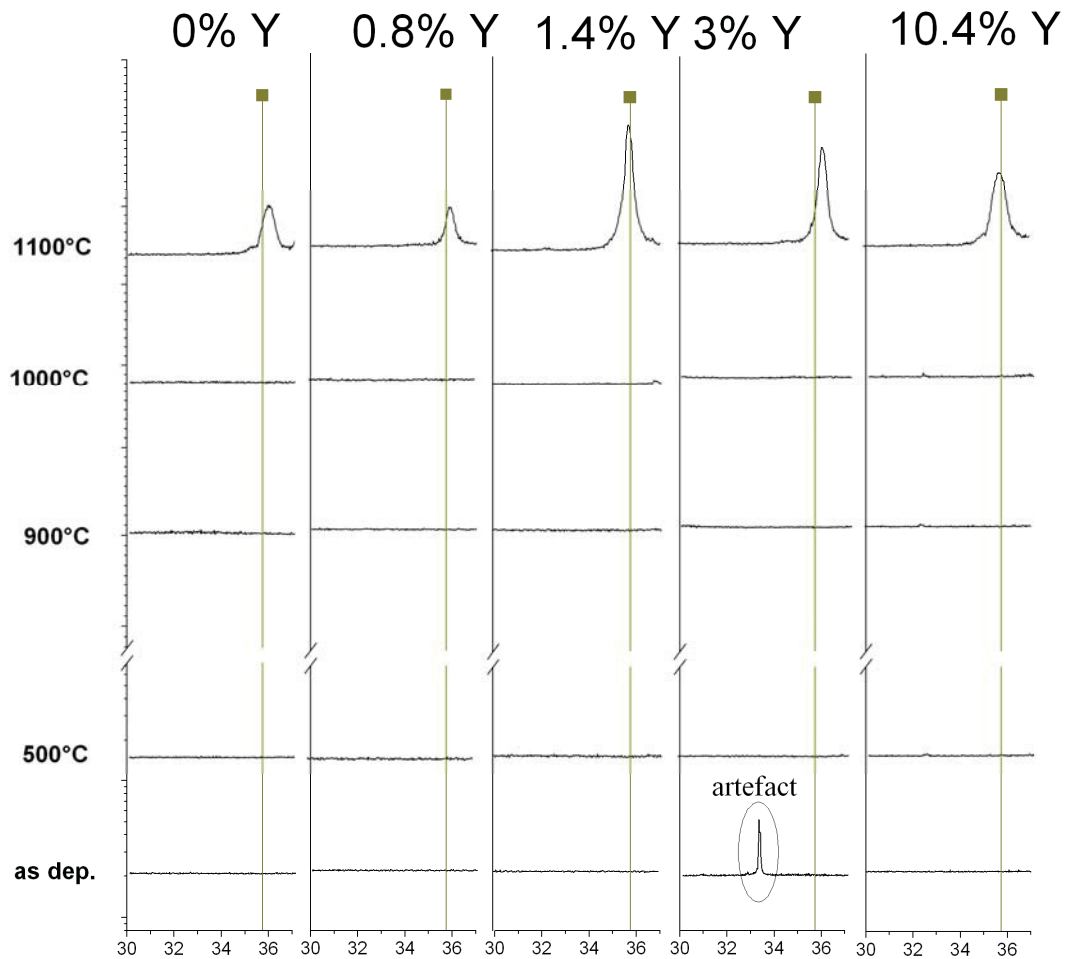
Figure 6.45: Matrix of in-situ XRD measurements of all films at several temperatures with the marked reflex of c-ZrN [111].

To investigate the formation of phases during the DSC measurement the samples were heated beyond the individual reaction temperatures and subsequently quenched with 50K/min to conserve their status.

The 0 at% Y film was annealed to 975°C and 1275°C and investigated with XRD at RT. These measurements are then combined in Figure 5.24 with the RT-XRD of the as-dep. film and the sample after the DSC measurement to 1450°C.

L. Hädicke

The overview reveals the phase transformation during the DSC measurement. Based to these studies Ex 1 is dedicated to a recrystallization or even recrystallization reaction as presented by the at 975°C quenched sample where the phases are developed compared to the as-deposited state. In the sample annealed to 1275°C a phase change is observable during Ex 2 reaction. The γ-Al$_2$O$_3$ transforms to α-Al$_2$O$_3$ (corundum) and the c-ZrAlN solid solution segregates to c-ZrN as indicated by the c-ZrN peaks which are situated exactly at the positions given by the database [74]. The t-ZrO$_2$ phase shows no change.

After the sample has undergone the entire DSC cycle it was measured at room temperature. This sample shows another change in the phase composition. The t-ZrO$_2$ transformed into a mixture of monoclinic ZrO$_2$ and cubic ZrO$_2$ whereas the other phases stay stable and show no shift.
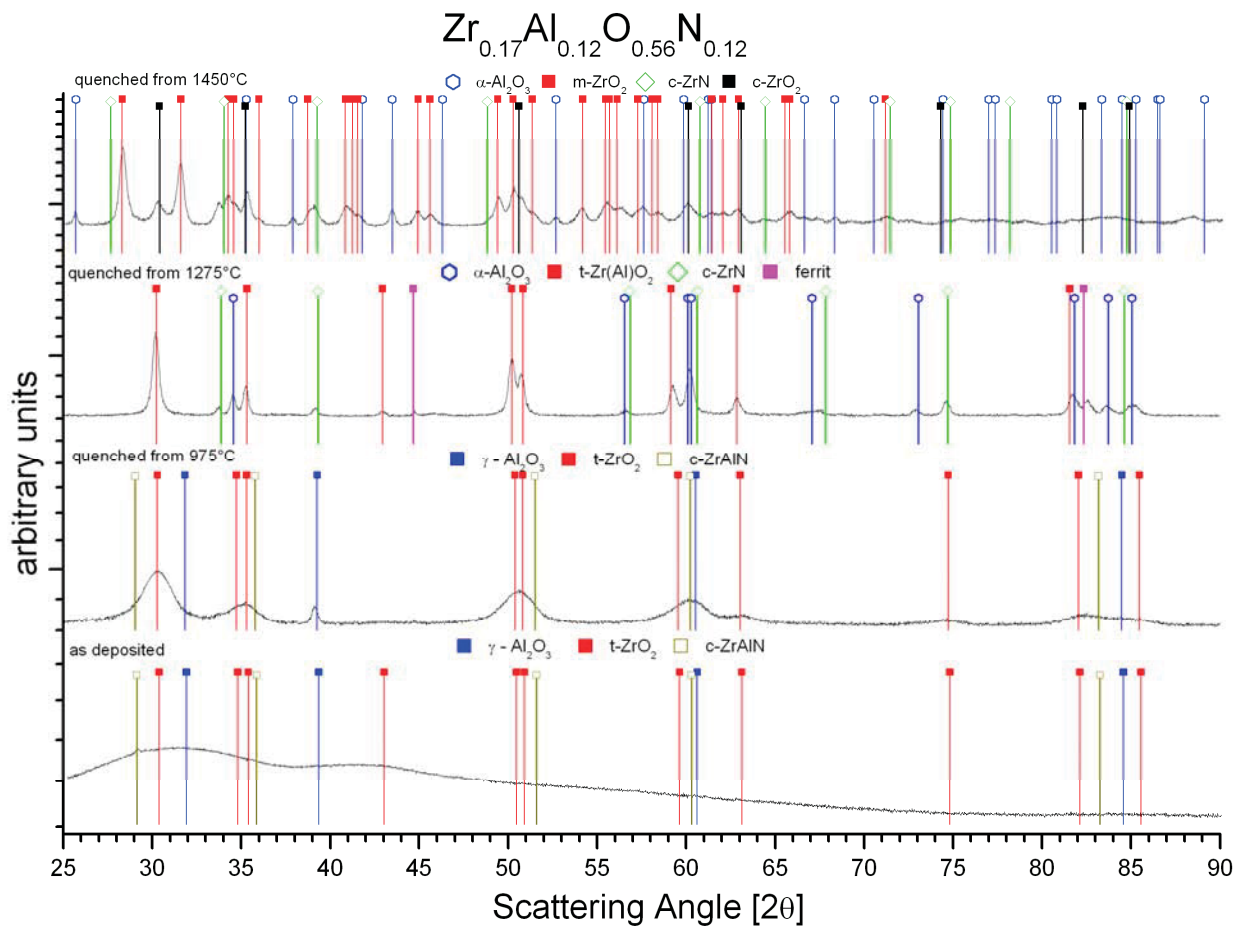

Figure 6.46: RT-XRD of 0Y in the as-deposited state and after annealing to 975°C, 1275°C and 1450°C.

The same procedure was applied on the 3Y film where in contrast to the 0Y sample a Y$_2$O$_3$ phase was detected. At 975°C no change compared to the as-deposited state in the phase

L. Hädicke

composition is observable. The γ →α transformation of Al_2O_3 and the decomposition of c-ZrAlN occurred corresponding to the 0Y sample. In contrast to the t- ZrO_2 phase formed in the 0Y film, the sample with 3at% Y forms 6.5 YSZ instead of t-ZrO_2. The 6.5 YSZ (6.5 mol % Y_2O_3 stabilized t-ZrO_2) stays stable up to the maximum DSC temperature of 1450°C, see Figure 6.46.
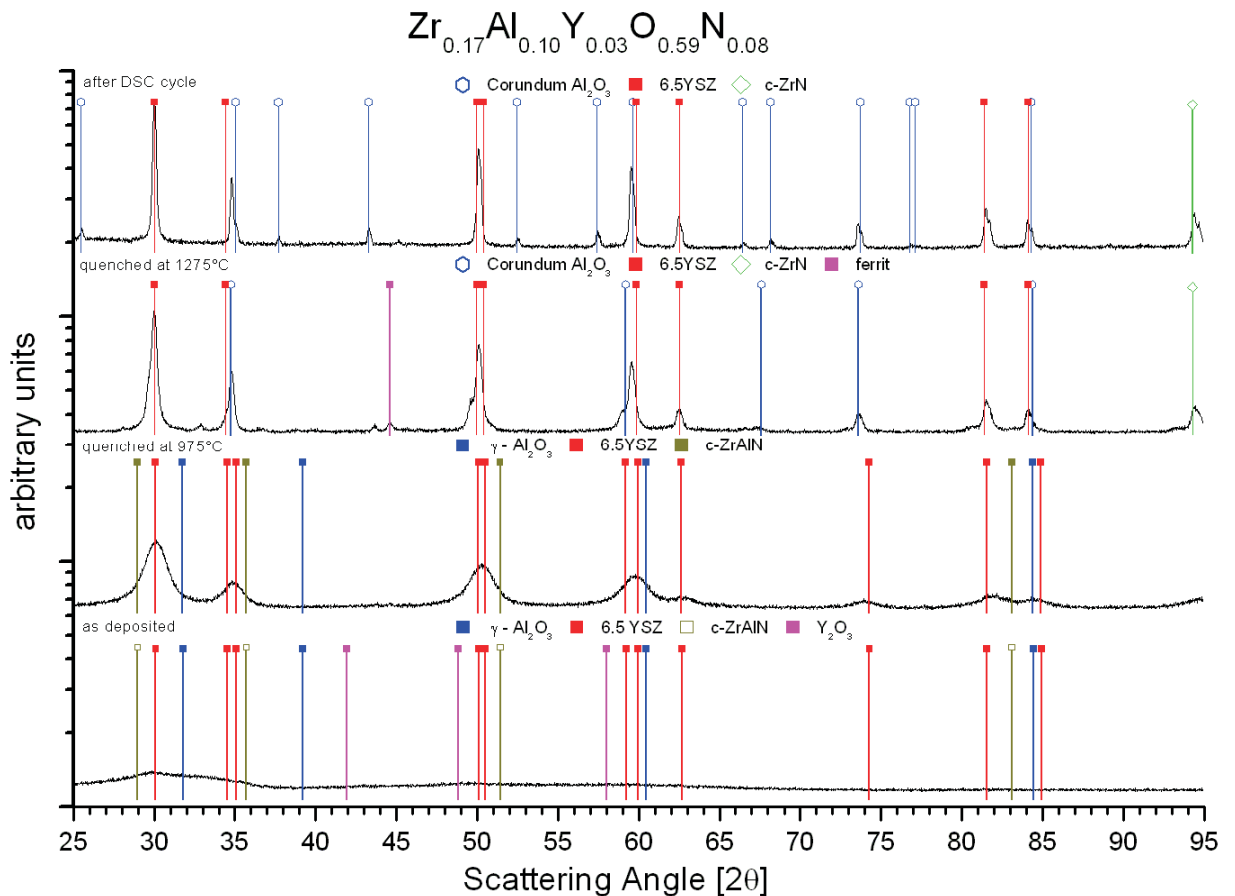
Figure 6.47: RT-XRD of 1.4Y in the as-deposited state and after annealing to 975°C, 1275°C and 1450°C.

All DSC investigated samples (i.e. after heat treatment to 1450°C) were measured with XRD at RT and are presented together in Figure 6.47. In this illustration the evolution of the formed phases can be seen. All samples show the γ →α transformation of Al_2O_3 and the decomposition of cubic and hexagonal ZrAlN into stable c-ZrN, no h-AlN can be detected. These phases vary in their reaction temperature with increasing Y content. In contrast to the formed ZrO_2 which decomposes into m-ZrO_2 and c-ZrO in the Y-free sample and into 3.5 YSZ (3.5 mol % Y_2O_3 stabilized t-ZrO_2) and m-ZrO_2 in the 0.8 at% sample, whereas at higher Y contents no change of the phase is observable.

L. Hädicke
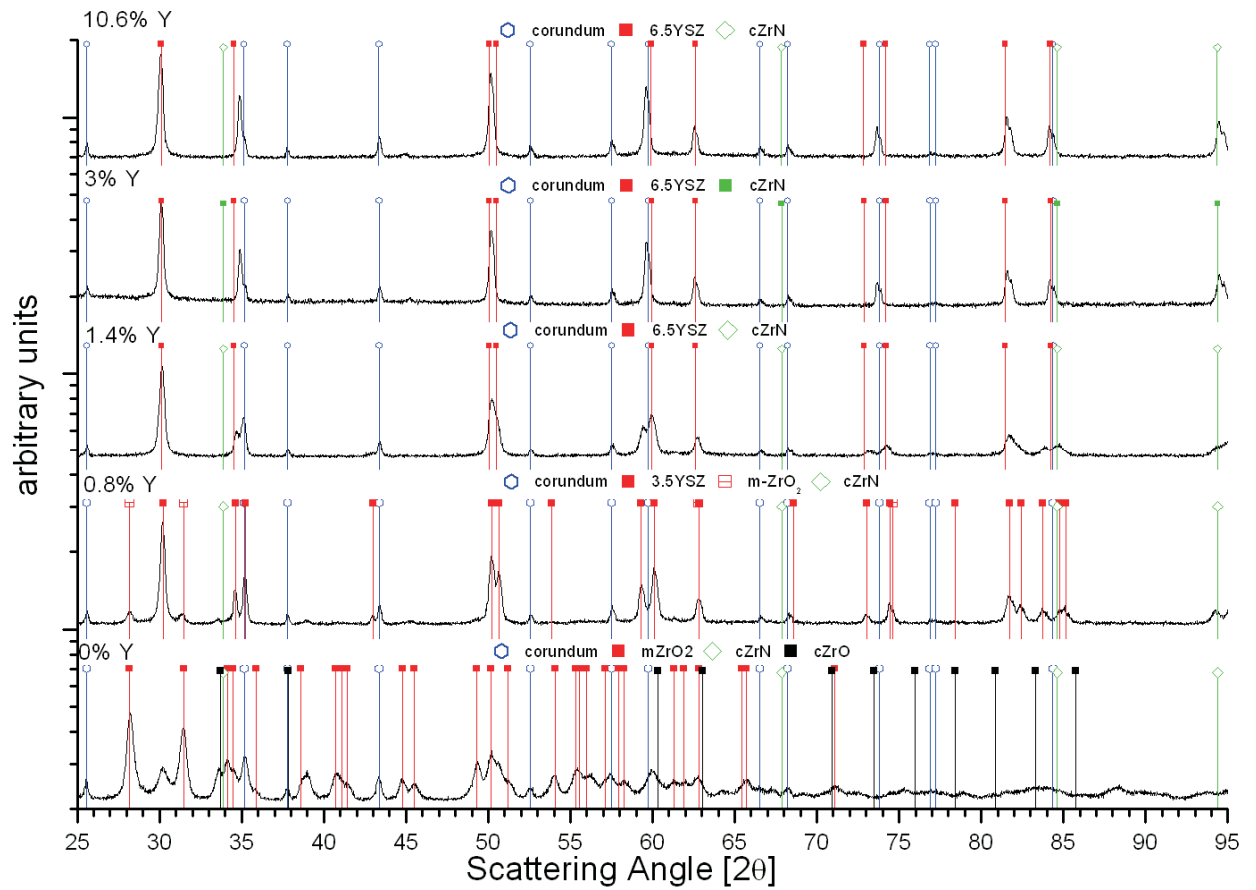
Figure 6.48: RT-XRD patterns of the Zr-Al-Y-ON films with 0, 0.8, 1.4, 3 and 10.4 at% Y after DSC to 1450°C in Ar-atmosphere.
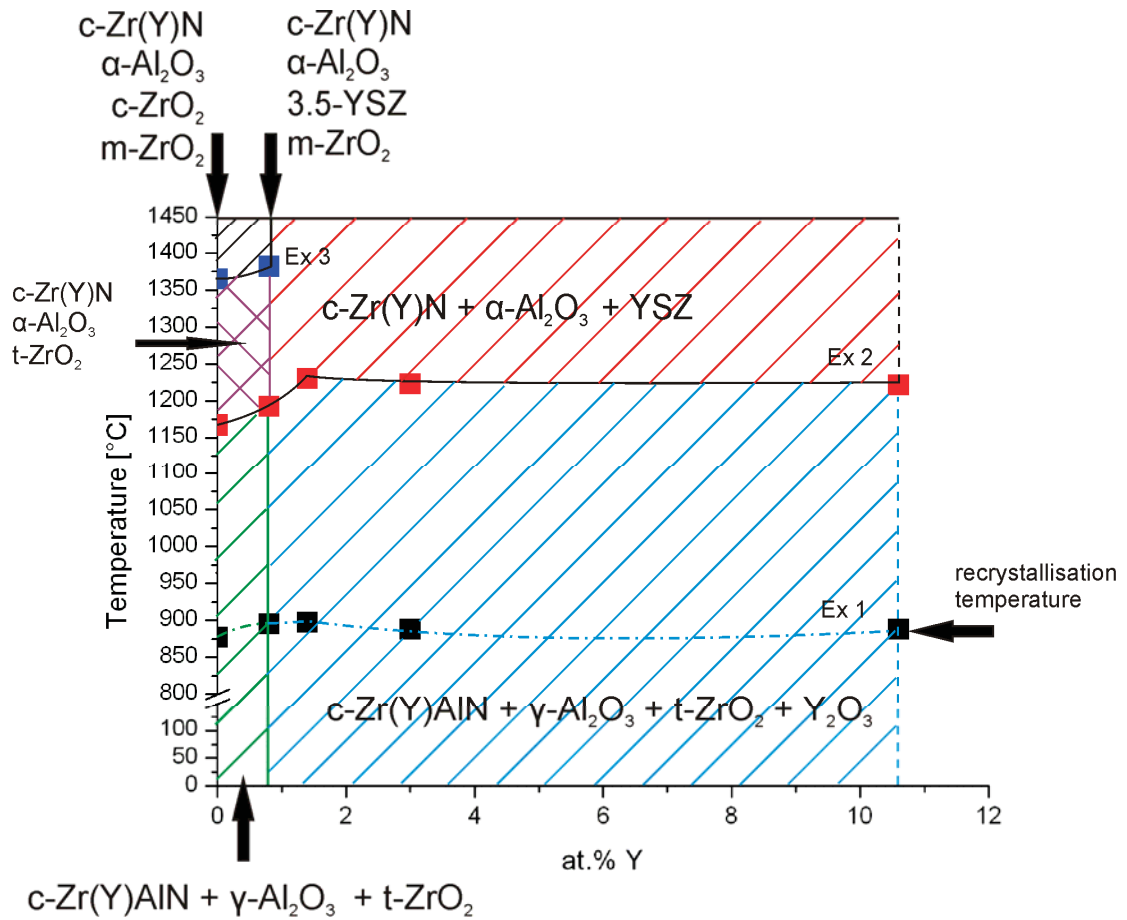
Figure 6.49: Phase stability range in the Zr-Al-Y-O-N films as a function of their Y contents.

As indicated in Figure 6.49, Yttrium stabilises the irreversible $\gamma \rightarrow \alpha$ transformation (Ex 2) of Al_2O_3 from 1167°C to ~1220°C.

 In the as-dep. state of the films Y is dissolved in c-$(Zr_{1-x}Al_x)_{1-y}Y_yN$ as a solid solution. At higher temperatures than Ex 2 and an Y content of more than 0.8 at% the Y_2O_3 and t-ZrO_2 phases form YSZ. The Y-free film and the 0.8 at% Y film show stable t-ZrO_2 up to ~1375°C were t-ZrO_2 decays into monoclinic and cubic ZrO_2 as it is indicated for the Y-free film and into m-ZrO_2 and 3.5-YSZ as it is observed for the coating containing 0.8 at% Y. A further increase of Y in the film shows no effect in the detected transition temperatures of the individual phases.

L. Hädicke

6 Summary

The aim in this thesis was to give a basic overview over the morphology and phase composition in the as-deposited state and the phase stability and at elevated temperatures of the Zr-Al-Y-N and Zr-Al-Y-O-N.

The first step was the deposition of the film with an unbalanced DC magnetron PVD system. In order to obtain oxinitride films the working gas was artificial air.

The elemental composition was investigated with EDX and ERDA. ERDA was especially used to determine the accurate amount of O and N in the film. The advantages of ERDA and EDX which is more accurate with heavier elements were combined.

Phase evaluation was done by using XRD and SAED. The measurements revealed randomly oriented crystalline phases of c-Zr(Y)AlN and hex-ZrAlN for the nitrides. In the oxinitride film the c-Zr(Y)AlN was found, as well as γ-Al_2O_3 and t-ZrO_2. Y_2O_3 was found only over an Y content of 0.8 at%.

In SEM investigations the cross sections of our films reveals dense, but otherwise feature-less cross sections, typical for nanostructured films. Whereas the nitride films show a coating thickness of ~ 3.5 μm the oxinitrides only show about 2 μm in the same deposition time. This reduced thickness is due to poisoning of the target because of the used artificial air used for the oxinitrides.

The morphology, investigated by HRTEM, showed nanocrystalline structure with a grain size of ~7 to ~15 nm in the nitride films. In the oxinitride films a crystallite size of ~7 up to ~12 nm was found. The crystallites were surrounded by a boundary phase with a low short range order (amorphous).

The hardness value of 16.07 GPa was found for the Y free nitride coating. With increasing Y-content the hardness decreases rapidly till it reaches a plateau of 15.5 GPa at about 3.4 at% of Y where the hardness does not change with the Y-content. In comparison to the nitride coatings the hardness of the oxinitride coatings starts at a value ~8.3 GPa for the coatings below 3 at% Y, but at an Y content of 10.4 at% the hardness increases to 12.2 GPa.

In the nitride films the effect of solid solution results in an increase of the Young's modulus from 194.43 to 208 GPa at an Y-content of 1.26 at% Y. At a higher Y-content the Young's modulus decreases to a level of 203.67 GPa and reaches 201.34 GPa at an Y-content of 15.96 at% Y. This decrease in Young's modulus can be explained in the formation of the relatively soft c-YN phase. Y. Cherchab et al. [80] gave an average bulk modulus of 166 GPa which explains the decrease with increasing Y-content. For the oxinitride films an increase from a

L. Hädicke

level of about 150 GPa to a maximum of 169.9 GPa at an Y-content of 10.4 at% Y is observed.

Investigating the thermal stability with DSC, several reactions were observed for both systems up to 1450°C. Both systems show recovery and recrystallization reactions. The nitride films show the c-ZrAlN + h-ZrAlN → c-ZrN + h-AlN spinodal decomposition reaction at around ~1150°C, decreasing with Y-content. The additive γ-Al_2O_3 phase in the oxinitride films shows a transformation into α-Al_2O_3 at about ~1200°C. During the DSC measurements a mass spectroscopy was executed. These measurements showed that by trend more N_2 than O_2 was released. The mass loss detected during DSC measurements showed the highest mass loss during the spinodal composition for the nitride films and during the $\gamma \rightarrow \alpha$ transformation of Al_2O_3.

L. Hädicke

References

1. D.M. Hoffmann, B.Singh, and J.H. Thomas, eds., Handbook of Vaccum Technology. Academic Press, Boston,G.

2. M. Ohring, Materials science of thin films, (2002)

3. R.A. Häfer, Oberflächen- und Dünnschicht- Technologie, Teil I: Beschichtungen von Oberflächen, Springer-Verlag, Berlin, Heidelberg 1987

4. M.G. Hocking, V. Vasantasree, P.S. Sidky, Metallic and Ceramic Coatings, Longman Scientific & Technical, Essex, 1989

5. T. Burakowski, T. Wierzchen, Surface Engineering of Metals, CRC Press LLC, 1999

6. R.F. Bunshah, in R.F. Bunshah, S.M. Rossnagel, G.E. McGuire (ed.), Handbook of Hard

7. Coatings, Deposition Technologies, Properties and Applications, Noyes Publications, New Jersey, 2001

8. K.-P. Müller, Praktische Oberflächen- Technik, vorbehandeln, beschichten, prüfen, Vieweg, Braunschweig, 1999, 3.Auflage

9. G. Franz, Oberflächentechnologie mit Niederdruckplasmen, Beschichten und Strukturieren in der Mikrotechnik, Springer-Verlag, Berlin, Heidelberg, 1994 (2nd ed.)

10. F.F. Chen, Plasma Physics and Controlled Fusion, Plenum Press, New York, 1984

11. B. Rother, J. Vetter, Plasmabeschichtungsverfahren und Hartstoffschichten, Deutscher Verlag für Grundstoffindustrie, Leipzig, 1992

12. L.I. Maissel, in L.I. Maissel, Handbook of Thin Film Technology, McGraw-Hill, New York, 1983

13. B. Window, N. Savvides, J. Vac. Sci. Tech. A, 4 (3), 1986, 453 29. B. Window, Surface Coating Technology, 81, 1996, 92

14. D.M. Mattox, J. Vac. Sci. Tech. A, 3 (3), 1985, 553

15. T. Burakowski, T. Wierzchon: Surface Engineering of Metals: Principles, Equipment, Technologies; CRC Press, Boca Raton, 1999

16. A. Laarmann, T. Wenz: Modern Surface Technology, WILEY-VCH, Weinheim, 2006

17. H. Hofmann, J. Spindler: Verfahren der Oberflächentechnik, Fachbuchverlag Leipzig, 2004

L. Hädicke

18. A. Grill: Cold Plasma in Materials Fabrication, IEEE Press, New Jersey, 1994 für die Grundstoffindustrie, Leipzig, 1992

19. N.B. Chapman: Glow Discharge Processes, John Wiley, New York, 1984 12. R.F.

20. K.U. Riemann: in Hartstoffschichten zur Verschleissminderung, (eds. H. Fischmeister, H. Jehn), DGM, Oberursel, 1987

21. P.H. Mayrhofer: Materials Science Aspects of Nanocrystalluine PVD Hard Coatings, PhD-Thesis, University of Leoben, 2001

22. C.A. Neugebauer: in Handbook of Thin Film Technology, (ed. L.I. Maissel), McGraw-Hill, New York, 1983

23. P.B. Barna, M. Adamik: in Protective Coatings and Thin Films, Synthesis Characterization and Applications, (eds. Y. Pauleau, B.P. Barna), Kluwer, Dordrecht, 1997

24. P.B. Barna, M. Adamik, Thin Solid Films 317 (1998) 27-33

25. H.A. Jehn: in Advanced Techniques for Surface Engineering, (eds. W. Gissler, H.A. Jehn), Kluwer, Dordrecht, Brussels, 1992

26. P.H. Mayrhofer: Lecture Script Basics of Deposition and Material Science of Hard Coatings, 2007C. Suryanarayana, Intern. Mat Rev. 40 (2) (1995)

27. B.A. Movchan, A.V. Demchishin, Phys. Metals. Metallogr. 28 (4) (1969) 83-90 R.

28. Messier, A.P. Giri, R.A. Roy, J. Vac. Sci. Tech. A 2 (2) (1984) 500-503 J.A.

29. Thornton, J. Vac. Sci. Technol. 11 (4) (1974) 666-670

30. R. Kieffer, P. Ettmayer, F. Petter, Monatshefte für Chemie 102 (1971)

31. P.B. Barna, M. Adamik, Thin Silid Films, 317 (1998)

32. E. Hornbogen, H. Warlimont, Metallkunde, Springer – Verlag, 1991.

33. G. Gottstein, Physikalische Grundlagen der Materialkunde, 2. Auflage, Springer Verlag, Berlin, 2001.

34. L. Hultman, Vacuum 57 (2000) 1.

35. W. Schatt, H. Worch, Werkstoffwissenschaft, Deutscher Verlag für Grundstoffindustrie, 1996.

36. H. J. Bargel, G. Schulze, Werkstoffkunde, 8. Auflage, Springer – Verlag, Berlin, 2004.

37. E. Hornbogen, Werkstoffe, 7. Auflage, Springer – Verlag, Berlin, 2002.

38. RF Zhang, SH Sheng, S Veprek. Appl Phys Lett 2007;90:191903

39. J-E Sundgren, H-TG Hentzell, J Vac Sci Technol A 1986;4:2259

40. S PalDey, S-C Deevi, Sci Eng A 2003;342:58

L. Hädicke

41. H J Holleck. Vac Sci Technol A 1986;4:2661

42. G Berg, C Friedrich, E Broszeit, C Berger In: Riedel R, editor. Handbook of ceramic hard materials. Weinheim Wiley-VCH;2000 p965

43. DJ Li, Sci Chin Ser E: Technol A 1986;4;2661

44. R.Lamni, R Sanjinés, M Parlinsk-Wojtan, A Karimi, F Lévy. J Vac sci Technol A 2005;23(4):593

45. S.Veprek, SH Sheng, RF Zhang. Acta Materialia 56 (2008);968-976

46. R L Jones, Metallurgical and Ceramic Protective Coatings, edited by K. Stern,1996, ISBN 0 421 54440 7

47. Y. A. Tamarin, E.B. Kachanov, and S.V. Zherzdev, Materials Science Forum, Vol. 251-254. (1997), pp 949

48. M. Peters, C. Leyens, U. Schulz, W.A. Kaysser, Advanced Engeneering Materials, 3(No.4), (2001), pp. 193

49. Y. Du, Z. Jin, and P.Huang, J. Amer. Soc., 74(7),(1991),pp. 1569

50. M. Yashima, M. Kakihana, M. Yoshimura, Solid state ionics, 86-88(2), (1996) pp. 1131

51. Boryana Rashkova, Phd Thesis " Microstructural Characterization of Yttria Stabilized Zirconia Thermal Barrier Coatings Grown on Sapphire Subtrate", Max – Planck-Institut für Metallforschung Stuttgart, 2003, Nr145

52. User Manual A400 VL, Leybold AG.

53. Operational Manual ACG-6B, ENI Company Ltd.

54. User Guide Leybold Vacuum, Leybold AG.

55. User Guide Tylan General R 7030/7031, Tylan General Gmb

56. User Manual Duo 20, Pfeiffer Vacuum GmbH, 2002

57. Eberhart, Structural and Chemical Analysis of Materials, Wiley VCH, Weinheim, Germany, 1991., 7878. D.C. Joy, in Electron Microscopy - Principles and Fundamentals, (ed. S. Amelinckx, D. van Dyck, J. van Landuyt, G. van Tendeloo), Wiley VCH, Weinheim, Germany, 1997.].

58. J.M. Howe, Transmission Electron Microscopy and Diffractometry of Materials, Springer Verlag, Berlin, Heidelberg, 2001.

59. M. Lechthaler, Diploma Thesis, Department of Physical Metallurgy and Materials Testing, Leoben, 2005.

L. Hädicke

60. D.C. Joy, in Electron Microscopy - Principles and Fundamentals, (ed. S. Amelinckx, D. van Dyck, J. van Landuyt, G. van Tendeloo), Wiley VCH, Weinheim, Germany, 1997.

61. K.E. Sickafus, in Encyclopedia of Materials Characterization, (ed. C.R. Brundle, C.A. Evans Jr., S. Wilson), Butterworth-Heinemann, Stoneham, Massachusetts, 1992.

62. H.P. Klug, L.E. Alexander, X-Ray Diffraction Procedures, John Wiley, New York, 1974

63. William Henry Bragg, William Lawrence Bragg, Proceedings of the Royal Society of London. Series A, Containing Papers of a Mathematical and Physical Character 88/605 (1913) 428.

64. L. Snyder, in X-ray Characterization of Materials, (ed. E. Lifshin), Wiley VCH, Weinheim, Germany, 1999.

65. W.F. Hemminger, H.K. Cammenga, Methoden der Thermischen Analyse, Springer-Verlag, Berlin, Heidelberg, 1989

66. P. Eklund: Multifunctional nanostructured Ti-Si-C thin films, PhD-Thesis, University of Linköping, 2007

67. W. C. Oliver and G. M. Pharr An improved technique for determining hardness and elastic modulus using load and displacement sensing indentation experiments Journal of Materials Research 7 1564 (1992)

68. J.L.Labar, Ultramicroscopy, 103(2005) 237-249

69. W.E.Lee, K.P.D. Lagerlof, Structural and Electron Diffraction Data for sapphire (α-Al_2O_3), Journal of electron Microscopy Technique 2:247-258, 1988

70. Wang, D.-N., Guo, Y.-Q., Liang, K.-M., Tao, K., Sci. China, Ser. A: Math., Phys., Astron., volume 42, page 80 (1999)

71. Verwey, E.J.W., Z. Kristallogr., Kristallgeom., Kristallphys., Kristallchem., volume 91, page 317 (1935)

72. Kimmel, G., Zabicky, J., Goncharov, E., Ben-Gurion Univ. of the Negev, BeerSheva, Israel., ICDD Grant-in-Aid (2002)

73. O. Fabrichnaya , F. Aldinger;Assessment of the thermodynamic parameters in the system ZrO_2-Y_2O_3-Al_2O_3, Z. Metallk 95(2004)

74. Natl. Bur. Stand. (U.S.) Monogr. 25, volume 21, page 136(1985)

75. M. Konuma, Film Deposition by Plasma Techniques, Springer-Verlag, Berlin, Heidelberg, 1992

L. Hädicke

76. K.N. Tu, J.W. Mayer, L.C. Feldman, Electronic Thin film Science for Electrical Engineers and Materials Scientists, Macmillan 1992.

77. H.Willmann, PhD Thesis Department of Physical Metallurgy and Materials Testing, Leoben, 2006.

78. Netzsch, User Manual Netzsch STA 409 C, 2000

79. F.Adibi, I.Petrov, L.Hultman, U.Wahlström, T.Shimizu,D.CIntyre, J.E.Greene and J.-e. Sundgren, J.Appl. Phys.Vol. 69, No. 9, (1991)

80. Y.Cherchab, B. Amrani, N. Sekkal, M. Ghezali, K. Talbie, Physica E 40, 606-617 (2008)

81. Martin, K., McCarthy, G., North Dakota State University, Fargo, North Dakota USA., ICDD Grant-in-Aid (1989)

82. G. Kienel, K. Röll (ed.), Vakuumbeschichtung 2 , Verfahren und Anlagen, VDI-erlag, Düsseldorf, 1995

83. R.F. Bunshah, D.M. Mattox, in Deposition Technologies for Films and Coatings, Developments and Applications, Noyes Publications, New Jersey, 1982

84. S. PalDey, S.C. Deevi, Mat Sci. Eng., A 342, 2003, 58

85. R. Mévrel , Materials Science and Engineering and Theory, J.Mater. Res. Vol. 5, No. 1 (1990), pp151

86. W.Y. Lee, D.P. Stinton, Ch. C. Berndt, F.ERdogan, Y.D. Lee and Z. Mutasim, J. Am. Ceramic Soc., 79 [12] (1996)

87. G. Kimme, J. Goncharov, E. Ben-Gurion Univ. of the Negev, Beer Sheva, Israel., ICDD Grant-in Aid (2002)

L. Hädicke